The Application Feasibility for Regional and Commercial Use of CO_2 for Enhanced Coal Bed Methane Recovery

Final Report: November 2021

Report Prepared for
PacifiCorp

Report Prepared by

Department of Chemical Engineering
University of Utah

John McLennan
USTAR Professor
Department of Chemical Engineering
University of Utah
jmclennan@egi.utah.edu
801-587-7925

Carlos Vega-Ortiz
carlos.vega@utah.edu

Oluwafemi Omotilewa
Femi.omotilewa@utah.edu

Department of Chemical Engineering
University of Utah

Department of
CHEMICAL ENGINEERING
THE UNIVERSITY OF UTAH

Executive Summary

This project has been a feasibility study to evaluate opportunities for using CO_2 for enhanced natural gas recovery from coal seams, specifically coal seams in Emery County in Utah. An assessment has also been made of the capability of these coal seams to concurrently sequester CO_2. Much in the same way that CO_2 is currently used for economically beneficial enhanced oil recovery, CO_2 also has the potential for enhancing natural gas recovery from coal beds ("coal bed methane").

Long-term sequestration is a desirable complement to above-ground technologies for improving plant efficiency and high grading carbon dioxide streams. CO_2 has a preferential adsorptive affinity in comparison to methane. The methane is naturally present in coal below ground. If carbon dioxide were injected into unmineable coal seams in Utah, it would preferentially displace (and allow the production of) methane and replace the methane within the coal. Methane is produced from - and carbon dioxide is sequestered in - deep, unmineable coals.

Laboratory testing and numerical simulations were used to characterize CO_2 injection in Emery/Ferron coal seams adjacent to the Hunter and Huntington plants in central Utah. Simulations demonstrated that it may be feasible to inject 1.16 million tons and sequester 1.15 million tons of CO_2 over 20 years from two injection wells alone. Injection capacity would scale upwards with additional wells. Additionally, 13.95 billion cubic feet of methane could be recovered within the same period from two nearby production wells. The methane estimates are optimistic because there has been historic gas production and some depletion would have already occurred. Regardless, produced methane can go directly to sales or, more rationally, can be used for compression to inject carbon dioxide or flue gas into the coal.

Some of the key findings are as follows.

1. **Methane capture and purification before injection.** Laboratory scale, experimental work using a surrogate to flue gas (a nitrogen-carbon dioxide mixture) suggested that there could be some advantages in injecting flue gas directly without separation of the carbon dioxide explicitly. The advantage is not necessarily that NOx can be sequestered but that the presence of nitrogen may enable moving CO_2 deeper into the coal (hypothesis at this point, based on laboratory observations, requiring validation).
2. **Coal swelling** impacts coal-bed methane production. The experience in the past has been that chemisorption and associated swelling have reduced cleat permeability in coals. Tactical changes in the injection strategy – multiple horizontal wells, with water diversion stages and pressures above fracturing are envisioned to effectively provide conformal injection and storage of CO_2 through the bulk of the reservoir. The experimental work in this study demonstrates the consequences of adsorption and points to some advantages in injecting flue gas rather than explicitly separated

carbon dioxide. A carefully monitored and designed pilot injection program could safely help to clarify this at a scale larger than in the laboratory.

3. The true **capacity** for carbon dioxide storage in coals in-situ has not been established. Continuous injection below fracturing pressure may not be a realistic scenario. The potential for refined injection procedures including fracturing, water stages, and in particular horizontal wells, might alleviate the mismatch between a necessarily large and constant CO_2 supply and the sequestration volume in the coals. A pilot project could provide clarification. The geologic specifics of the Ferron coal/sandstone packages could be favorable for injection where the movement of carbon dioxide (or flue gas) through the sands would be relatively unimpeded and storage in the coal could move well away from the injectors. The potential complication is the potentially finite extent of the sands.
4. **Seal integrity and permanence of sequestration** are always a concern for subsurface storage. Effective monitoring is required. Injection of water, particularly calcified water after periodic injection of carbon dioxide could afford mineralization and more permanent sequestration. Predicting, monitoring, and mitigating leakage is a common theme of all subsurface storage operations. The overlying Mancos formation is thick and would provide an effective seal.
5. **Logistics and feasibility of piping CO_2** to injection equipment from a plant environment to the injection facility. The two plants are close to a historically produced coal bed methane play. In particular, the Buzzard Bench field was evaluated in this work.
6. **The estimated OGIP (original gas in place - methane)** in the northern block of the Buzzard Bench field abutting the Hunter and Huntington power plants is 153 to 202 bcf methane (using typical gas contents of 190 and 350 scf/ton, respectively for worst- and best-case scenarios). The estimated OGIP for the southern block ranges from 192 to 450 bcf methane. Some of this gas has been already produced because of coalbed production operations over the past twenty years or so.
7. **The estimated CO_2 maximum storage capacity:** The dry-ash free CO_2 gas capacity of a Ferron coal sample at in-situ conditions was measured as 670 scf/ton, which leads to a volumetric capacity of carbon dioxide of 523 and 673 bcf of CO_2, for the northern and southern Buzzard Bench blocks, respectively.
8. **This is not an insignificant operation.** Consider servicing the Huntington plant. As a benchmark, consider an annual CO_2 emission of 6,000,000 tons of CO_2. Over twenty years, simulations suggest that about 75 to 100 injectors would be required – a significant investment with significant OPEX requirements. Only a pilot program can characterize this for sure. These numbers are conservative because the Langmuir isotherm for the CO_2 was not available from Schlumberger when the simulations were completed. After those data were generated, the storage capacity appears to be substantially higher, and the number of injectors could be halved – still a significant operation.
9. A limitation on the rate of injection per well is the reduction in permeability associated with swelling. As the permeability reduces, the injection pressure

increases. The limit on the injection pressure has been taken to be minimizing the bottomhole pressure to avoid hydraulic fracturing. Only a pilot/field experimentation will ultimately confirm these pressure limitations. There is also some laboratory evidence that direct injection of flue gas may mitigate the consequences of the swelling.

10. **Question: Will an increase in injection pressure due to swelling be as severe as simulated if the interfingering sands act as a pressure relief and delivery mechanism?** Almost certainly not. The Ferron sands are interfingered with the coals. Measurements of the permeability of the Ferron sand suggest preferential gas flow would occur into the sands, offering the ability to bypass *locally* reduced permeability in the coals. With time, flow into and adsorption would occur in the interfingered coals with accompanying sequestration. Simulations tend to suggest this as well. A pilot test would establish the value of this revolutionary concept – relying on the sands to deliver the CO_2 and the coals to sequester it.
11. **Question: What happens if the pressure causes local fracturing?** This is an unanswered technical question. If the fracturing is restricted to the sands and the coals, the results will be beneficial. Areas of locally reduced permeability in the coals would be breached/bypassed and injectate could move beyond the impaired zones. The concern is breaching a seal. However, the overlying Mancos formation is relatively thick and could tolerate some local fracture penetration. Consequently, the method for fracturing, as part of the storage protocol, needs to be carefully defined and tested at a pilot scale. For example, if high pressures are encountered during injection, a small slug of water might be injected to allow a small fracture to occur, to see if pressure can be relieved. This is "unexplored technical territory" and would require testing and validation. Assuming that the carbon dioxide can be maintained in a super critical state, a nominally incompressible slug (the water) may not be needed to generate a small fracture step. This is advocating the possibility of a WAG (water alternating gas) operation. Corrosion would need to be considered.
12. **Question: Can flue gas be pumped?** There are some indications that it could be viable to pump flue gas or at least a nitrogen-carbon dioxide mix. Oxygen and non-scavenged H_2S are undesirable from a corrosion perspective, but possibly reduced separation of the flue gas is feasible. Laboratory testing has shown that the degree of swelling is contingent on the amount of nitrogen present with the carbon dioxide and that permeability reduction is similarly impacted. If flue gas is injected, permeability reduction may be reduced. The drawbacks are that the relative concentration of carbon dioxide injected is less and the hydrostatic pressure will be reduced (with miscibility or perfect mixing) and expenditure for compression and pumping will consequently be higher.

The report summarizes numerical calculations assessing volumetrics of the Buzzard Bench field – first-order estimates of how much carbon dioxide could be stored. Experimental measurements on Ferron coal samples also highlighted sorptive capacity.

Preliminary considerations are provided for considering a pilot program of flue gas injection.

One question often posed is whether the carbon dioxide would remain sequestered if there is a drilling penetration at some time in the future. Consider a case in the Ferron sandstone at a depth of 3500 ft. The hydrostatic pressure would be about 1500 psi (0.433 psi/ft and a nominal depth of 3500 ft TVD). A well penetrating this formation, pressurized with water as the wellbore fluid would be in equilibrium with the carbon dioxide in situ and there would not be desorption from the coal or gas produced by expansion drive from the sand. Gas production would occur if the pressure in the penetrating well is decreased and would continue until that well was killed (pressure brought back to hydrostatic). If in time, the carbon dioxide is entombed by mineralization, drawdown or depletion would not immediately produce adsorbed gas.

Table of Contents

I. Introduction

This project has been a high-level feasibility study to evaluate opportunities for using CO_2 for beneficial use in the form of enhanced natural gas recovery from coal seams, specifically coal seams in Emery County in Utah. As part of this study, an assessment has been made of the capability of these local coal seams to concurrently sequester the CO_2. Much in the same way that CO_2 is currently used for economically beneficial enhanced oil recovery, CO_2 also has the potential for enhancing natural gas recovery from coal beds ("coal bed methane"). In the past, significant research has been focused across the United States to identify cost-effective CO_2 capture technologies. In some cases, large utility-scale projects have been constructed (i.e., SaskPower's Boundary Dam project and Petra Nova's W.A. Parrish project). For those projects, the underlying disposition of the CO_2 is for enhanced oil recovery (EOR).

Beyond EOR, long-term sequestration is a desirable complement to above-ground technologies for improving plant efficiency. CO_2 has a preferential adsorptive affinity to coal in comparison to methane. Methane is naturally present in coal below ground. If carbon dioxide were injected into unmineable coal seams in Utah, it would preferentially displace (and allow production) methane and replace the methane within the coal. Methane is produced from - and carbon dioxide is sequestered in - deep, unmineable coals.

For this study, the focus has been on the potential for recovering coal bed methane which is abundant in the areas surrounding the Hunter and Huntington power plants, while sequestering carbon dioxide. This study considered options for CO_2 use for enhanced recovery of coal bed methane and the ability of these regional coal seams to be used as geologic sequestration resources. The study objectives were to:

1. Determine whether local coal beds are conducive to enhanced CO_2 methane recovery.
2. Provide a high-level technical, economic, and environmental synopsis on the costs and benefits of sequestration in the Ferron coals in central Utah.
3. Propose new technologies for improving CO_2 injection efficiency.

Laboratory testing and numerical simulations were carried out to characterize CO_2 injection in Emery/Ferron coal seams adjacent to the Hunter and Huntington plants. Simulations demonstrated that it may be feasible to inject 1.16 million tons and sequester 1.15 million tons of CO_2 over 20 years from two injection wells. Injection capacity would scale upwards with additional wells. Additionally, 13.95 billion cubic feet of methane could theoretically be recovered within the same period. The methane estimates are optimistic because there has been historic gas production and some depletion would have already occurred. Regardless, produced methane can go directly to sales or, more rationally, can be used for compression to inject carbon dioxide or flue gas into the coal.

Laboratory testing demonstrated three important attributes.

1. Exposure of the Emery coal to carbon dioxide at reservoir conditions (temperature and pressure) is accompanied by adsorption of the CO_2. With adsorption, coal swelling occurs and permeability to carbon dioxide is reduced.
2. This swelling has usually been the primary negative consequence of injection into coal. However, experimental work herein has demonstrated that injection of synthetic flue gas – without separating the CO_2 – does not significantly degrade the permeability and a greater volume of fluid can be injected from a single well. The advantage is that separation of carbon dioxide is not required. The disadvantages are that the concentration of injected carbon dioxide is lower and injection costs will be higher because of the reduced specific gravity of the flue gas mixture (the hydrostatic pressure of the gas mixture will be less than CO_2 itself, meaning the static bottomhole pressure will be lower and additional pumping power will be required).
3. Depending on local conditions, the interbedded sandstone has enough porosity and permeability to deliver flue gas deep into the reservoir for ultimate sequestration.

Simulations of one coal bed methane field adjacent to the power plants showed viability but indicated numerous injectors would be needed to completely offset emissions. Furthermore, the simulation results confirm that the CO_2 adsorption during neat carbon dioxide injection cause coal matrix swelling leading to cleat closure hence, reduction in the coal permeability. Consequently, the volume of CO_2 injected, and methane recovered decreased by 29% and 19% respectively when swelling was used in simulations. The simulations did not consider direct flue gas injection which could ameliorate some of the local swelling issues.

Despite the concern for swelling, the Emery/Ferron coal sequence is a geologically favorable regime. A thick Mancos formation overburden acts as a seal to prevent upwards migration. Coals are present with adsorptive capacity. Finally, and very important, higher permeability Ferron sandstone interfingers with the coal seams and may provide an inert (nonswelling) pathway for the deliverability of gas deep into the formation for sequestration in the coals, progressively bypassing locally swelled areas. Considering these elements, the simulations, based on the experimental measurements, demonstrated injection feasibility, even in the presence of potential permeability reduction by coal matrix swelling during CO_2 injection. Injection and production strategies become viable to maximize injectivity and sequestration to overcome problems resulting from permeability changes and override.[1]

[1] In some less favorable geologic settings, after permeability reduction, carbon dioxide has been found to be directed to overlying formations, overriding the coal.

II. TASKS

The specific tasks carried out to assess the feasibility of CO_2 sequestration and concurrent production of residual methane in coal beds proximal to the Hunter and Huntington Power Plants are shown in Table 1.

Table 1. Tasks

Task	Description
1	**Resource Evaluation:** From public domain sources (UGS[2] data in particular) summarize the possible injection locations, capacities, advantages, and challenges
2	**Bench Scale Demonstrations:** Using CO_2 as well as surrogate flue gas (a synthetic blend of 80% N_2 and 20% CO2 was used) carry out bench-scale demonstration measurements to assess sorptive capacities and permeability modification in representative Utah coals.
3	**Permanent Sequestration:** How can CO_2 be more permanently be sequestered in coal seams?
4	**Economic Viability:** First order estimate of the economics of sequestration offset partially by methane production.
5	**Simulations:** Based on Tasks 1 through 3 to confirm storage capacity
6	**Pilot Program:** Five-spot injection and monitoring program suggested

III. Background:

III.1 Adsorption

Coalbed methane has been a viable natural gas production source since the 1980s. Unlike conventional natural gas, which is stored by compressibility in pore space, methane in coal is physically adsorbed to the surfaces within the coal. Following production of the water that is in the cleats in the coal (naturally present fractures), reduction in pressure will encourage the methane to desorb from the solid coal matrix and be produced. Hydraulic fracturing is often required to provide conductive pathways for this desorbed gas to move to the wellbore. The capacity of generic coal to store methane by adsorption is shown by the isotherm in Figure 1. That figure further demonstrates that as the in-situ reservoir pressure is reduced, methane will be desorbed. That is, Figure 1 shows a reduced adsorptive capacity for methane as the pressure in a reservoir is reduced. This means that as the reservoir pressure depletes during production, methane will be produced.

The bulk of the in-situ gas production requires significant drawdown (and ultimately depletion[3]). The shaded area in Figure 1 schematically denotes the pressure in the

---

[2] Utah Geological Survey

[3] Drawdown is the reduction in the pressure in a wellbore that provides a gradient (with respect to the average reservoir pressure) for flow to occur. Depletion is the reduction in pressure throughout the reservoir caused by drawdown.

wellbore below which artificial lift (pumping or similar) would need to be implemented to recover the substantial volumes of remaining gas – with attendant costs. Figure 2 shows an example of declining production in a prominent Utah coalbed methane play. Other examples throughout the state and the country are similar. One initial question to keep in mind is *"How can this residual gas be recovered more economically?"*

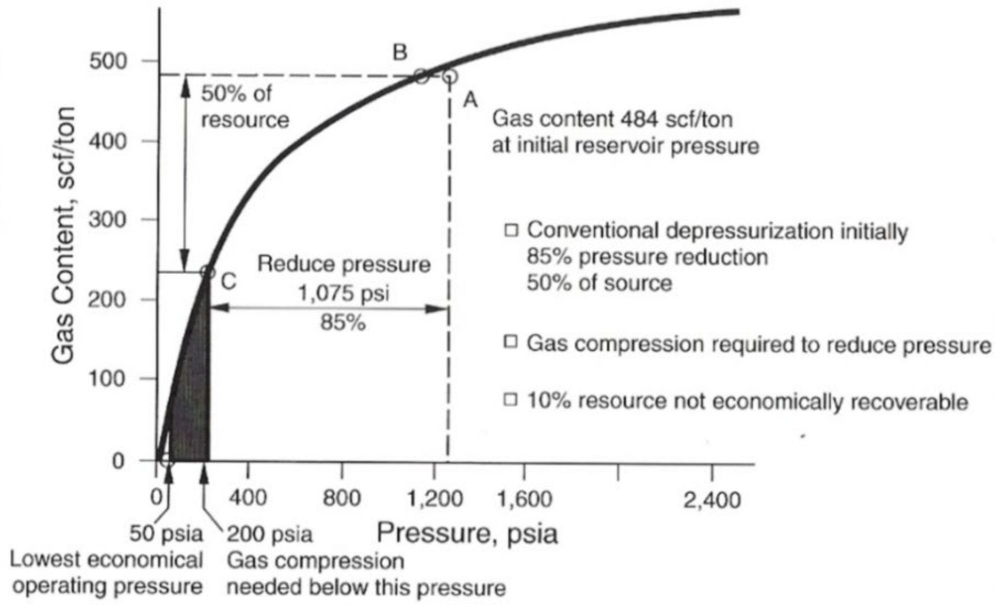

Figure 1. This is an example of an isotherm[4] for methane stored by adsorption in typical coal. As can be seen, by the name "isotherm", the temperature is constant. The adsorptive potential reduces as temperature increases. At constant temperature 1) the amount of methane adsorbed increases as the pressure (representing the reservoir pressure) increases, and 2) reciprocally, as the pressure decreases methane will be produced because the reservoir's adsorptive capacity is reduced. Notice that a significant quantity of methane remains (and will not be produced) by reducing pressure alone. (Courtesy of Halliburton)

Insight into possible methods for producing residual methane and sequestering carbon dioxide can be gained by comparing the adsorptive capacity of different gases. Figure 3 demonstrates that carbon dioxide has a greater affinity (more gas will be adsorbed at a particular temperature and pressure) than methane. Carbon dioxide will displace methane from coal. This means that if carbon dioxide is injected into a methane-saturated coalbed, the carbon dioxide will be adsorbed, and methane desorbed/produced.

[4] An isotherm is a measurement of the amount of stored gas as a function of pressure of the gas – determined at a constant temperature.

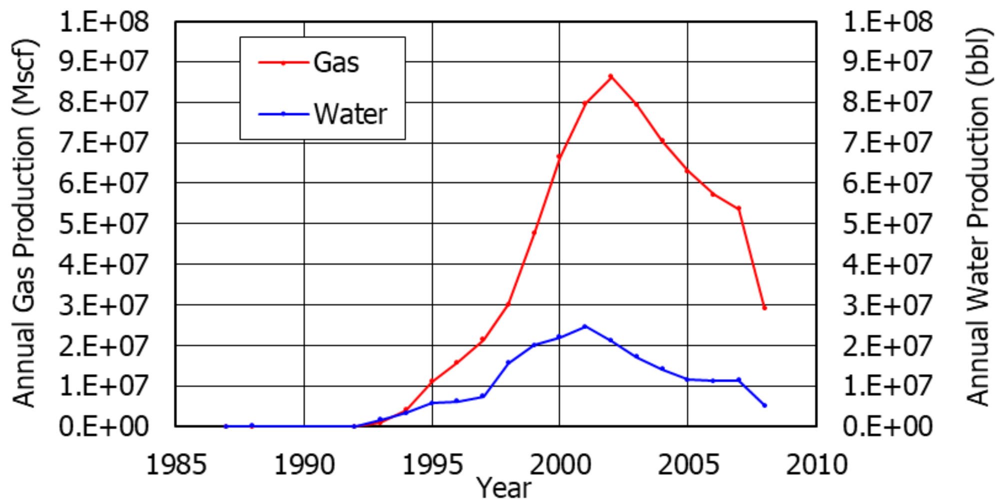

Figure 2. Quarterly production data from the Drunkard's Wash field in Carbon County Utah. There are various reasons for the decline some of them related to depletion, some related to gas pricing. Regardless, there is methane remaining in-situ. This field is still operational.

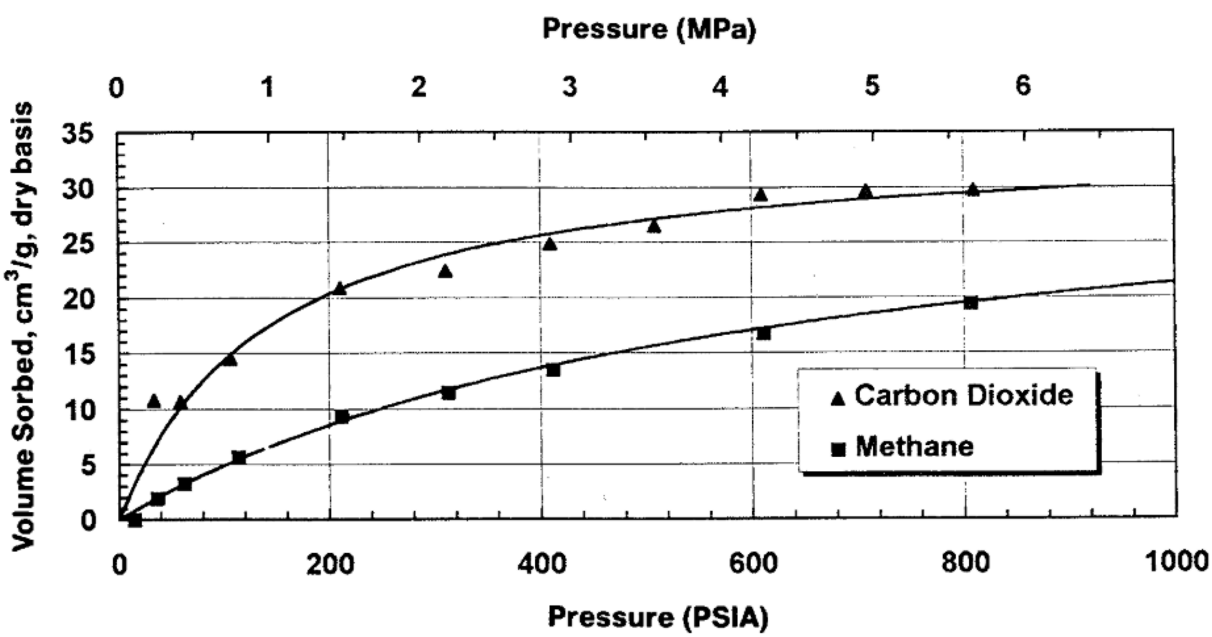

Figure 3. Isotherms for nominally equivalent coal samples where the sorbates varied from methane to carbon dioxide (Levine, 1996). A blend falls between the two extremes. Two features stand out. The first is that substantially more carbon dioxide is adsorbed in this coal than methane. The second aspect is that there is a tremendous affinity for carbon dioxide at low pressures.

Coalbeds have both cleat[5] and matrix porosity. Almost all the gas-in-place (or sequestered) is stored in the matrix by adsorption, while the cleats serve as conduits for gas migration. The permeability of the primary porosity unit (the matrix) is negligible since these pores are small. Migration of gas from the coal matrix (primary porosity) occurs by desorption, diffusion, and pressure-driven flow; after a decrease in gas concentration by first pumping out the connate water (dewatering), leading to the development of a concentration gradient. The gas then desorbs from the coal matrix and diffuses into the cleats. Fluid flow through the cleats (secondary porosity system) towards the wellbore is subsequently achieved by Darcy flow. In most coal beds, primary methane recovery begins when dewatering is complete (or nearly so). In some cases, this primary recovery may be up to 60 percent of the gas in place (Stevens et al., 1998). Enhanced Coalbed Methane (ECBM) recovery, facilitated by injecting other gases, has been advocated as an effective means of recovering the residual gas (Shi and Durucan, 2003; Puri and Yee, 1990).

Research during the past three decades confirms the higher adsorptive capacity of CO_2 in comparison to methane (Arri and Yee, 1992; Harpalani et al., 2008). Coal seams can adsorb huge volumes of gas, especially CO_2, due to their large internal surface area (30 to 300 m^2/g; Berkowitz, 1985). Coalbeds not only provide the potential to adsorb CO_2, but the injected CO_2 can concurrently promote the desorption of additional methane not recoverable during primary recovery. One estimate is that coal can store six times more gas in comparison to the volume of rock in a conventional gas reservoir (Utah Geological Survey, 1996). Moreover, since the affinity to adsorb CO_2 is almost twice that of methane (He et al., 2013), injected CO_2 would be preferentially adsorbed, and methane produced under the right conditions. The CO_2 is stored in-situ and not produced until the injected CO_2 front reaches the production well(s). This form of CO_2-ECBM operation has been proposed to sequester anthropogenic CO_2 emissions (Mathews et al., 2001; Schroeder et al., 2002; Steinberg, 2001).

An early CO_2-ECBM field project (Allison unit) was in the San Juan Basin (this basin was responsible for most CBM production worldwide in 1998; Reeves et al., 2003). The technical feasibility of sequestrating CO_2 in unmineable coal seams has been demonstrated by this and a few other field tests while enhancing methane production (White et al., 2005). These field tests include the Tiffany pilot in Colorado (Liang et al., 2003), the Allison unit in New Mexico, as previously described (Reeves et al., 2003), and the Medicine River pilot in Alberta (Mavor et al., 2004). Coal seam sequestration research has only been carried out in a few basins around the world, including the San Juan Basin in New Mexico and Colorado, the Ishikari coalfield CO_2 storage pilot project in Japan, the Black Warrior Basin in Alabama, and the Appalachian Basin, Eastern United States (Reeves et al., 2003; Robertson, 2010; Caroll et al., 2009; Reeves and Tailefert,

[5] Naturally occurring, often closely spaced fractures in coal; surrounding a microporous matrix of “solid” coal.

2002; Shi et al., 2008; Vangkilde et al., 2009; Wong et al., 2007; Ye et al., 2007). Although successes have been recorded, additional basin-specific research is necessary.

Recognizing the potential for carbon dioxide replacing methane in situ, pilot testing was undertaken several decades ago. For example:

- Burlington Resources (ConocoPhillips) carried out long-term CO_2 and N_2 injection into the Allison and Tiffany Units, respectively, both in the San Juan Basin. Figure 4 shows data from the Allison pilot (Reeves et al., 2002).
- Data from the nitrogen pilot in the Tiffany unit are shown in Figure 5. Nitrogen "functions" somewhat differently than carbon dioxide. The process is methane stripping (the partial pressure of methane is reduced since nitrogen is present in the cleats, causing desorption to achieve partial pressure equilibration). Since nitrogen is not adsorbed, there is likely to be a more rapid breakthrough of the injected gas from an injection well into a production well. This is undesirable because the pathway developed is a short circuit and less of the reservoir is exposed to the injectate (recovery of the methane is reduced).
- Alberta Innovates– Fenn-Big Valley, Alberta (Gunter et al., 2005); and China (Gunter et al, 2005).
- Southwest Partnership Fruitland Coal injection project:

> "The site is located in San Juan County, northern New Mexico, just within the limits of the high-permeability fairway of prolific coalbed methane production. The study area for the SWP project consists of 31 coalbed methane production wells located in a nine-section area. CO_2 was injected continuously for a year and different monitoring, verification, and accounting (MVA) techniques were implemented to track the CO_2 movement inside and outside the reservoir. A total of 319 MMscf[6] of CO_2 (or 18,400 tons) were injected over a 12-month period (July 30th, 2008, to August 12th, 2009); primarily due to highly permeable coal. However, as expected, the CO_2 injectivity dramatically decreased over the injection period. This was mainly due to matrix swelling and permeability reduction, as a result of the CO_2 being adsorbed onto the coal, while displacing methane, as well as increasing reservoir pressure. It was also determined that injection was predominately into the basal coal, reducing injectivity by 20%.
>
> Advanced Resources Inc., 2010

[6] MMscf indicates million standard cubic feet.

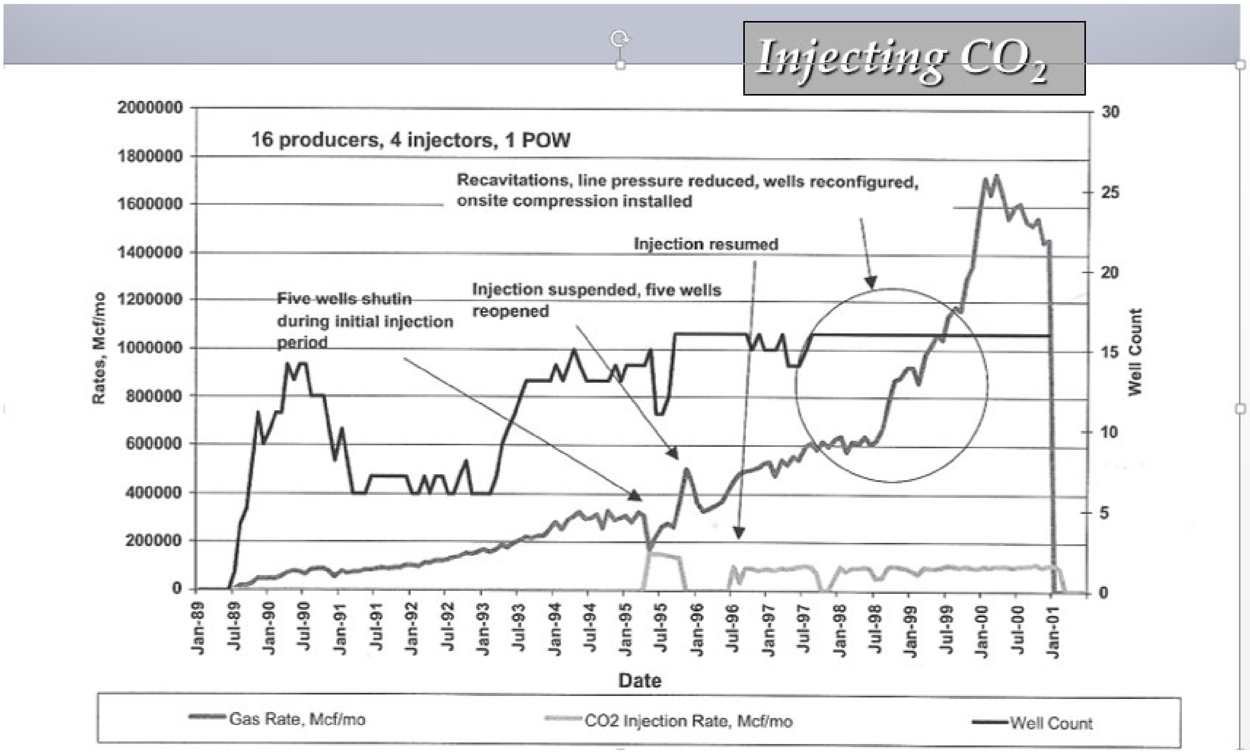

Figure 4. Over 5 years, 4.7 Bcf of CO_2 were injected and there was an incremental recovery of 1.5 Bcf of natural gas. These data are from the Allison Unit and the CO_2:CH_4 ratio was 3.1:1.0.

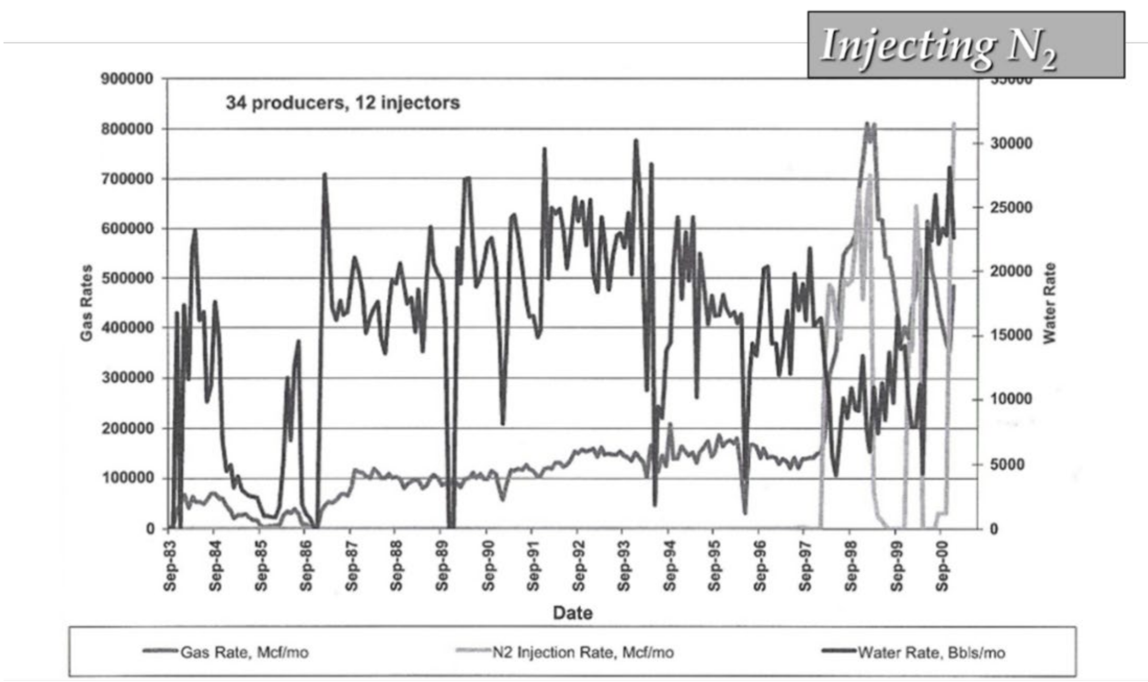

Figure 5. Nitrogen was injected into the Tiffany Unit. N_2 over 4 years. There was a fivefold increase in methane production, but early breakthrough occurred in 11 of 12 wells.

III.2 Recap - CO_2 Sequestration in Coal?

CO_2 capture and sequestration in favorable geologic settings have gained traction to fight global warming (Krupnick et al., 2014; Rai et al., 2010; Quere et al., 2018). Unmineable coal seams - regarded as too deep or too thin and lacking continuity to be mined economically - are feasible options for CO_2 sequestration and ECBM production. Coal can store a substantial amount of CO_2 at low pressure via adsorption. Low-pressure storage is desirable because it reduces the cost of compression during injection (Pan et al., 2017). As described above, various field and laboratory experiments have validated that CO_2-ECBM is feasible (Koperna et al., 2009; Mavor et al., 2004; Pagnier, 2005; Reeves, 2001).

Recall that complex evolution in the permeability of coal has been recognized with exposure to carbon dioxide. CO_2 adsorption causes an expansion of the matrix and penalizes cleat permeability by reducing cleat aperture. There can be increases in cleat permeability if the effective stress is reduced during injection – and conversely if the effective stress increases due to depletion. Permeability variations during ECBM operations have been defined from history matching with reservoir modeling (Pekot and Reeves, 2003; Shi and Durucan, 2005). Laboratory analysis has provided a better understanding of ECBM procedures, although field operations are complex (Van Bergen et al., 2006; Reeves et al., 2003).

The world's CO_2 storage capacity in unmineable coal seams has been estimated to be 350 gigatons (Stevens, 2002). The U.S. storage capacity has been estimated to be 90 gigatons (Reeves et al., 2003). Based on completely utilizing these storage opportunities, estimates of current output and storage capacity, the coal seams in the U.S. could provide 47 years of storage capacity for conventional coal-powered plant CO_2 emissions – even if a percentage of this were exploited, this signifies that coal has significant potential as a storage medium for CO_2 (Reeves et al., 2003).

Locally, the Uinta Basin in Utah has been attributed a storage capacity of 1.9 gigatons of CO_2 (2 percent of the U.S. storage capacity, per Godec et al, 2014). A field within the Uinta basin is the subject of the following evaluations.

IV. Challenges:

It seems that there is an elegant way – by injecting CO_2 – to displace residual methane and sequester the CO_2. This is true but there are some hurdles. The major hurdles are:

1. **Volumetrics:** The available subsurface volume will need to be assessed. A Utah field has been identified and the volumetrics assessed (refer to Section VI. Ferron CBM Volumetric Estimation). One field producing from Ferron/Emery coals, adjacent to the Hunter and Huntington plants has been reconstructed and potential storage volume estimated.

2. **Swelling:** CO_2 adsorption causes the coal matrix to swell. Matrix swelling is accommodated by the reduction in the cleat dimensions. The cleats provide permeability. The matrix swelling, therefore, reduces the cleat permeability. Override may follow – the CO_2 going elsewhere in a vertical setting since it becomes difficult to stay in the coal. There are numerous possible mitigations to this, and it is certainly not an insurmountable problem. Swelling is investigated for the candidate Utah coal. Two important observations from this research work are:
    a. **Permeability reduction is mitigated if flue gas is injected.** This has only been demonstrated in a laboratory setting. In flow tests through Ferron (Emery) coal a mixture of carbon dioxide and nitrogen – simulating flue gas – separated quickly in the pumping equipment (gravitationally) and the required pumping pressure and volumetric expansion of the sample varied in accordance with whether carbon dioxide or nitrogen was flowing. Overall, the permeability reduction was less when pumping this mixture. This is not surprising because of the reduced CO_2 concentration. It opens the door for improved injectivity by not separating the carbon dioxide before injection.
    b. **Interfingered or adjacent high permeability sands** allow carbon dioxide to be injected deep into the formation, bypassing local swelling bottlenecks.
3. **Sequestration:** The CO_2 used in tertiary injection recovery programs like this is not permanently sequestered. If there is a wellbore penetration or a seal failure, it can be released. Hence, this activity needs to be hybridized with technology to permanently sequester the CO_2. These include WAG stages (water after gas) where water is injected to inhibit or restrict desorption, injecting treated water to encourage precipitation and cementation of cleat systems and other methods.
4. **Induced Seismicity:** All injection zones will need to be certified to de-risk the occurrence of induced seismicity. (Refer to Section XIII, Risk Assessment)
5. **Breakthrough:** The efficacy and sequestration potential of flue gas is uncertain. Laboratory experiments suggest favorable opportunities. The precise composition of the flue gas is also relevant as are in-place scrubbing operations. Nitrogen breakthrough may precede carbon dioxide breakthrough. This means that nitrogen may reach the production wells earlier than carbon dioxide. This may not be an issue if the nitrogen reaching the production wells can be simply vented but it suggests a limit to efficient sequestration operations when the arrival of nitrogen is detected.

V. Resource Evaluation for the Uinta Basin

Are there possible subsurface coalbed methane seams near the Hunter and Huntington plants and could there be merit of sequestration in these? From public domain sources

(UGS[7] data in particular), possible injection locations, capacities, advantages, and challenges for ECBM were assessed in a high volatile bituminous coal Uinta basin field located adjacent to the Hunter and Huntington plants. This is the Buzzard Bench field. The evaluation program entailed the following generic methodology.

1. Determination of the CO_2 injection rate and storage capacity in a candidate field in the Uinta Basin, a High Volatile Bituminous Ferron/Emery coal,
2. CO_2 breakthrough time in a typical scenario, and,
3. Evaluation of the amount of ECBM recovery for a pilot-scale operation.

To achieve these goals, a three-dimensional, dual-porosity geologic model was constructed using Petrel, a Schlumberger geologic modeling software package. The model was built with available hydrocarbon well data from public sources (Utah Division of Oil Gas and Mining, 2021). After that, a series of reservoir simulations was performed using Eclipse 300, a compositional flow simulator also developed by Schlumberger. The reservoir simulation model was calibrated against actual methane production using a history match before simulating the injection and storage capacity of CO_2 and the corresponding ECBM recovery in a Buzzard Bench scenario.

V.1 Site Description and Model Development

The Uinta Basin is located primarily in eastern Utah, with a small part extending into northwestern Colorado. It is structurally separated from the Piceance Basin by the Douglas Creek Arch and covers an area of about 14,450 square miles (Adams & Kirr, 2021). The Ferron Sandstone unit signifies one deltaic sedimentation episode into the foreland basin. The Upper Cretaceous (~90 MA) Ferron Sandstone was deposited in a fluvial-dominated deltaic system. This deltaic environment produced substantial coal deposits (Ryer, 1991). The setting consists of fine- to medium-grained deltaic sandstones and coalbeds with an average coal thickness of 24 feet (Burns and Lamarre, 1997). The coal was formed in peat swamps behind the Vernal delta's delta-front shoreline sandstones (Hale and Van De Graff, 1964). The Buzzard Bench field is located west of Orangeville, in Emery County, within the Uinta Basin. It is along the San Rafael Swell's western flank and towards the east of the Wasatch Plateau in Central Utah (Figure 6). The field is in Township 16S to Township 19S, and Range 7E to Range 8E (Utah Township, Range, and Meridian, 2006). The CBM discovery well was drilled in late 1994 by Texaco Exploration and Production, Inc. (Lamarre, 2004).

Two coal-fired power plants are located within the Buzzard Bench field (Figure 6). These are the Hunter and Huntington plants, operated by Rocky Mountain Power. These plants are potential suppliers of flue gas; CO_2 is a component of this. Finding a subsurface domain to sequester the flue gas or the CO_2 emissions would be desirable.

[7] Utah Geological Survey

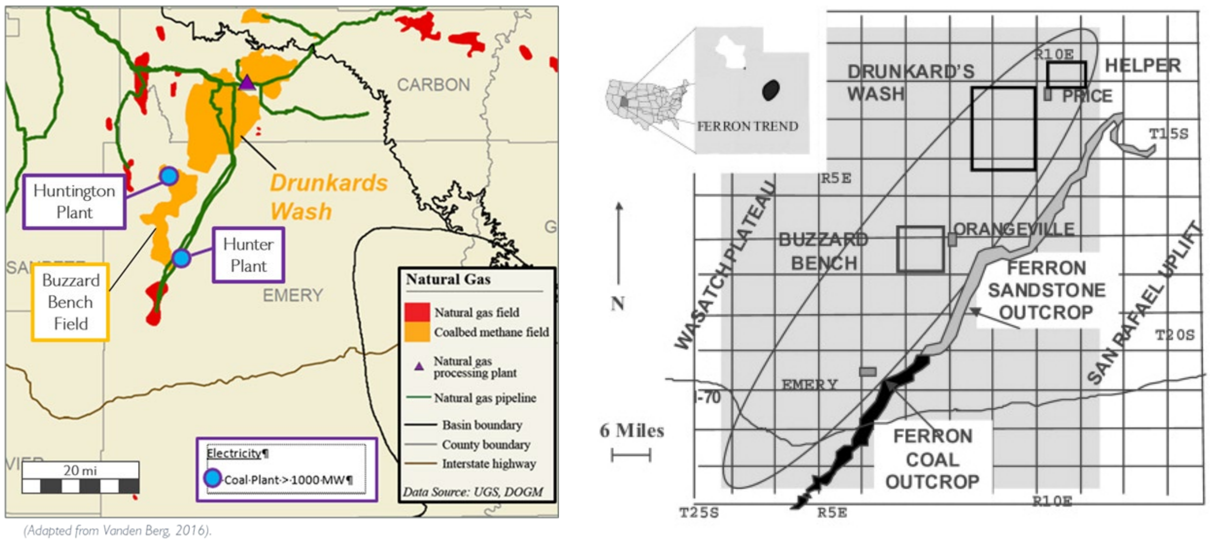

Figure 6. The relative location of the power plants and the Buzzard Bench field is seen in the left-hand panel (van den Berg, 2016). The Buzzard Bench field produces from the Ferron coal. At right, the Ferron coalbed (80 miles) long, extending from north of Price to south of Interstate 70; outcrops in the western part of the San Rafael Swell. The Ferron coal outcrop is exposed within the black shaded region and in the subsurface extends in the grey shaded region (Lamarre, 2004).

The Huntington power plant is in the northern part of the Buzzard Bench field. There are multiple nearby wells (as seen in Figure 7) with varying recent production histories.

The Ferron coalbed methane trend is approximately 80 miles long and 10 miles wide, with the shallowest coals encountered at depths of 2845 ft on the east side of the field near the San Rafael uplift. The deepest coals are found at a depth of 4100 ft to the west under the Wasatch Plateau (Lamarre, 2004). Some of the cored coal samples contain very few cleats, while others show well-developed cleats. However, productive wells located adjacent to faults indicate enhanced permeability (Lamarre, 2004). *Implications: The coals are deep enough to afford isolation particularly with the overlying Mancos shale (see next paragraph). Presumably, the reservoir pressure is near hydrostatic. Some compression will be required to inject CO_2 – more so for less dense flue gas.*

The Blue Gate shale, part of the Mancos shale, with a thickness between 1400 and 2000 feet, overlies the Ferron unit and serves as a potential upper seal for the Ferron coal (Condon, 2003). This is very important from a sequestration perspective because this thick sequence will prevent the migration of injected CO_2 to the surface. During injection, there can be free carbon dioxide locally – above the adsorbed capacity. The Ferron unit is also underlain by the Tununk Shale (Figure 8). *Therefore, with super- and* *subjacent barriers to leakage, the Ferron coal units are potential candidates for CO_2 sequestration.*

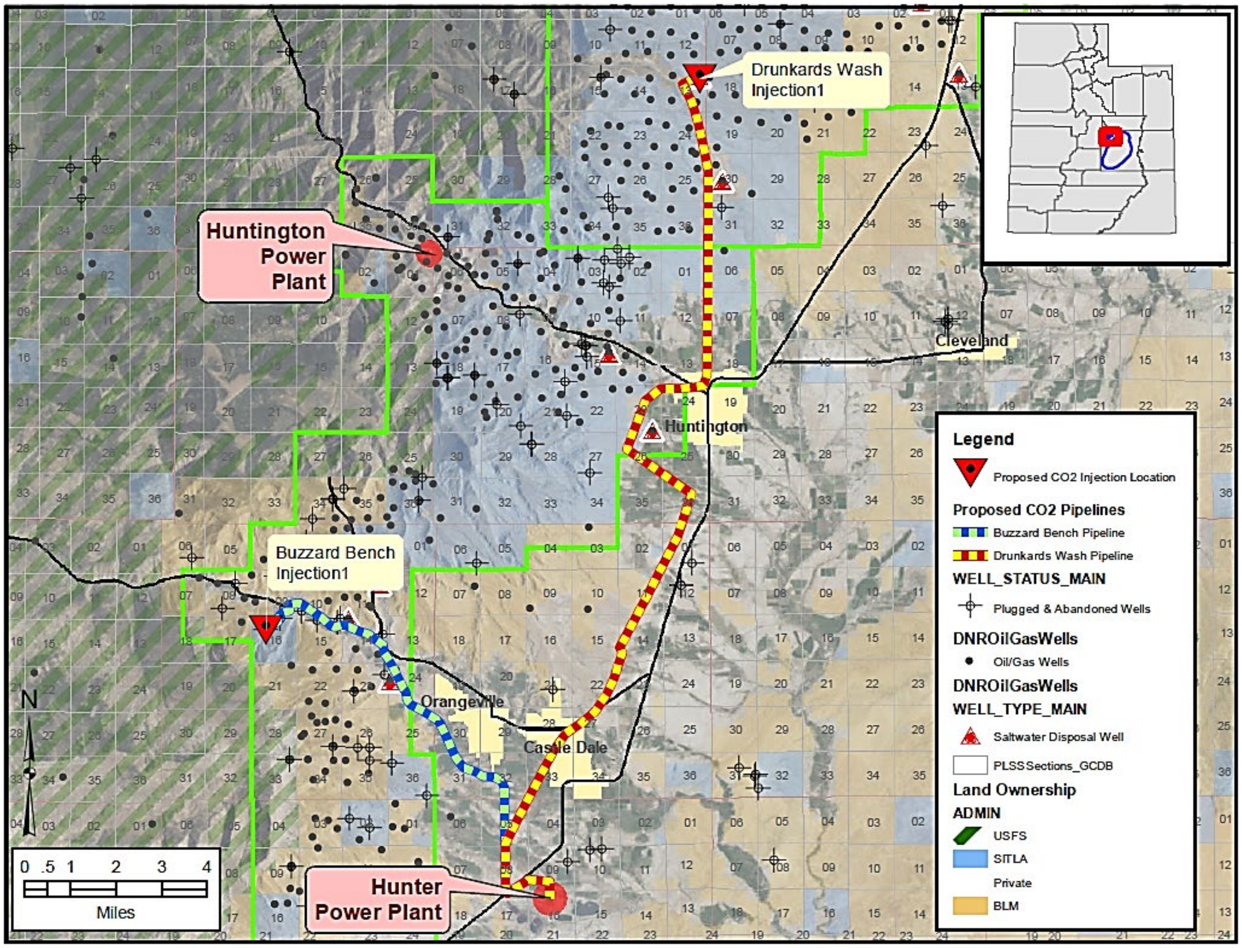

Figure 7. Location of the Buzzard Bench field, indicating the Huntington Power plant's location and the wells in the field (modified from McPherson et al., 2018).

Coalbeds have been characterized as systems comprising micropore (primary) and macropore (secondary, i.e., cleat) porosity. Almost all gas-in-place (or sequestered) is stored in the primary porosity by adsorption, while the secondary porosity (cleat systems) provides conduits for gas migration. The matrix permeability is negligible. The migration of gas from the coal matrix into the cleats and a wellbore occurs by desorption, diffusion, and pressure-driven flow. Therefore, it is relevant to model this complex heterogeneous system comprising cleats and overlying seals to investigate the migration and retention of CO_2 within the reservoir.

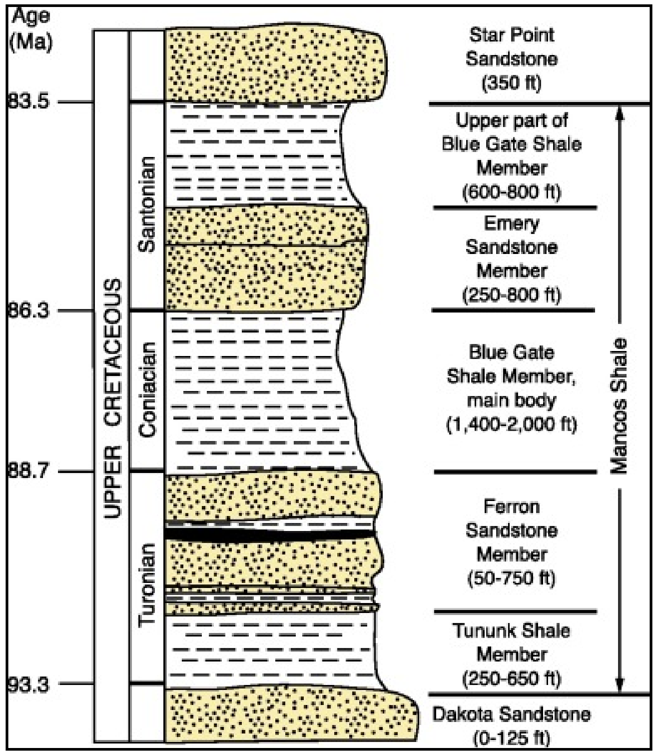

Figure 8. Stratigraphic column. The thicknesses of the geologic units are not drawn to scale (after Condon, 2003).

Over the last few decades, there has been modest natural gas production from the coals in the Buzzard Bench field. Some readers might be more familiar with ConocoPhillips' operations in the Drunkards Wash field just to the north of the Buzzard Bench field. Figure 9 shows gas well locations and shows a natural partitioning of the Buzzard Bench field into a northern and southern block. This study focused on the northern block because of the proximity to the power plant.

V.2 Geological Model

A three-dimensional geologic model was built with a geostatistical tool in Petrel™, a Schlumberger geologic modeling software package. The software is used for seismic, structural, and stratigraphic interpretation. The available data were incorporated into the three-dimensional model to visualize the reservoir and its characteristics. The software's geostatistical routines populated the grid with petrophysical properties using spatial correlation. Stochastic and geostatistical techniques allow heterogeneity to be introduced in both vertical and horizontal directions, thereby creating a representative geologic model. The model was initially used for volumetric calculations. Thereafter, the model was used to forecast methane production performance and subsequently for CO_2 injection. Historical production data were used for the calibration of the model.

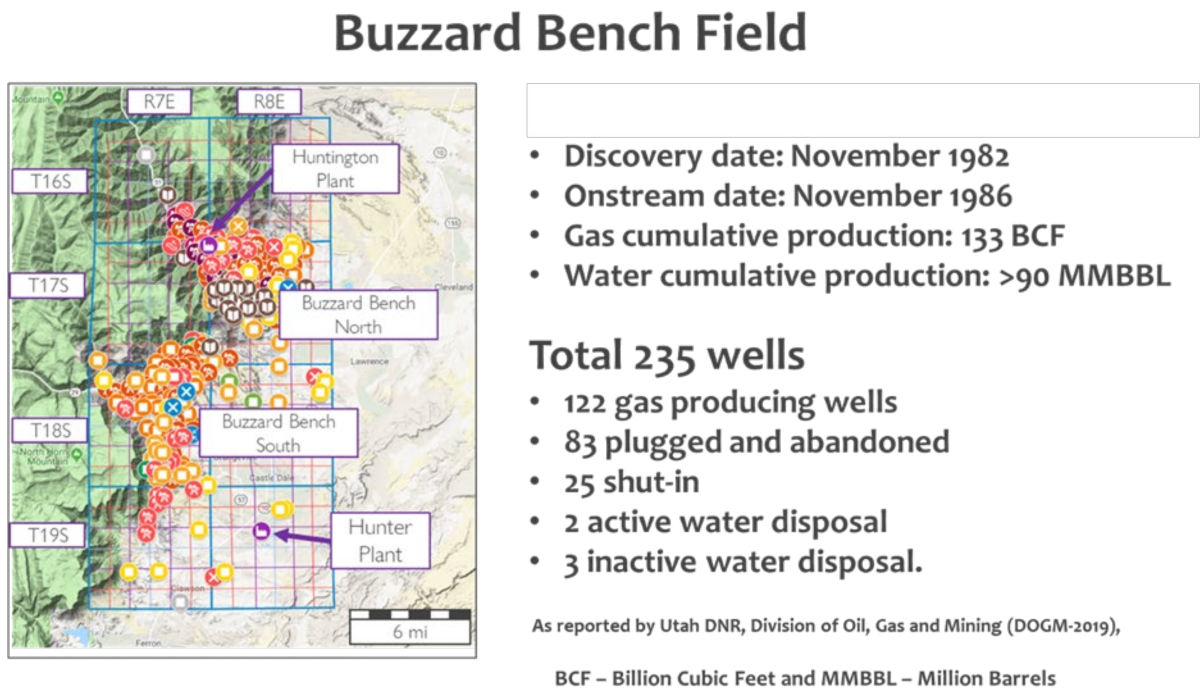

Figure 9. Well locations and a synopsis of gas production history for the northern and southern blocks of the Buzzard Bench field.

V.3 Petrophysical Parameters

Petrophysical properties, such as permeability, water saturation parameters (e.g., cementation factors), porosity, and adsorptive capacity significantly impact a field's volumetrics and performance during carbon dioxide injection (Li et al., 2011). Public domain petrophysical logs were obtained from the Utah Division of Oil, Gas, and Mining (State of Utah Division of Oil Gas and Mining, 2019). These legacy data were digitized using the Neuralog well logging software suite. Over 70 well logs were used to build the model. A density cut-off of 1.75 g/cm^3 was used to identify the coal units.[8] Coal was inferred in zones with values less than this threshold. To simplify analysis and make reservoir simulations tractable, a gamma-ray count below 100 GAPI was used to discriminate between sandstone and shale. Six coal units (M, J, I, G, C, and A) were identified from the log interpretation (Figure 10). These units and the nomenclature are consistent with other categorizations for the Ferron coal (Ryan, 1991). As implied, three generic facies (sand, shale, and coal) were identified to make numerical simulation tractable.

[8] Presuming some ash present.

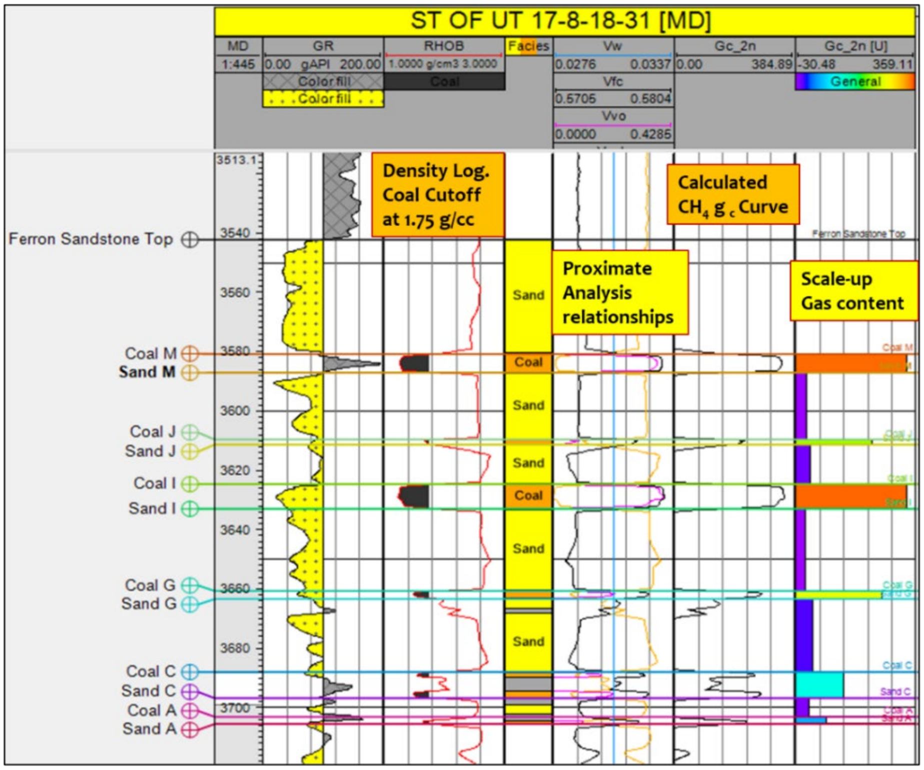

Figure 10. An example interpreted log from well ST OF UT 17-8-18-31. Six different coal seams (Coal M, J, I, G, C, and A) were identified. The lateral continuity of each coal seam can be traced between adjacent wells.

Available core data from the Ferron formation and the Blackhawk formation,[9] a Cretaceous formation consisting of thick laterally continuous coal beds and a similar depositional environment to the Ferron formation were used to estimate the coal matrix porosity. These measured porosities were correlated with density log values and regressed for an acceptable estimate of porosity (Figure 11). The sandstone's porosity was estimated using density log data (equation 1). These coal-derived porosities and sandstone-derived porosity logs were then merged through Petrel's calculator function using conditional logic. For the coal, the cleat porosity was also estimated. The so-called cleat porosity is the ratio of the cleat network volume to the total bulk volume of the coal. The cleats provide channels for fluid movement (Jie et al., 2014).

$$\phi = \frac{\rho_{ma} - \rho_b}{\rho_{ma} - \rho_f} \quad \textbf{(1)}$$

[9] The Blackhawk is a Cretaceous formation which consists of thick, laterally continuous coalbeds like those found in the Ferron formation. It is in Eastern Utah, partly overlaying the Mancos shale and near the Ferron formation. Both are Cretaceous Formations and in the Uinta Basin. The porosity data available from the Ferron formation came from two data sources, for better data quality, analogue data (Blackhawk formation) were included to make an informed evaluation.

where ϕ is the porosity; ρ_{ma} is the matrix density (2.65 g/cm^3; a sandstone matrix had been used for the logs); ρ_b is the bulk density (from well logs), and ρ_f is the fluid density (1.0 g/cm^3).

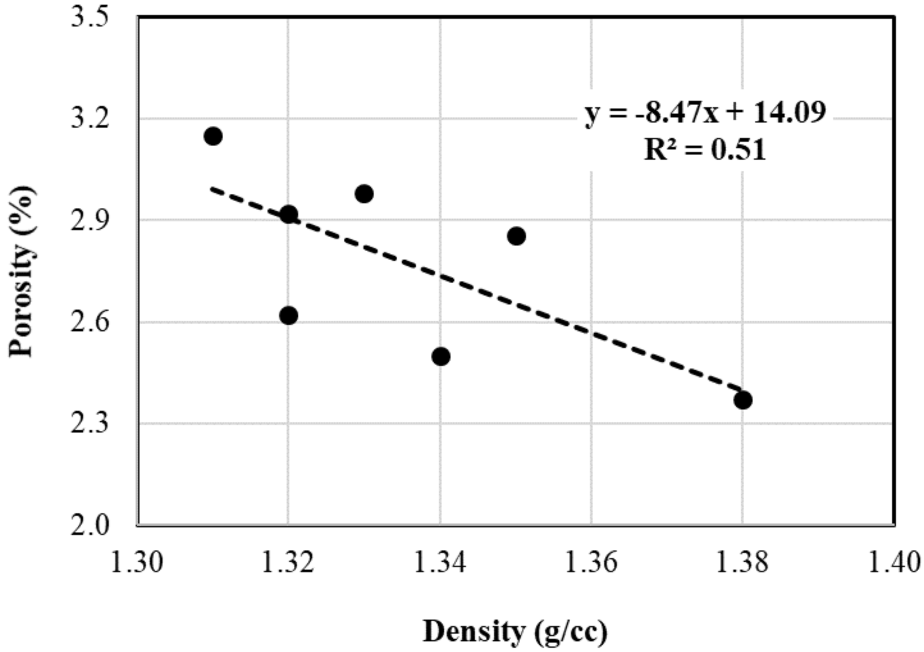

Figure 11. Porosity density cross plot showing regression coefficient of 0.51. While this is a relatively small regression coefficient, it is acceptable for the calculations carried out.

A relationship was established between the deep and shallow resistivity and the porosity (using the methodology of Boyeldieu and Winchester, 1982) to infer the cleat porosity. In that relationship used for building the cleat porosity model, a cementation exponent (m_f) of 1.3 was used. This value of the cleat cementation exponent is related to the coal's pore geometry since it reflects the difficulty of fluid flow (Yang et al., 2019). This value for the cementation exponent is lower than for conventional oil and gas reservoirs. For consolidated, shale-free sandstones, *m* ranges from 1.8 to 2. Rocks with low porosity but a well-developed fracture network have cementation factors closer to unity since the network has flow paths that are reasonably direct (Glover, 2010). 0.5 ohm·m was used in the equation as an average mud filtrate resistivity. This value was arbitrarily obtained from the headers of legacy wireline logs available from DOGM. The simplified Archie model (Yang et al., 2006) (equation 2) was used for building the cleat porosity model.

$$\phi_f = \left(\frac{R_{mf}}{R_{lls}}\right)^{\frac{1}{m_f}} \qquad (2)$$

where ϕ_f is the cleat porosity; R_{mf} is the mud filtrate resistivity (ohm·m); R_{lls} is the shallow lateral resistivity (ohm·m), and m_f is the cementation factor. In this model, m_f = 1.30 ohm·m and R_{mf} = 0.50 ohm·m.

Figure 12 shows a three-dimensional map of the cleat porosity for one seam of the Ferron Coal in the northern block of the Buzzard Bench field (see approximate demarcation in Figure 9). About 80% of the cleat porosity values are between 0.05% and 2.25%, with an average value of 0.67%, a standard deviation of 0.49%, and a variance of 0.24%^{2}. These porosities are in the range expected for cleat porosity in CBM reservoirs (Palmer et al., 2011).

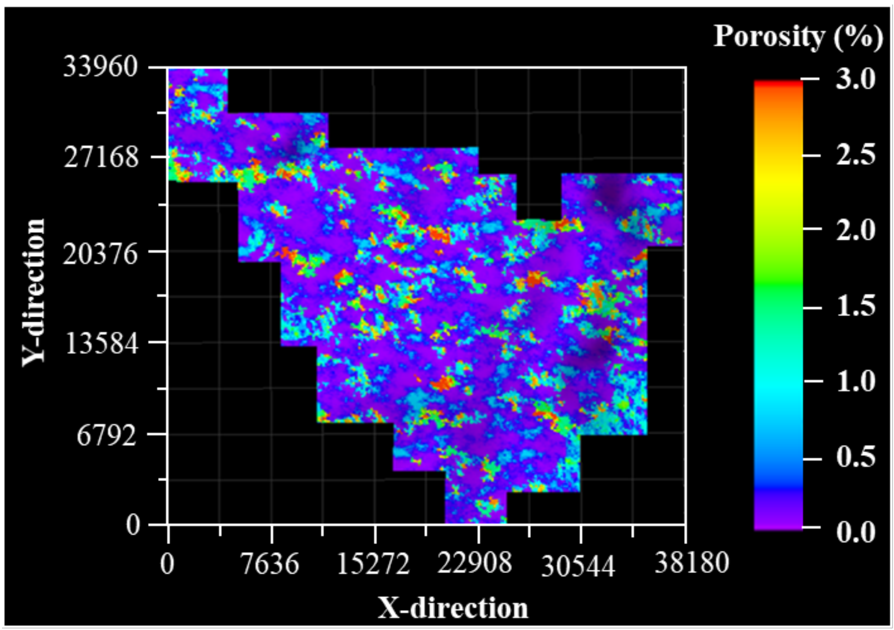

Figure 12. A plan view of the cleat porosity distribution for coal seam M. This coal seam's relative position in the stacking of the seams is shown in Figure 10.

In addition to porosity, permeability is an essential and difficult parameter to characterize for CBM production and CO_2 injection (Xue and Ohsumi, 2004). CBM reservoir permeability is regulated by coalification, geological structure, in situ stress, coal seam structure, depth of burial, syn-sedimentary and post-depositional processes, as well as cleating (Li et al., 2011). Later, during production, permeability changes due to variations in temperature, pressure, stress, deformation, adsorption, and moisture content (Tao et al., 2012). It is often assumed that the matrix permeability is low and is not immediately relevant to productivity (although diffusional properties will be relevant). Cleat permeability is generally used to represent coal permeability and assumed to control productivity (presuming the rate of desorption is not the limiting factor). The cleat permeability F-S model – designated after the two researchers who developed the formulation (Sibbit and Faivre, 1985) - was used to infer cleat permeability.

The technique uses a dual laterolog logging track and ad hoc estimates of cleat width. Since no references were available for inferring the cleat width in the Buzzard Bench coals, the cleat width was estimated from the dual laterolog and mud conductivity (Sibbit and Faivre, 1985) (equation 3).

$$w = \frac{C_s - C_d}{4C_m} \tag{3}$$

where w is the cleat width (μm); C_s, C_d, and C_m represent the shallow, deep, and mud conductivity (moh), respectively.

The cleat permeability was then approximated using a basic relationship between hydraulic conductivity and the cube of the aperture (equation 4). Refer to Figure 13.

$$k_f = 8.50 \times 10^{-4} w^2 \phi_f \tag{4}$$

where k_f is the cleat permeability (mD) and 1 mD ≈ 1×10^{-15} m^2. w is the cleat width (μm), and ϕ_f is the fracture porosity (decimal).

The calculated results using these F-S cleat permeability values range from 0.32 mD to 16 mD, with an average of 4.35 mD, a standard deviation of 2.67 mD, and a variance of 7.13 md^2 (Figure 13). These absolute permeabilities are close to the values of between 4 and 20 mD reported for permeability in the Ferron coal (Burns and Lamarre, 1997).

V.4 Scale-Up

Scale-up, a process of assigning the well log data to the grid cells, was carried out to build a simulation model from the geological data. The discrete (facies[10]) and continuous properties (porosity) were scaled up to a coarse grid using specific algorithms. The porosity was biased to the scaled-up facies to reflect the reservoir's heterogeneity.

After scale-up, a Sequential Gaussian Simulation (SGS) (algorithm for the stochastic characterization of properties) was used to populate the grid cells with petrophysical properties. The permeability histogram shows that about 96% of the grid cells' permeability values range from 0.32 mD to 10 mD, while the remaining 4% ranges from 11 mD to 18 mD.

[10] What is a facies? A facies is a geologic classification where the overall characteristics of a rock unit are used to reflect similar origin and differentiate the unit from others around it. Mineralogy, provenance, depositional environment, fossil content, sedimentary structures and texture distinguish different facies.

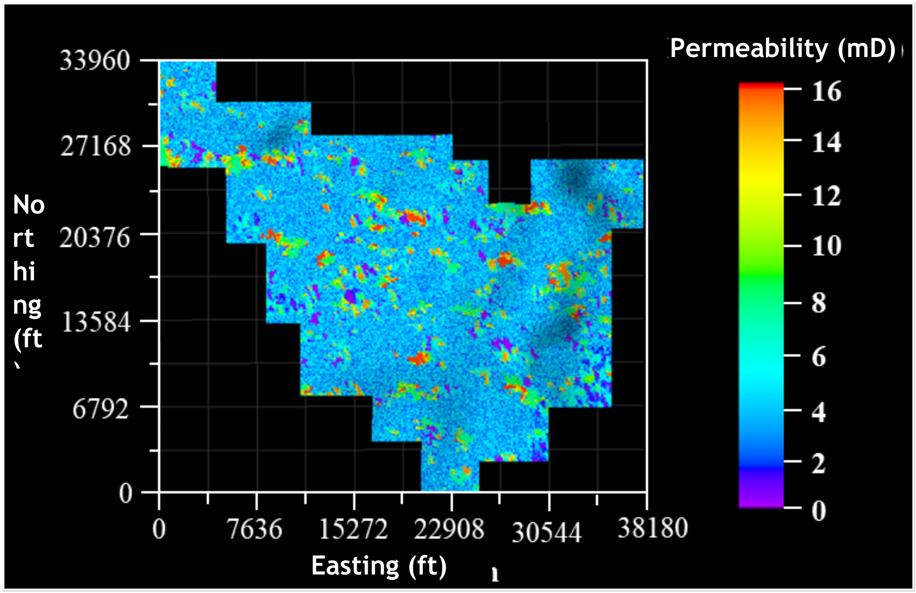

Figure 13. A plan view of the fracture permeability distribution for coal seam M.

VI. Ferron CBM Volumetric Estimations

The determination of gas-in-place (GIP) in a CBM reservoir requires (1) the area of the coalbeds, (2) the thickness of each relevant coal unit, (3) the average coalbed density (used for inferring gas content), and (4) the in-situ gas content (Dallegee and Baker, 2013). The reservoir pressure, water saturation in the cleats, and the so-called moisture content in the matrix are additional factors controlling the (GIP) of coal (Morad et al., 2007).

Proximate analysis was performed to characterize the coal before volumetric estimations. It involves heating the coal (pyrolysis) according to ASTM Standard D7582 to determine the moisture content (lost mass), volatile matter (non-aqueous gases formed from a coal sample during heating), fixed carbon (non-volatile fraction), and ash yield (remaining inorganic residue after combustion). It was carried out on representative samples of the Ferron coal (recovered from an underground coal mine). The samples were extracted from different laminations, where the coal texture appeared to be crystalline (bright hue) or dull (opaque coloration). The Ferron coal has a vitrinite reflectance (R_o%) of 0.6-08%, signifying a moderate thermal maturity (Montgomery, et al., 2001). The quantity of methane generated and expelled from coal is related to thermal maturity and gauged by the coal rank (Pashin, 2020).

Table 2 shows the results for the proximate analysis for four different samples from the Ferron coal.[11] This analysis indicates that the coal has a rank of High Volatile Bituminous B and C. As a rule of thumb, absorptive capacity increases with rank. The samples in

[11] The coals were classified using the gross calorific (heating) value from the proximate analysis. High volatile Bituminous B to C coal has a calorific value range of 11,500 to 14,000 Btu/lb.

Table 2 were acquired from an underground coal mine in Emery County. During coalification (as coals are formed), coals increase in rank from lignite to subbituminous, to bituminous, and finally to anthracite. A coal's rank directly influences the gas storage capacity of coal (Seidle et al. 1995). Bituminous coal[12] has a lower moisture content but a higher volatile content and heating value than subbituminous coal. Bituminous coal represents more than 47% of the nation's coal production (EIA 2019). The higher coal ranks have a higher percentage of carbon since moisture and volatiles are driven off during coal maturation (under temperature and pressure in situ) leaving carbon behind. With the increase in carbon content, there is also an increase in the heat content of a coal (Ali, 2004).

Table 2. Average proximate analysis results of mined coal seam samples from the Ferron coal

Moisture (%)	3.07
Ash (%)	7.93
Volatile Matter (%)	36.95
Fixed Carbon (%)	52.06
Sulfur (%)	0.42
Calorific Value (Btu/lb)	12,848

The density logs and proximate analyses were used to generate a gas content profile, which is unique for each well in the field. The fraction of the ash volume (V_{ash}) is derived from the density log by estimating the proportion of the bulk density compared to the nominal values of coal and ash[13] (equation 5).

$$V_{ash} = \frac{\rho_{bulk} - \rho_{coal}}{\rho_{ash} - \rho_{coal}} \quad (5)$$

where ρ_{ash} is the density of ash assumed at 2.65 gm/cm^3, ρ_{coal} is the nominal density of bituminous coal 1.24 gm/cm^3 (Sutton, 2014), and ρ_{bulk} is the log density curve RHOB (gm/cm^3).

[12]"Bituminous coal is a middle rank coal between subbituminous and anthracite. Bituminous coal usually has a high heating (Btu) value and is used in electricity generation and steel making in the United States. Bituminous coal is blocky and appears shiny and smooth when you first see it, but look closer and you might see it has thin, alternating, shiny and dull layers." after https://www.usgs.gov/faqs/what-are-types-coal?qt-news_science_products=0#qt-news_science_products

[13]Ash would be considered as residue after a coal is combusted – e.g., silica (silt) or clays (montmorillonite), calcite present in minor quantities in coal.

A continuous curve for ash volume is obtained, covering the same interval as the density log. A three-dimensional grid was generated by upscaling the calculated gas content using equation 6. Gas content is the volume of gas in a unit mass of coal (Saghafi, 2017).

$$\mathrm{G_c} = \mathrm{G_c}\ (\text{sample}) - \frac{\mathrm{G_c}\ (\text{sample}) \times \mathrm{V_{ash}}}{0.8 \times (1 - \mathrm{V_w})} \tag{6}$$

where G_c is the gas content per ton of coal (scf/ton coal), G_c(sample) is the maximum volume of gas that can be adsorbed into the coal matrix (in-situ G_c was set at 350 scf/ton coal for methane for the simulations), V_{ash} is the volume of ash, and V_w is the moisture content (amount of water present in the moist sample). **Actual isotherm measurements are somewhat less than this estimate - Figure 14.** Those samples had an ash content of 4.20% and an equilibrated moisture content of 5.14%. At 1500 psi, for these samples, the estimated in situ methane would not exceed 265 scf/ton daf.[14] The higher value is from published data so the estimate might be optimistic.

The estimated gas content values (now available on a foot-by-foot basis in each well) were then upscaled to the three-dimensional geo-grid cells. The grid cells were stochastically populated with the gas content values using the SGS algorithm. This was carried out for all wells. The field's overall gas-in-place GIP assessment was calculated by multiplying the computed gas content by the total coal mass of the Ferron coals. The estimated static GIP in the northern block of the field is 153 to 202 bcf methane (using typical gas contents of 190 and 350 scf/ton, respectively for worst- and best-case scenarios). The estimated GIP for the southern block ranges from 192 to 450 bcf methane. Some of this gas has been already produced because of coalbed production operations over the past twenty years or so.

The isotherm in Figure 14 was generated on Ferron coal by Schlumberger, who also generated an isotherm of pure carbon dioxide (Figure 15). Using the isotherm data in Figure 15, the dry-ash free CO_2 gas capacity of the Ferron coal at in-situ conditions is 670 scf/ton, **which leads to a volumetric capacity of carbon dioxide of 523 and 673 bcf of CO_2, for the northern and southern Buzzard Bench blocks, respectively.**

VII. Development of the Reservoir Model

VII.1 Gridding

Before simulating the injection and storage of carbon dioxide, the reservoir model was calibrated against actual methane production from selected wells in the Buzzard Bench field. Schlumberger's Eclipse 300 flow simulator was used to describe the combined mechanisms of Darcy flow, gas adsorption, desorption, and diffusion in the coalbed methane reservoir. Discretizing the reservoir into small grid blocks allows for accurate tracking of fluid fronts and pressure gradients through the reservoir with time. The flow

[14] daf indicates dry, ash free.

equations' solutions are computed for finite time intervals (time steps) in each of the discrete grid blocks. With numerous grid blocks, solving the underlying finite difference equations required significant computational overhead.

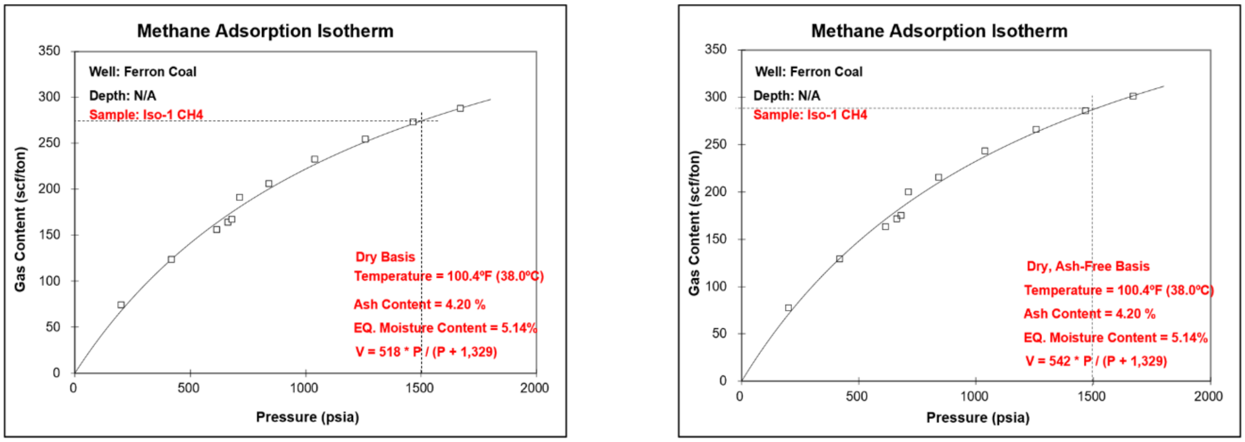

Figure 14. Adsorption isotherm for methane was performed on a Ferron coal sample.

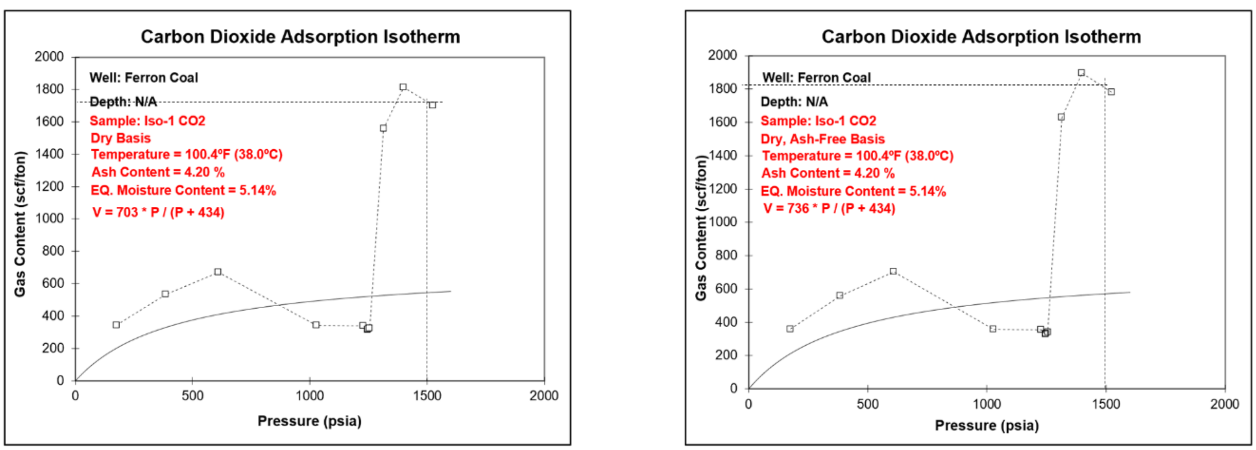

Figure 15. Adsorption isotherm for carbon dioxide was performed on a Ferron coal sample. The CO_2 - under supercritical conditions - considerably increases the storage capacity, in addition to the high adsorptive capacity due to molecular interactions.

The coalbed methane (CBM) model was constructed as a dual-porosity model with a very low or negligible permeability matrix, coupled to a medium to high permeability fracture (the cleats) network. The matrix, which contains the absorbed gas, has limited *effective* porosity and permeability (Palmer and Mansoori, 1996). Darcy flow between the matrix and the fracture (cleat) system is not considered since there is anticipated to be negligible flow from one matrix block to the next. This differentiates the dual-porosity system for a sorption-dominated system from a conventional dual-porosity system. However, the coal cleats or natural fractures are represented by Darcy flow, and they are typically filled with water before the onset of primary production. Permeable flow occurs through the cleats. The dominant cleat is called the face cleat. The butt cleat is oriented roughly perpendicular to the face cleat (Rodrigues et al., 2014). The fracture permeability is assigned to be the same in both the x- (face cleat), and z- (vertical) directions[15] in this coal (i.e., ash layers are ignored; ash layers would be thin low permeability impediments to vertical flow) and one-tenth of this value for the y- (butt cleat) direction since the face cleats are generally more conductive than the butt cleats and the butt cleats are more discontinuous. This assignment was generally supported by physically viewing the coal in situ in an underground mine.

The study area for CO_2 injection and sequestration incorporated two existing CBM production wells and two wells converted to be hypothetical CO_2 injection wells. It is anticipated that there will be methane production and that these same production wells may also serve as monitoring wells. Both the selected production and injection wells are in the northwestern area of the field. At this location, the average depth to the top of the coal is about 3500 ft, with an average reservoir pressure of 1500 psi, assuming a pressure gradient of 0.43 psi/ft. There are six different coal units within the Buzzard Bench field. The actual four wells used in the simulation have previously been hydraulically fractured as part of production operations. The coals in these wells were perforated with 0.88-in diameter holes, six shots per foot, with 60-degree phasing. These wells were hydraulically fractured using crosslinked fracturing fluid. Each of the wells had two to three hydraulic fracturing stages, suggesting possible targets other than the coals although the coals are assumed to be the primary production zones.

To adequately capture the heterogeneity and variations in gas composition during production and injection of CO_2 for ECBM production, compositional effects must be considered in the modeling. The three-dimensional static model (as described above) was imported into the ECLIPSE compositional simulator (E300) for the reservoir simulation. This compositional simulator incorporates both geological and petrophysical models for the reservoir. A fully implicit solution method was employed for the corner point orthogonal grid. The aim was to reduce material balance errors. Pressures and saturations calculated in the grid blocks containing the production wells were used to calculate production rates,[16] and the calculated grid pressures were corrected to formation face pressures using Peaceman's equations (Peaceman, 1978). There were 1,432,882 (382 x 341 x 11) grid cells. The locations of the wells are shown in Figure 16.

---

[15] The coordinate system in the model is a Cartesian x,y,z system.

[16] As carbon dioxide is injected at the two injectors, methane is initially produced from the production well pair. Ultimately, some carbon dioxide reaches the production wells.

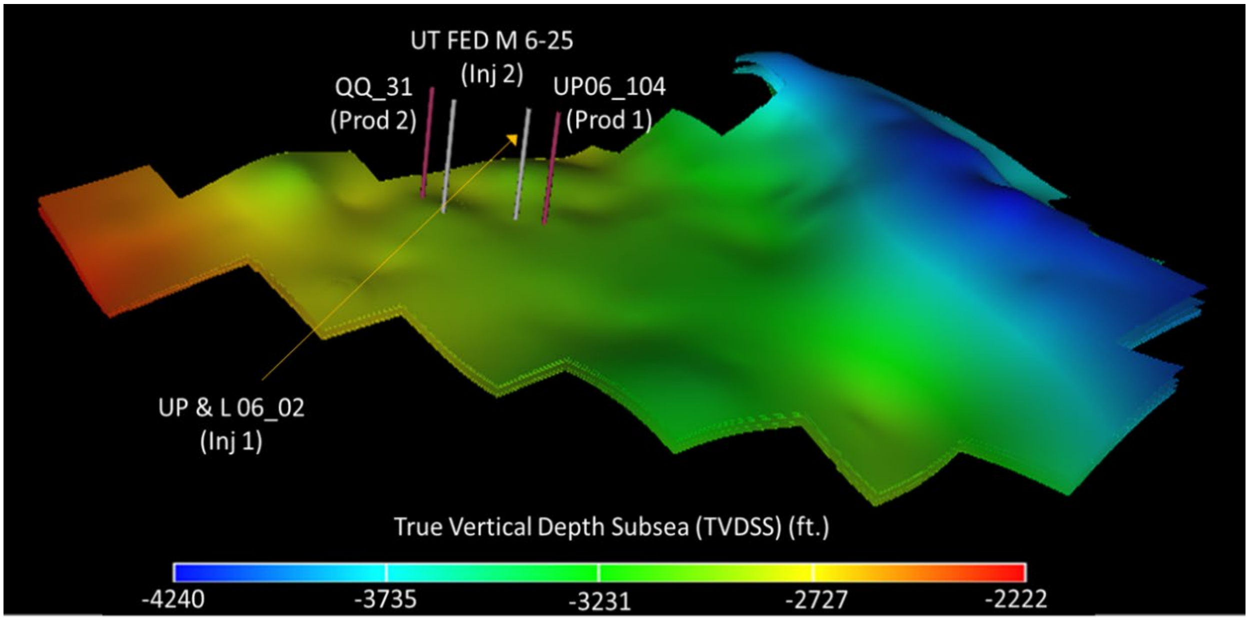

Figure 16. A three-dimensional depth map showing the locations of two CH_4 producing wells history matched and two injection wells. The wells were actual wells in the field (with available logging and production data). Two of these wells were hypothetically converted to injectors.

The reservoir reference pressures, PVT properties, depths, and the Langmuir isotherm parameters were specified to enable calculating the initial GIP.[17] The OGIP obtained from this dynamic model is 204 bcf, which is close to the estimation from the static model (202 bcf) for the northern block of the Buzzard Bench field. The difference is less than 1%, ensuring acceptance of the dynamic model as a realistic (if not unique) representation of the Buzzard Bench field's ultimate productive potential.

VII.2 History Matching

As indicated, a model was built to approximate the reservoir from a discrete number of measurements (well logs, etc.). How does one assess the reliability of this assumed representation? The standard method is to run simulations of production history and compare those predictions with measured production. By adjusting the parameters used to represent the reservoir, a history match can be established where forecasted and measured production agree (to the extent that is possible). History matching is performed to reduce uncertainty, characterize the reservoir, validate the reservoir simulation model, and enhance prediction accuracy. The general assumption is that if the reservoir model can replicate past reservoir performance, it can predict future performance. By running the simulator over historical production periods where production data are available, the reservoir descriptions used in the models can be modified and validated, and the differences between calculated (simulation) and

[17] OGIP indicates original gas in place; GIP indicates gas in place.

measured production (history) can be minimized. Several parameters can be adjusted either locally or globally to minimize the difference between the observed data and the simulation results, although some parameters are more sensitive to changes than others. For example, if lowering both the cleat porosity and relative permeability to water within reasonable limits fails to curtail high water production, the initial water saturation in the cleat – usually set at almost 100% - may be lowered.

The following adjustments were employed to obtain a history match to enable an adequate representation of the reservoir performance.

- absolute cleat permeability,
- cleat porosity,
- skin factor,
- gas-water relative permeability curves (ratio of k_{rw} to k_{rg}),
    - Corey exponents for water,
    - Corey exponents for gas,
    - k_{rw} and k_{rg} endpoints, and
- the ratio of vertical to horizontal permeability (k_v/k_h).

The wells selected for the modeling were chosen according to the following three criteria:

(1) their proven producing capacity,
(2) proximity to the Huntington power plant, and,
(3) favorable location on the geologic structure.

The production wells selected were UP06-104 (denoted as Prod 1) and QQ_31 (denoted as Prod 2). These wells have been actual producers in this field. The performance data targeted for matching are both measured gas and water production rates. For the history match, monthly water and gas production histories were available for these wells. These production data (historical) were expressed as gas and water production rates per day. Subsurface properties were adjusted iteratively until an acceptable quality of match was achieved. The history match metrics are assessed after each iteration to ensure that adjusted properties have the intended effect on the model's overall quality. Every simulation run is nonunique, and the order and extent to which each property is adjusted varies on a case-by-case basis. Some of the reservoir's descriptive data were not available; hence, relevant data from the literature (Olajossy, 2019) and experience-based engineering judgment were used (Table 3).

Table 3. Input parameters for history matching.

Initial pressure (psi)		1500	Estimated[18]
Temperature (°F)		120	Well logs[19]
Initial gas composition (%)	CH_4	100	Assumed[20]
	CO_2	0	
Initial water saturation (%)		90	
Initial gas saturation (%)		10	
Average fracture permeability (mD)		15	Simulation
Average fracture porosity (decimal)		0.006	
Average matrix porosity (decimal)		0.05	
Sorption time (day)		0.003	Simulation
Gas content (scf/ton)		350	
Gas gravity (air = 1)		0.65	
Langmuir pressure (psi)	CH_4	400[21]	
	CO_2	276	
Langmuir volume (scf/ton)	CH_4	350	
	CO_2	710	
Young's modulus (psi)		3×10^5	Olajossy, 2019
Poisson ratio		0.30	
Net thickness (ft)		1 - 24	Well logs
Formation compressibility (psi^{-1})		3×10^{-6}	Literature
Skin		-5	Stimulation[22]

A no-flow outer boundary was assumed since the selected production wells are surrounded by other producing wells, which came onstream at about the same time. A negative skin value was used to achieve the history match, signifying that the wells had been hydraulically fractured before production. Figures 17 and 18 indicate the final history-matched simulation results for the wells selected in the Buzzard Bench CBM play. The measured production data (history) are indicated with the dotted lines, while the simulated history (which is the calibration of the flow model) is indicated by the

[18] Presuming a hydrostatic pressure gradient of 0.433psi/ft

[19] Likely an underestimate of the static reservoir temperature.

[20] It is possible that there could be some naturally occurring gases such as carbon dioxide.

[21] Laboratory isotherm measurements on coal from an underground mine in Emery County gave a Langmuir pressure of 1329 psia and a Langmuir volume of 419 scf/ton.

[22] A skin of -5 is representative of a well that has been effectively hydraulically fractured, as these wells likely have.

blue lines. For this history match, gas is the dominant phase. Hence, the gas rate was chosen for matching which enables the corresponding water rates to be calculated according to their mobility and pressures. Adjusting the available parameters is a subjective process that requires an assessment of the model's sensitivities to the controlling parameters. Sensitivity analysis was conducted during the history match to determine the impact of each parameter on the match. The history-match quality metrics were then assessed after each iteration to ensure that the property adjustments had the intended effect on the overall model quality.

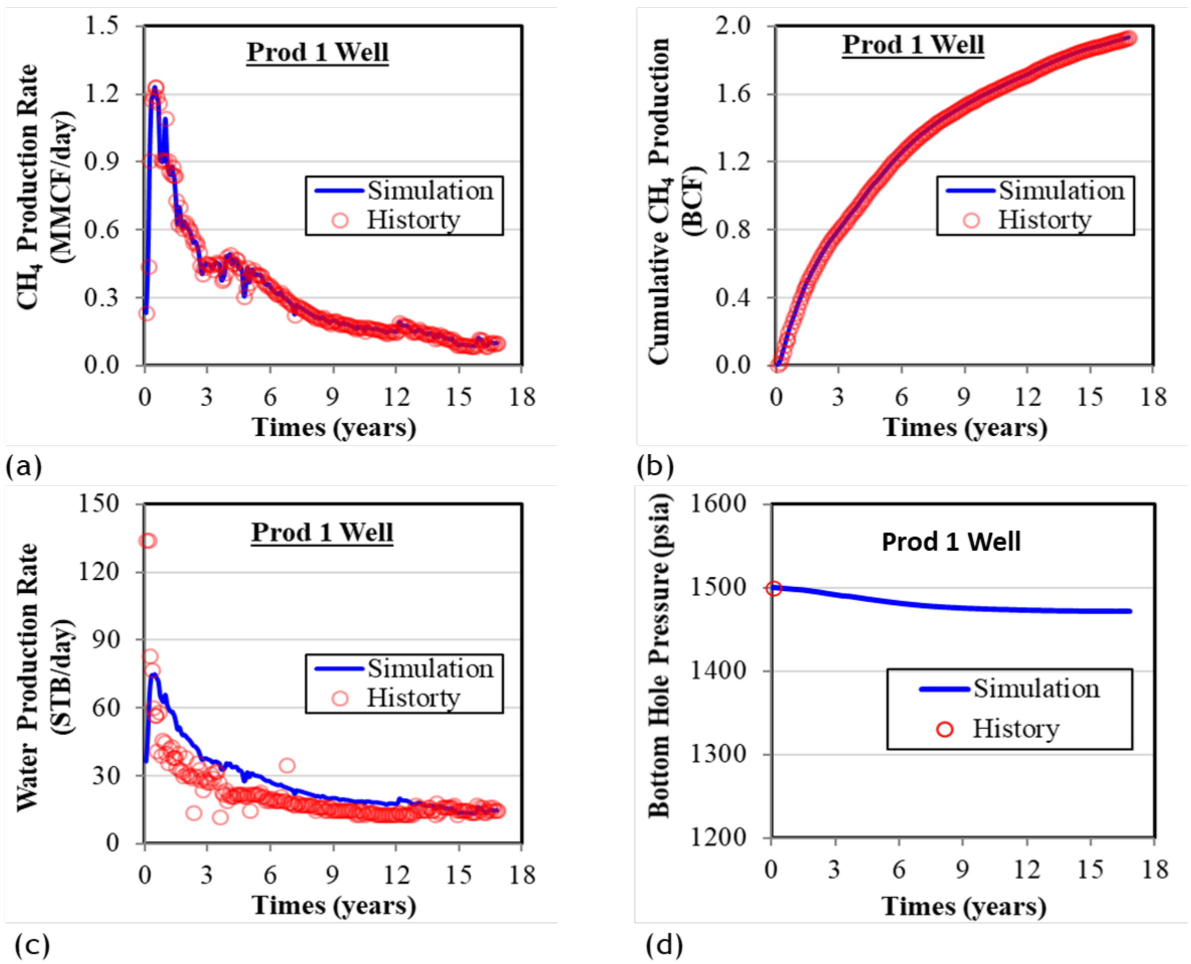

Figure 17. Validation of simulated results for the Production 1 well (UP & L 06-104) by history matching of (a) methane rate (b) cumulative methane production and (b) water rate and (d) bottom hole pressure. The match for gas production is good and that for water is adequate.

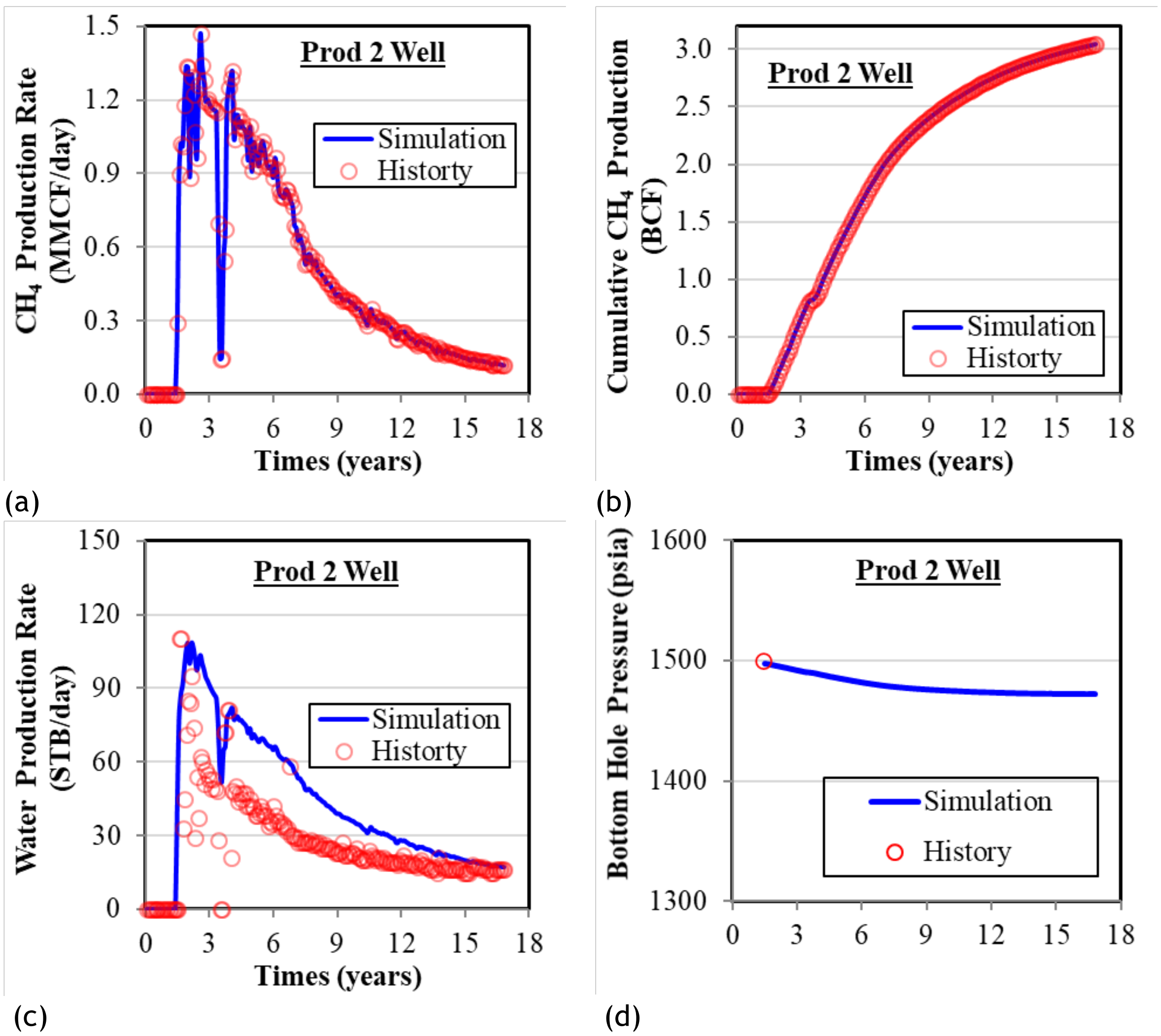

Figure 18. Validation of simulated results for the Production 2 well (St of Ut QQ 31-201) by history matching of (a) methane rate (b) cumulative methane production, and (b) water rate, and (d) bottom hole pressure. Water production is overestimated but gas production is well represented. The overall water production is small - hence the error can be tolerated.

Sensitivities were assessed and parametric variations were carried out on the relative and absolute permeabilities at different spatial locations to achieve the gas rate match. Sensitivity "tests" were conducted on the cleat porosity to obtain the water match since water is stored in the cleat porosity and this impacts the volume of water produced. Parametric variations were carried out within acceptable margins based on the available data. Threshold values are often defined to ensure that sensitivity modifiers are estimated only where valid simulated and historical data are available and are not adjusted beyond the defined threshold.

VIII. Simulation of CO_2 Injection and Sequestration Capacity

VIII.1 Considerations for CO_2 Injection – Hydraulic Fracturing

To evaluate the performance of a potential scenario where CO_2 is injected into the Buzzard Bench field to produce methane and sequester the carbon dioxide (CO_2-ECBM[23]) two currently producing wells, 'UP & L 06-102' (Inj 1) and 'UT FED M 6-25' (Inj 2) in the Buzzard Bench field, were numerically converted into injection wells. These injectors were selected due to their relative proximity to the power plants. The process must be cost-effective in utilizing these wells and converting them into injectors. The two wells that had been previously history matched, 'Prod 1 and Prod 2', were selected as methane producers since they had been the most prolific producers in the field. Under this configuration, it was presumed that CO_2 injection commenced in March 2019 and proceeded through February 2039 as an ECBM operation to sequester CO_2 and enhance methane production.

There are certain restrictions on the injection. By convention, the pressure needs to stay below the pressure to fracture the reservoir. With the thick overlying seal, some consideration should be given to relaxing this standard so that carbon dioxide can be moved deeper into the reservoir if permeability degradation occurs. However, the "no-fracturing" criterion was applied to these simulations. For that to be the case, the bottomhole pressure cannot exceed the minimum principal stress. Different reservoirs have different pressure and stress states. Generally, the least principal stress varies from 65% to 100% of the lithostatic stress[24] (Finkbeiner et al., 1996). To determine the maximum injection pressure, we assumed the least principal stress in the area to be 65% of the vertical stress. This put a constraint that the maximum injection pressure must be lower than the least principal stress to prevent additional fracturing of the reservoir. It is likely, however, that most wells were hydraulically fractured for primary recovery. This injection constraint will preclude additional fracturing if the injection pressure builds in the future. Using an average rock density of 2.5 g/cm^3 and an average depth of 3500 ft., the vertical stress was estimated to be 3400 psi (equation 7), while the least principal stress was estimated to be 2210 psi (0.65 x 3400 psi).

$$\sigma_v = 0.052 \int_0^h \big(\rho_r(1-\phi) + \rho_f(\phi)\big)dz \tag{7}$$

where σ_v is the total vertical stress (psi); ρ_r is the grain density (g/cm^3); ρ_f is the fluid density (g/cm^3); ϕ is the average porosity, z is the true vertical depth and h is the average reservoir depth (ft).

[23] Enhanced coalbed methane production

[24] Lithostatic stress is the vertical stress acting at a particular depth in situ – caused by the weight of the overlying material.

Therefore, the maximum injection pressure was constrained to 2100 psi (0.6 psi/ft) to avoid fracturing the coal and creating possible communication pathways. In the nearby Drunkard's Wash field, significant variations have been observed in the fracture gradient(minimum horizontal stress divided by true vertical depth) with values ranging from 0.65 to 1.4 psi/ft[25] (Conway, 1997). The Drunkard's Wash field is also a productive CBM play and is close to the Buzzard Bench field. This gives some confidence in the maximum value used for the injection pressure, equating the limiting threshold level to a pressure gradient of 0.6 psi/ft (a little below the assumed value for the minimum horizontal principal stress).

VIII.2 Considerations for CO_2 Injection - Swelling

Coal swelling occurs with the adsorption of CO_2. This reduces the cleat apertures which serve as pathways for flow, causing a reduction in coal permeability and a subsequent drop in injectivity. This phenomenon has been observed in CO_2 injection pilot projects (Reeves and Oudinot, 2005). Since coal matrix swelling associated with CO_2 adsorption is greater than shrinkage due to methane desorption, there will be a net reduction in permeability (Laxminarayana et al., 2004). To account for swelling due to CO_2 injection, the so-called Palmer and Mansoori model (Palmer and Mansoori, 1996) was incorporated in the simulation protocols. This model uses a cubic equation that provides a relationship between permeability and porosity and the equation of elasticity for strain in porous rock. Since fluid flow in coal cleats (and fractures when present) is described by Darcy flow, the absolute permeability is not constant but varies with the change in effective normal stress (stress perpendicular to the cleat minus pore pressure) and the effects associated with desorption and adsorption of gas in the coal matrix.

The Palmer-Mansoori model used in the simulations incorporates Young's modulus, the constrained axial modulus,[26] grain compressibility,[27] a porosity-permeability exponent,[28] and Langmuir parameters to account for the swelling effect during CO_2 injection. The model determines pore volume compressibility and permeability in a coal seam as a function of the effective stress and matrix shrinkage using equation 8.

$$\frac{\phi}{\phi_i} = 1 + c_f(P - P_i) + \varepsilon_L\left(1 - \frac{K}{M}\right)\left(\frac{P_i}{P_i + P_L} - \frac{P}{P + P_L}\right) \qquad (8)$$

where: ϕ is the fracture porosity; ϕ_i is the initial fracture porosity; c_f is the pore volume compressibility (1/psi); P_i is the initial pressure (psi); P is the pressure (psi); ε_L is a

[25]The high values are likely misinterpretation of treatment pressure data for inferring the minimum horizontal principal stress.

[26]This is the value of modulus that is calculated from a laboratory test where the sample is loaded along its axis, but lateral deformation is prevented by increasing the confining pressure – uniaxial strain loading.

[27]The compressibility of the solid components of a reservoir rock, in this case coal.

[28]Such as the commonly used cubic relationship.

fitting parameter to represent volumetric shrinkage strain (dimensionless) using an equation with a Langmuir shape; K is the bulk modulus (psi); M is the constrained axial modulus (psi), and P_L is the Langmuir pressure (psi). The second term on the right strictly indicates a dependency on effective stress change. The third term accounts for swelling associated with chemisorption.

VIII.3 Results and Discussion

Injection Rate Sensitivities and Effect of CO_2 Injection on Coal Matrix

Sensitivity exercises were carried out to infer the consequences of different injection rates for twenty years of carbon dioxide injection (after 16.8 years of primary methane production). This enabled determination of an optimal CO_2 injection rate for the selected wells. Figure 19 indicates that increasing the injection rate from 2 MMscfd to 2.5 MMscfd no longer substantially impacts the total amount of CO_2 injected and CH_4 produced. This signifies that the well has reached its maximum injection potential for the configuration considered (a small operation - two production wells and two injection wells).

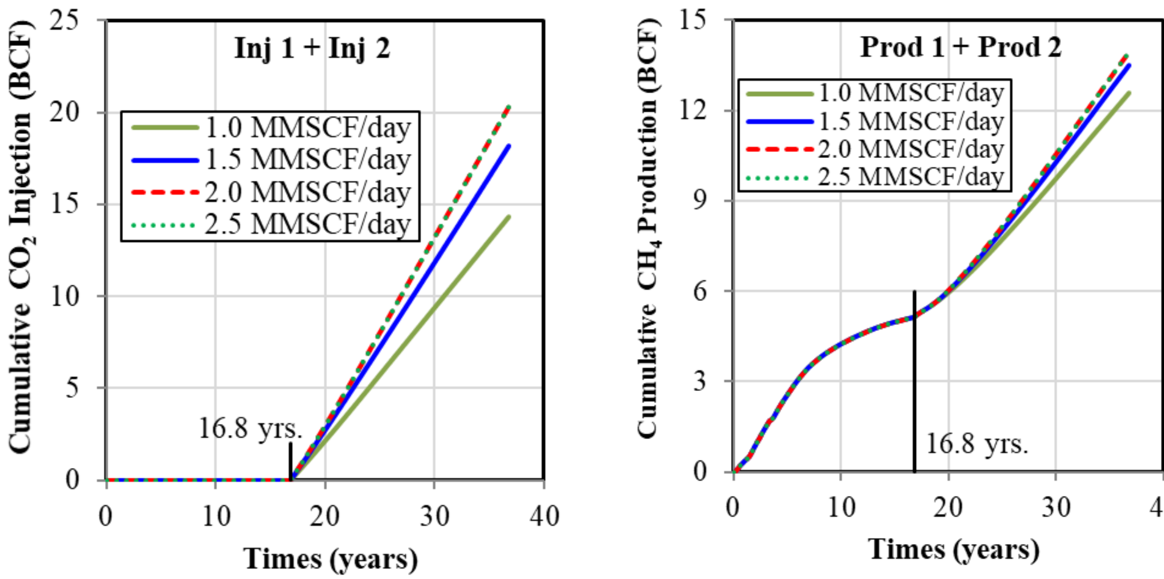

(a) (b)

Figure 19. The injection and production profiles with different CO_2 injection rates (a) the total volume of CO_2 injected by the two injectors, and (b) the total volume of CH_4 produced by the two producers.

Further simulation runs were then carried out to determine the impact of CO_2 injection on the coal seams at a maximum injection rate (2 MMscfd). Two runs were performed for each scenario considered. The first run did not incorporate the effect of coal swelling accompanying CO_2 injection, whereas the second run included coal swelling due to CO_2 injection. Figure 20 compares the results when swelling was and was not considered during CO_2 injection. The injected CO_2 caused the coal to swell, closing the cleats and reducing permeability. The results indicate that the total volume of CO_2 injected by the two injection wells over 20 years was reduced by 29% (28.6 bcf to 20.3 Bcf), while the total volume of CH_4 produced from the production wells was reduced by 19% (17.3 bcf to 13.95 bcf) (Figure 20) when swelling occurred.

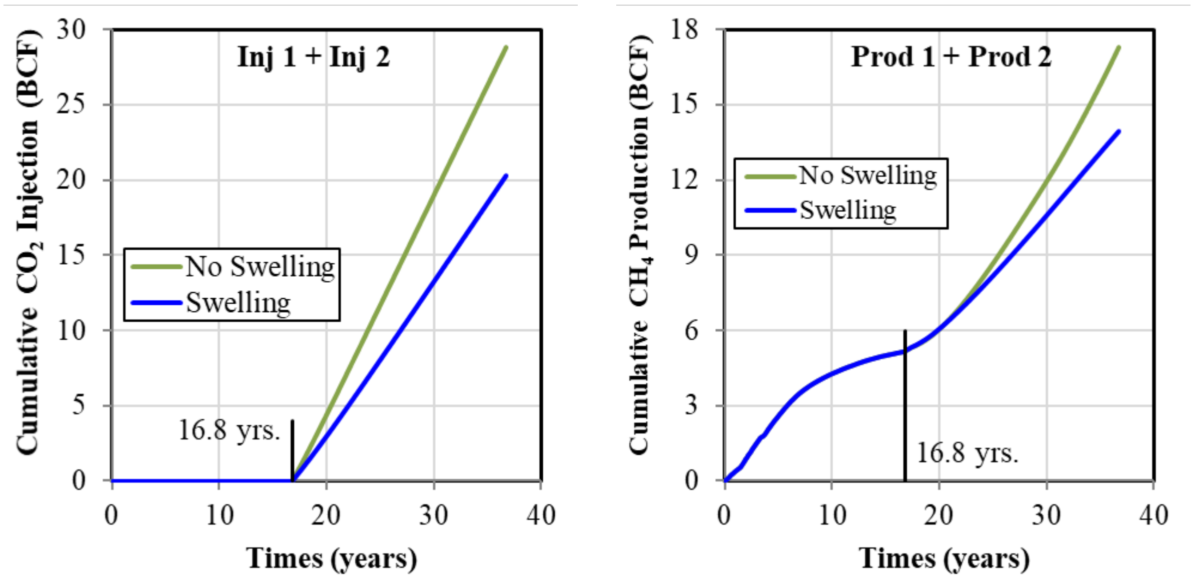

(a) (b)

Figure 20. The effect of swelling on (a) the total volume of CO_2 injected by the two injectors and (b) the total volume of CH_4 produced by the two producers.

Effect of CO_2 Injection on Breakthrough Time

Considering a maximum (per well) injection rate of 2 MMscfd,[29] the injected CO_2 is preferentially adsorbed at the expense of the coalbed methane, which is simultaneously desorbed and recovered from the producing wells. The results indicate an initial slight decline in gas production rate with the commencement of the enhanced recovery process compared to the primary CBM production (Figure 21). This slight initial decline in the methane production rate at the start of CO_2 injection occurs due to relative permeability changes around the production wells. After the commencement of CO_2 injection, residual water is displaced towards the producing wells, resulting in increased water saturation. This increases the relative permeability to water in the vicinity of the producer (with an accompanying reduction in the relative permeability to methane). This caused a slight reduction in the gas production rate. When an adequate amount of water has been produced, the gas relative permeability starts to increase around the production wells, which increases the gas production rate. Earlier CO_2 breakthrough was observed at higher injection rates (Figure 22).

[29] M indicates thousand, MM indicates million

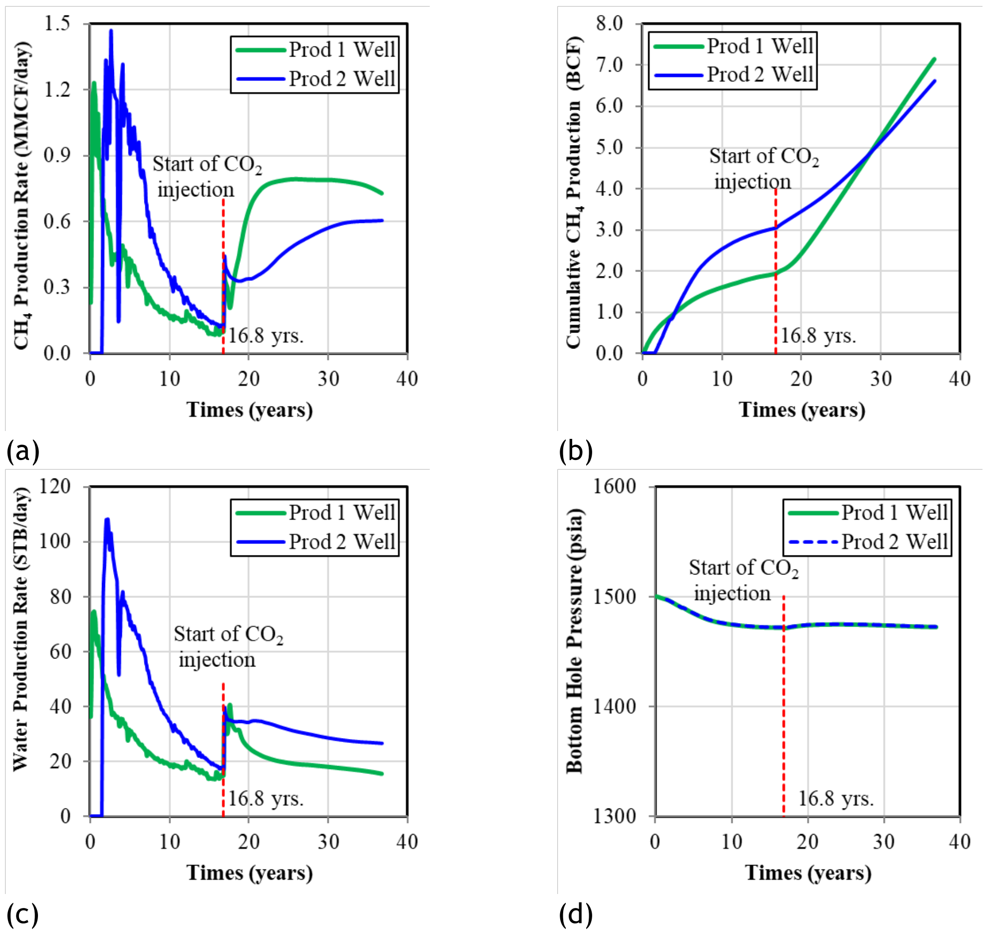

Figure 21. Prod 1 and Prod 2 CO_2-ECBM production profiles (a) CH_4 production rate (b) cumulative CH_4 production (c) water production rate (d) production well pressure.

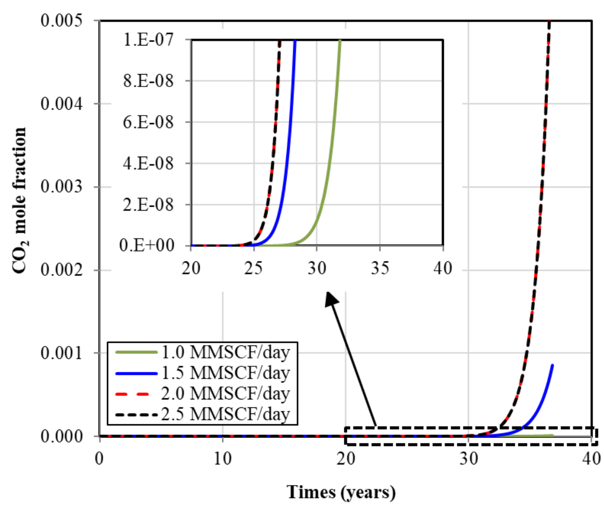

Figure 22. A zoomed-in CO_2 breakthrough profile indicates breakthrough times for the different injection rates.

As expected, the rates at which CO_2 breaks through to the production well(s) are inversely dependent on the injection rate. Table 4 summarizes the simulation results. The tabulation shows the total volume of CO_2 injected, the total volume of CO_2 produced at the methane production wells (these wells would likely be shut-in once significant CO_2 breakthrough occurred and/or the produced CO_2 would be sent back for reinjection), the total volume of methane recovered, the time at which CO_2 breakthrough occurred, and the total volume of CO_2 stored for different injection rates.

Table 4. Summary of the simulation result from the two injectors and producers.

CO_2 injection rates	Total CO_2				Total CH_4	CO_2 Breakthrough
(MMscf/d)	Injected (Bscf)	Produced (MMscf)	Stored (Bscf)	Stored (10^6 tons)	Produced (Bcf)	(years)
1.0	14.36	0.005	14.36	0.82	12.58	4.38
1.5	18.18	0.48	18.18	1.04	13.50	3.23
2.0	20.30	3.61	20.29	1.15	13.95	3.07
2.5	20.30	3.61	20.29	1.15	13.95	3

The reservoir simulation of CO_2 injection into the Ferron coal in the Buzzard Bench field indicates that sequestration could be feasible. The results from various simulation scenarios show that it is possible to inject about 1.16 million tons (20.3 bcf) of CO_2 over a 20-year prediction duration through two vertical injection wells. From this, 1.15 million tons were successfully sequestered and 13.95 bcf of methane were produced simultaneously from two production wells. Figure 23 is a top view of a CH_4 and CO_2 mole fraction map, indicating the spatial spread of CO_2 within the coal unit at the onset and end of injection, and the distance between the injection wells and the production wells.

IX. Implications of the Simulation Results

For this rudimentary two-well injection system, the volume of CO_2 stored represents 0.017 percent of the total greenhouse gas emitted in the U.S. in 2018. It is a fraction of the carbon dioxide emitted from either of the coal-fired plants, However, with more than two injectors and a wider spread over the field, a significant contribution could be made.

- Consider servicing the Huntington plant. As a benchmark consider an annual CO_2 emission of 6,000,000 tons of CO_2. Over twenty years this would imply that about 75 to 100 injectors would be required – a significant investment. Only a pilot program can characterize this for sure. These numbers are conservative because the Langmuir isotherm for the CO_2 was not available from Schlumberger when the simulations were completed. After that, data were generated the storage capacity appears to be double this and the number of injectors could be halved – still a significant operation.

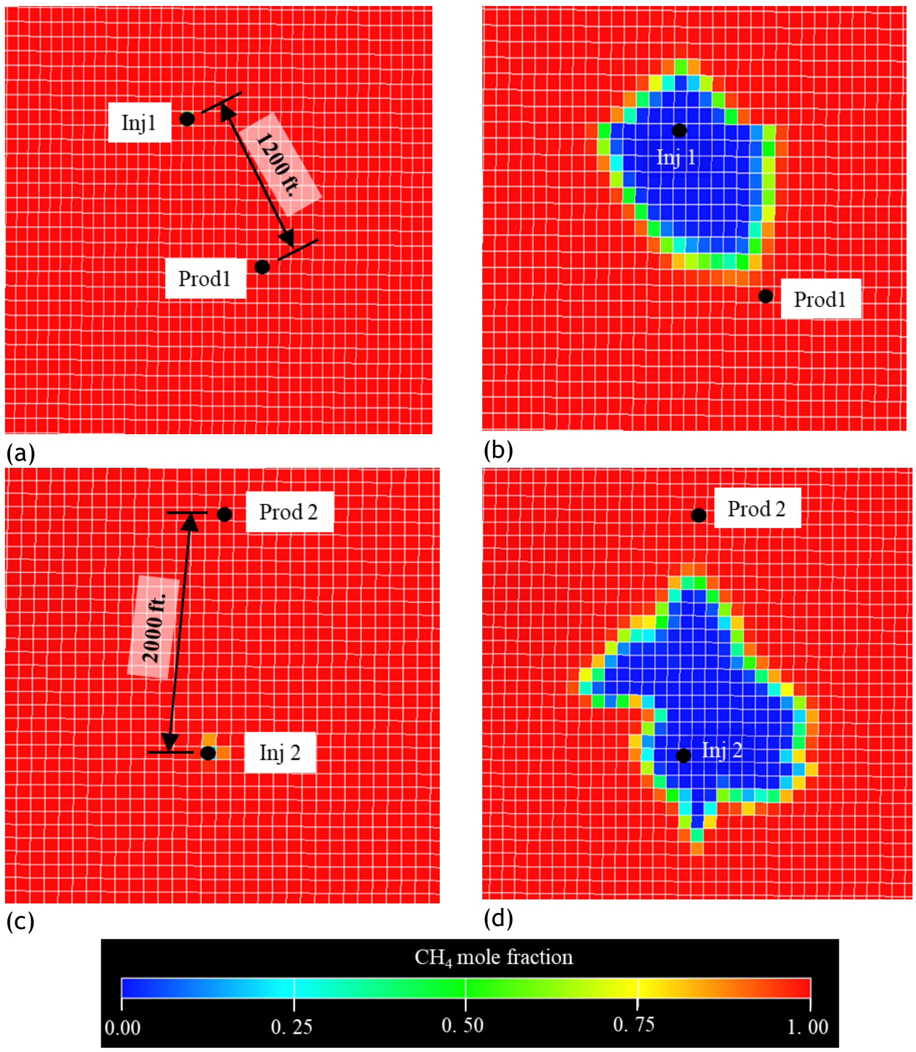

Figure 23. Top view of the mole fraction map (a) at the beginning of injection for Inj 1 and Prod 1, (b) at the end of injection for Inj 1 and Prod 1, (c) at the beginning of injection for Inj 2 and Prod 2, and (d) at the end of injection for Inj 2 and Prod 2.

- A limitation on the rate of injection per well is the reduction in permeability associated with swelling. As the permeability reduces, the injection pressure increases. The limit on the injection pressure has been taken to be minimizing the bottomhole pressure to avoid hydraulic fracturing. Only a pilot/field experimentation will ultimately confirm these pressure limitations.

- **Question: Will this pressure increase be as severe as simulated if the interfingering sands act as a pressure relief and delivery mechanism?** Almost certainly not. Measurements of the permeability of the Ferron sand suggest preferential gas flow would occur into the sands, offering the ability to bypass locally reduced permeability in the coals. With time, adsorption would occur into the interfingered coals with accompanying sequestration. Simulations tend to suggest this as well. A pilot test would establish the value of this revolutionary concept – relying on the sands to deliver the CO_2 and the coals to sequester it (refer to next section).
- **Question: What happens if the pressure causes local fracturing?** This is an unanswered technical question. If the fracturing is restricted to the sands and the coals, the results will be beneficial. Areas of locally reduced permeability will be breached/bypassed and injectate can move beyond the impaired zones. The concern is breaching a seal. The overlying Mancos formation is relatively thick and could tolerate some local fracture penetration. Consequently, the method for fracturing, as part of the storage protocol, needs to be carefully defined and tested at a pilot scale. For example, if high pressures are encountered during injection, a small slug of water might be injected to allow a small fracture to develop, to see if pressure can be relieved. This is unsubstantiated territory and would require testing and validation. Assuming that the carbon dioxide can be maintained in a super critical state, a nominally incompressible slug (the water) may not be needed to generate a small fracture step. This is advocating the possibility of a WAG (water alternating gas) operation. Corrosion would need to be considered.
- **Question: Can flue gas be pumped?** There are some indications that it could be viable to pump flue gas or at least a nitrogen-carbon dioxide mix. Oxygen and non-scavenged H_2S are undesirable from a corrosion perspective, but possibly reduced separation of the flue gas is feasible. Laboratory testing has shown that the degree of swelling is contingent on the amount of nitrogen present with the carbon dioxide and that permeability reduction is similarly impacted. If flue gas is injected, permeability reduction may be reduced. The drawbacks are that the relative concentration of carbon dioxide injected is less and the hydrostatic pressure will be reduced (if miscible or perfectly mixed) and expenditure for compression and pumping will consequently be higher. The separation of the two species will also be a challenge.

Methane production is anticipated. The optimal use of that methane may be for compression of the carbon dioxide (injecting carbon dioxide or flue gas). The EPA has estimated methane leakage rates to be ~1.4 percent by dividing the methane emitted per year by the total amount produced from natural oil and gas wells. That is, 1.4 percent of the natural gas produced could be lost into the atmosphere. Assuming 1.4

percent of the total volume of methane produced is released into the atmosphere, this represents about 313,000 tons of CO_2 equivalent (CO_2e) for the two-well case considered if there are no improvements in the capture of fugitive gas.[30] CO_2e is a metric used to compare greenhouse gas emissions based on their GWP (global warming potential) by converting amounts of other gases to the equivalent volume of CO_2 with the same global warming potential. Comparing this value with the total volume of CO_2 sequestered (1.15 million tons), the environmental impact of this sequestration outweighs the volume of methane that will be released during methane production. With good stewardship and field practices, it is anticipated that in a sequestration operation, this leakage can be significantly reduced.

X. CO2 Movement and Migration into Sandstone Layers

The petrophysical evaluation carried out for the Ferron coal indicates five sand units separating six regionally identifiable coal units. Figure 24 shows this schematically. This is an ideal scenario. While the Mancos formation offers an excellent seal upwards, the Ferron sand "stringers" (with gas storage by compressibility in porosity only – i.e., no adsorption) provide high permeability channels for delivering gas deep into the reservoir EVEN IF COAL PERMEABILITY IS LOCALLY REDUCED BY SWELLING. This ensures long-term injectivity. *The sandstone provides permeability. The coal provides storage*.

Simulations were repeated where a single sand stringer was represented at the top of the coal to establish the volume of CO_2 that would migrate into an adjacent sandstone unit after (or before) CO_2 injection into the coal seams has reached its full storage capacity.

Injection of CO_2 into the coal unit raises the pressure near the well, allowing CO_2 to enter the coal matrix initially occupied by the in-situ formation fluids (methane; if production has ceased some time ago, additional dewatering by displacement may be required). The amount and spatial distribution of pressure buildup and the distribution of CO_2 will depend on the injection rate, the permeability, the thickness of the injection formation, and the presence or absence of permeability barriers within the reservoir.

[30] https://static.berkeleyearth.org/memos/epa-report-reveals-lower-methane-leakage-from-natural-gas.pdf suggests around 1.5%

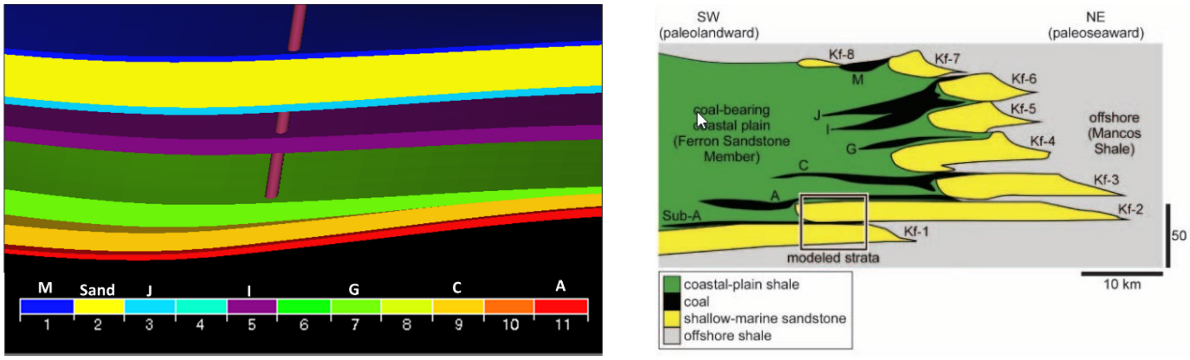

Figure 24. One cross-section of the Ferron coal layers (M-blue, J-light blue, I-pink, G-light green, C-orange, and A-red) indicates six coal layers and the interfingered sandstone layer (yellow). At right: "Schematic regional cross-section through the Last Chance delta system of the Ferron Sandstone Member, its major coal seams (assigned letters sub-A to M), and its eight-component shallow-marine [sic sandstone] tongues (numbered Kf-1 to Kf-8), from the southwest (paleo-landward) to the northeast (paleo-seaward) (after Anderson et al., 2004). … (after Deveugle et al., 2015)."

Once the CO_2 is injected into the composite sandstone and coalbed reservoir, the primary flow and transport mechanisms that control the spread of the CO_2 include:

- Fluid flow in response to pressure gradients created by the injection pressure.
- Buoyancy is due to the density differences between CO_2 and the formation fluid. In many operations, overriding of the CO_2 is a concern – less so here if sand stringers can move gas to more distant parts of the reservoir.
- Diffusion and adsorption of CO_2 into the coal matrix.
- Limited porosity storage in the Ferron sands and more importantly the ability to deliver gas far away from the injectors.
- Dispersion and fingering are caused by formation heterogeneities and mobility contrast between the CO_2 and the connate formation fluid.

As indicated, to model the composite nature of the reservoir, one sandstone unit was incorporated into the model. This required a new history match to validate the model with the historical rates accurately. The history match is shown in Figures 25 and 26 After validating the model via history match using measured methane production, CO_2 injection commenced.

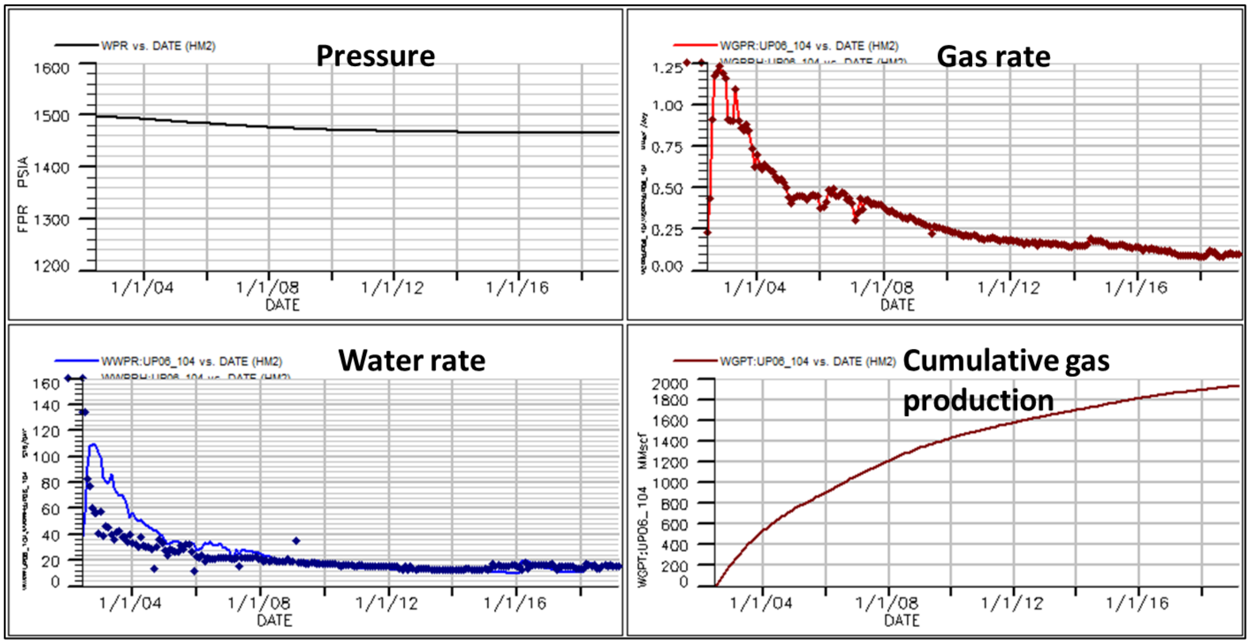

Figure 25. Well Up06_104 performance plot (historical data in dots and simulated data as a solid line). Historical methane production is shown.

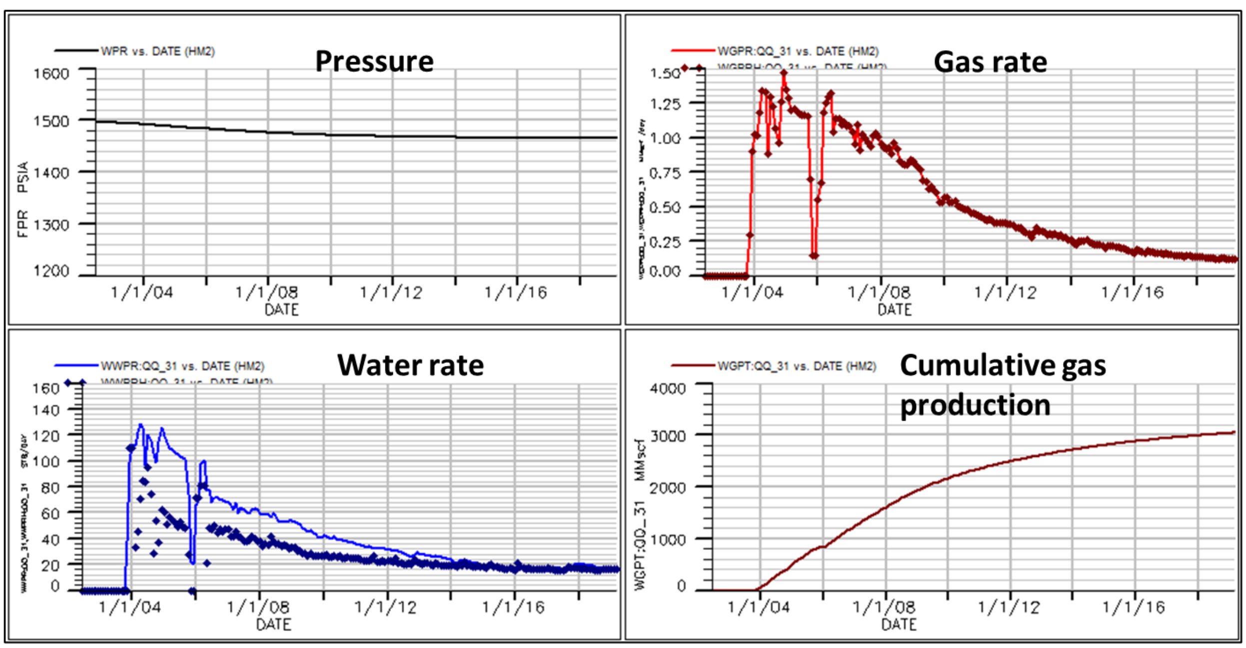

Figure 26. Well QQ_31 performance plot (measured data in dots and simulated as a solid line). Historical methane production is shown. The plots demonstrate the difficulties in matching both gas and water production.

XI. Insights

This evaluation focused on CO_2 sequestration and enhanced coal bed methane (ECBM) production opportunities in the Ferron coal of the Uinta Basin. The model generated includes a dual-porosity system with gas diffusion, adsorption, desorption, multiple-component gas representation, and coal swelling effects. Public domain geophysical and geological data were used to develop three-dimensional geological and reservoir models. The reservoir geometry was developed, and heterogeneity in porosity and permeability was represented using geostatistical techniques. The reservoir model was validated by history matching to available historical production data.

Key observations are as follows.

- Injection and storage of CO_2 into the Ferron coal seam within the Buzzard Bench field is feasible. With only two injection wells, simulation suggests it is possible to inject about 1.15 million tons (20.30 bcf) of CO_2 over 20 years, with CO_2 breakthrough occurring after three years of injection inception (the breakthrough gas would need to be reinjected). This is a lower limit and would increase if the transport and storage in interfingered sands is considered and if higher measured carbon dioxide storage capacity was used.
- The maximum injection rate for each injector was achieved at an injection rate of 2 MMscfd, successfully sequestrating about 1.15 million tons of CO_2 from a two-well injection package. The rate limitation was a pressure ceiling that was applied to avoid hydraulic fracturing. This injection consideration could be alleviated if the role of interfingering sands as a "delivery medium" is considered, recognizing that the elevated pressure is due to swelling.
- The volumes of CO_2 injected, and CH_4 produced were reduced by 29% and 19%, respectively due to coal swelling. This phenomenon is supported by several published research articles (for example, Palmer and Mansoori, 1996; Laxminarayana et al., 2004). The total volume of methane recovered over the same period is 13.95 bcf (from two production wells) This incremental methane recovered may provide a meaningful offset to the CO_2 sequestration, capture if necessary, and transportation costs.
- Carrying out hydraulic fracturing treatments on the injection wells and using a reasonable injection/production well configuration may be an effective way to enhance CO_2 injectivity. Also, direct flue gas injection instead of injecting only pure CO_2 may be carried out to reverse, delay or prevent coal swelling, thus increasing the permeability and injectivity to a reasonable extent. The rationale for this latter hypothesis is provided in the following sections.

XII.Bench Scale Demonstrations:

A comprehensive set of bench-scale evaluations was carried out to support the preliminary numerical modeling that is described above. In addition, fundamental injectivity concerns were addressed. These concerns/attributes included the degree of swelling and permeability restriction, the concept of the interfingered sands serving to deliver gas farther from the injectors despite swelling-induced permeability reduction, and the potential for injection of flue gas rather than higher-quality CO_2.

Different gases were injected into Ferron coal samples. This included argon (as a baseline where no adsorption is expected), nitrogen where limited injection is expected, carbon dioxide where significant chemisorption is expected, and blends of nitrogen and carbon dioxide to mimic injecting flue gas.

The purpose of the experiments is to provide input for carbon dioxide sequestration simulations and to clarify the basic response of these coals and surrounding rocks to indicate if they could be suitable for injection, enhanced methane recovery, and pseudo-permanent sequestration of carbon dioxide.

XII.1 Experimental Characterization of CO2 Storage in Coal

XII.1.1 Sample Description

Recall that the geologic challenge is to evaluate the coalbed methane system in the Buzzard Bench field. As described previously, the Ferron Coal is developed within the Ferron Sandstone in six different units with thicknesses ranging from 0.5 to 3 m across the play. These coal seams dip northwest over the western flank of the San Rafael Swell. The shallowest coal layer was encountered in one well at 2053 ft, and the deepest coal encountered in the area was at 4392 ft. The Blue Gate Member of the Mancos Shale conformably overlies the Ferron Sandstone, acting as the caprock above the coalbed methane reservoir.

For this scenario, the average estimated reservoir pressure is hydrostatic (a pore pressure of 0.43 to 0.45 psi/ft is anticipated). The pore pressure used in the experiments was 1200 psi, according to literature and drilling and production reports – based on actual logging depths. This would be for a well that encounters the coals at a depth of 2760 ft TVD[31].

The experiments described in the following sections were designed to consider fundamental scientific questions (swelling and injectivity to multiple gases) and to do a preliminary qualification of the field as a site for ECBM. The specific samples tested were from the following.

- Mancos (Blue Gate Member) Shale (MBG-Sh)
- Ferron Sandstone (F-SS)
- Ferron Coal (F-Coal)

Samples of each of these lithologies, Figure 27, were retrieved in-situ, from an active coal mine in Emery County, Utah, and its environs. The Mancos shale and the Ferron sandstone were retrieved from outcrops near the mine, whereas the coal was retrieved from tunnels in the mine.

[31] TVD indicates true vertical depth

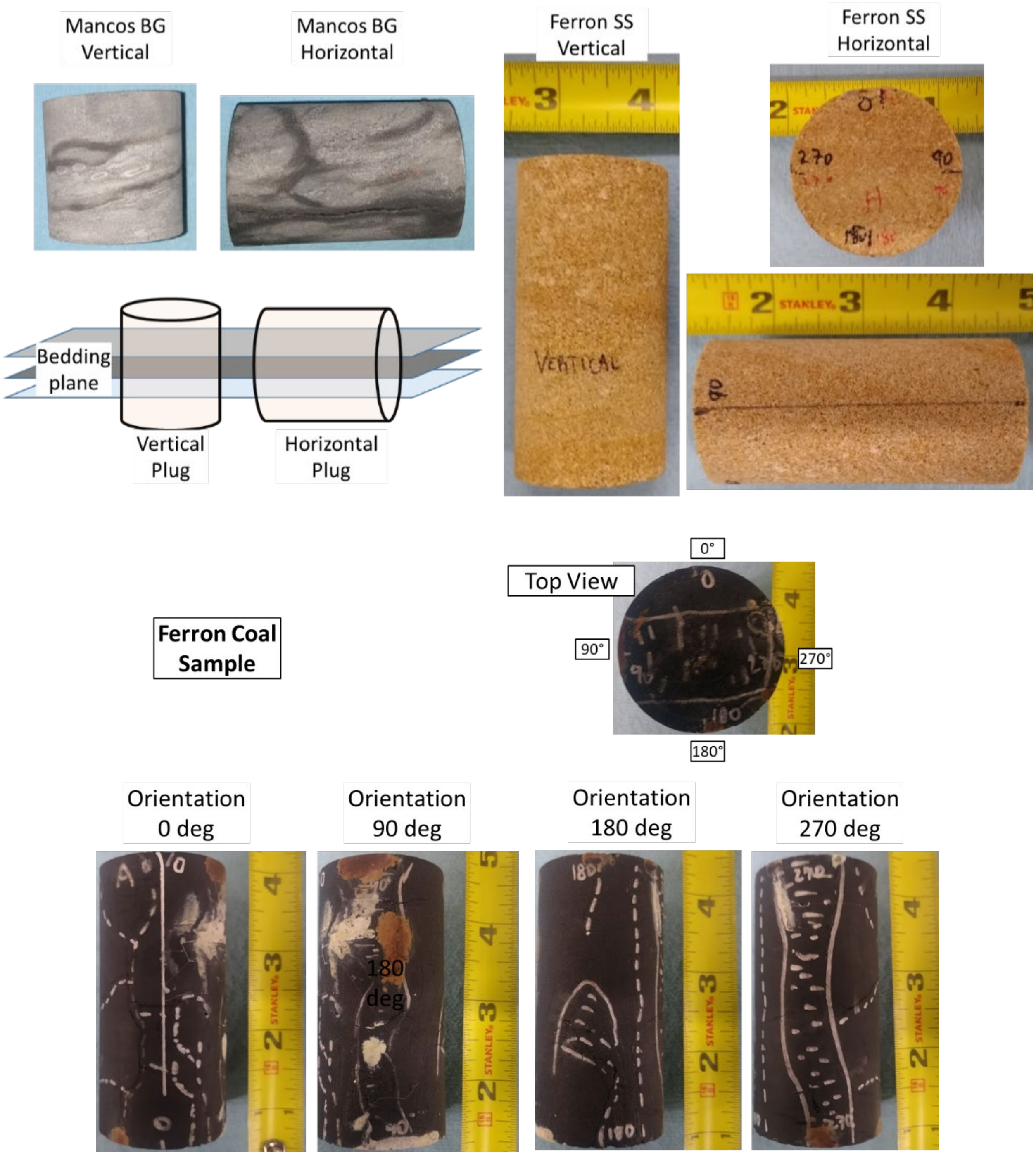

Figure 27 Samples retrieved from outcrops at the periphery of the Buzzard Bench field, near Emery, Utah. At the top left is a view of a core plug from the recovered Mancos shale. The core plug at the top right is from the Ferron sandstone. A coal core plug with fractures and cleats highlighted is shown in the lower panel.

After bulk samples were recovered from the field, the analyses required cutting core plugs (1.5 inches in diameter by a length of 3 inches). The plug from the extremely layered and brittle Mancos shale was only two inches in length. Before each test described in the experiments below, the samples were prepared by heating in an oven to 140°C for 36 hr, followed by a 48 hr period of evacuation in a vacuum desiccator filled with desiccant (silica gel beads).

XII.1.2 Sample Mineralogy

Mineral analyses (x-ray diffraction measurements) were performed. These are listed in Table 5 and displayed in Figure 28. A ternary diagram (Figure 28) is commonly used to describe the minerals constituting specific facies in sedimentary basins. The results indicate:

- The sampled Ferron sandstone is composed of 91.6 wt.% silicate minerals, confirming a shoreline depositional environment. The silicate minerals are subclassified as 75.8% Quartz (SiO_2), 9.7% tectosilicate plagioclase feldspar ($NaAlSi_3O_8$ – $CaAl_2Si_2O_8$), and 6.1% of potassium feldspar ($KAlSi_3O_8$). In addition, there were 7.9% clay minerals: 2.3 and 5.6 wt.% of illite and kaolinite, respectively.
- The composition of the Mancos shale sampled is a mixture of 58.3 wt.% silicates, 30.7 wt.% carbonates, and 11.0 % clays. Detailed subclassification is shown in Table 5. A relevant feature is the high concentration of carbonates. The consequences of this in the presence of carbon dioxide in the coals and the sands will need to be evaluated.
- As for the coal, proximate analysis (Table 2) showed 3% moisture and 8% ash (likely silicates).

Table 5. XRD Mineralogy from samples of the Ferron Sandstone (F-SS) and the Mancos Blue Gate Shale (MBG-Sh).

Sample	Carbonates				Silicates				Clays					Total
	Calcite	Mg Calcite	Dolomite	Total	Quartz	Plagioclase	K-Feldspar	Total	Illite	Kaolinite	Interlayered Illite/Smectite	% Illite in I/S	Total	Total
Ferron Sand	tr			0.0	75.8	9.7	6.1	91.6	2.3	5.6			7.9	99.5
Mancos Shale (Blue Gate)	12.1		18.6	30.7	54.1		4.2	58.3	3.0	8.0			11.0	100.0

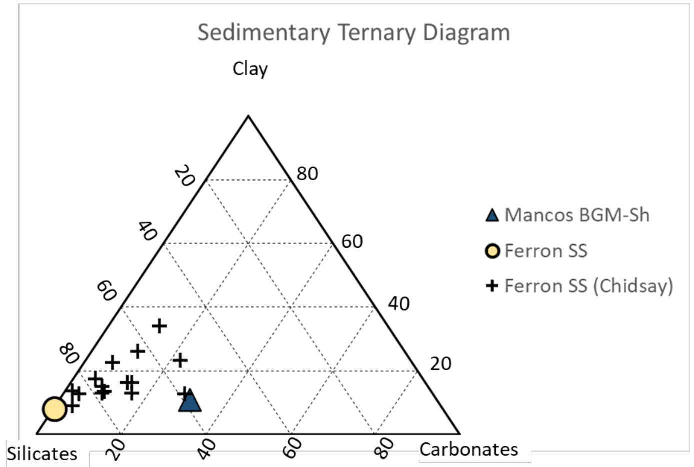

Figure 28. XRD- mineralogy analysis of the Mancos Shale and Ferron Sandstone displayed as a ternary diagram

XII.1.3 Porosity and Density Measurements

The porosities of the samples were measured using a Core Laboratories porosimeter. The samples were unconfined, and helium was used as the reference gas. The diameter and length were measured with calipers to determine the bulk volume of each sample. Each measurement was repeated three times to verify data consistency and averaged. The porosity and density of the samples are shown in Table 6 and displayed in Figure 29.

The porosity of the Ferron sandstone (F-SS) exceeds 20%., which indicates a large compressibility-based storage capacity and presumably high permeability given the weakly consolidated nature and the coarse grains of this formation. The Mancos sample (MBG-Sh) has a porosity of 6.0%, although it is formed by compacted fine grains. The porosity of the Ferron coal was measured, averaging 3.0%, mostly from the cleats and open fractures (recall that these measurements were unconfined, and in situ, this type of primary porosity may be closed because of in situ stresses). The grain density of the MBG-Sh and F-SS are 2.67 and 2.64 g/cm^3, respectively. The density of the MBG-Sh is higher because of the higher calcite and dolomite content.

XII.1.4 CT Scanning

Computerized Tomography Scanning (CT-Scanning) allows three-dimensional mapping of volumes, allowing the visualization of internal structures by identifying contrasts in density. It is also possible to obtain the distribution of larger pores and fracture networks. The basic interpretation of the images relies on higher-density minerals producing brighter (white) zones, and darker areas corresponding to low-density regions, including cracks and voids. Figure 30 is a composite of the CT scans of the relevant samples. The black domains represent voids, identifying the porosity and fracture distribution. (An exception is for images C and F where the contrast is inverted to highlight the void spaces in a 3D model).

Table 6. Porosity and Grain Density

Sample	Dry Weight (gm)	Length (in)	Diameter (in)	Calipered Bulk Volume (cm^3)	Grain Volume (cm^3)	Pore Volume (cm^3)	Grain Density (gm/cm^3)	Porosity (%)
Mancos BG-H[32]	165	2.33	1.48	65.9	62.0	3.9	2.67	0.06
Mancos BG-V	154	2.14	1.49	61.5	57.4	4.1	2.68	0.07
Ferron SS-H	180	3.00	1.49	85.8	68.3	17.5	2.64	0.20
Ferron SS-V	180	2.99	1.49	85.4	68.1	17.3	2.64	0.20
Coal-A	110	3.00	1.49	85.8	83.5	2.3	1.31	0.03
Coal-B	109	2.98	1.49	85.0	81.8	3.2	1.34	0.04

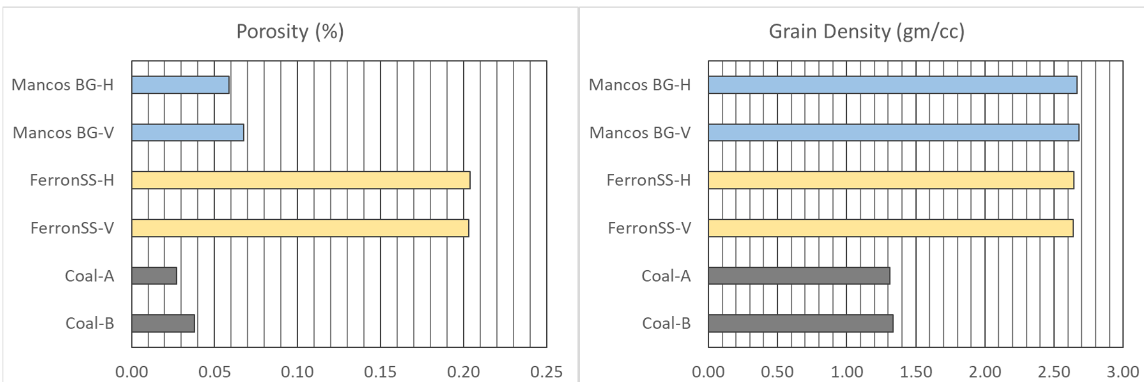

Figure 29. Porosity and grain density of the Mancos shale (MBG-Sh) sample, the Ferron sandstone (F-SS) sample, and the Ferron (F-Coal) coal sample, from unconfined porosity measurements with helium. The appended "H" or "V" indicates a horizontal or vertical plug, respectively.

The Mancos shale sample shown in Figures 30A and 30B shows a consolidated sample with minimal visible porosity, intercalated with a series of fractures parallel to the horizontal bedding. A few vertical fractures interconnect the horizontal laminations.

The porosity in Ferron Sandstone is evenly distributed, as shown by coarse grains of various densities in Figure 30D. A possible variation of the pore size is observed in the three-dimensional image (a composite of individual two-dimensional scans) in Figure 30C, parallel to the bedding plane observed in the core. At the bottom of the image, a concentration of larger pores is observed. This is not unexpected based on the depositional environment.

[32] H indicates a horizontal plug and V indicates a vertical plug.

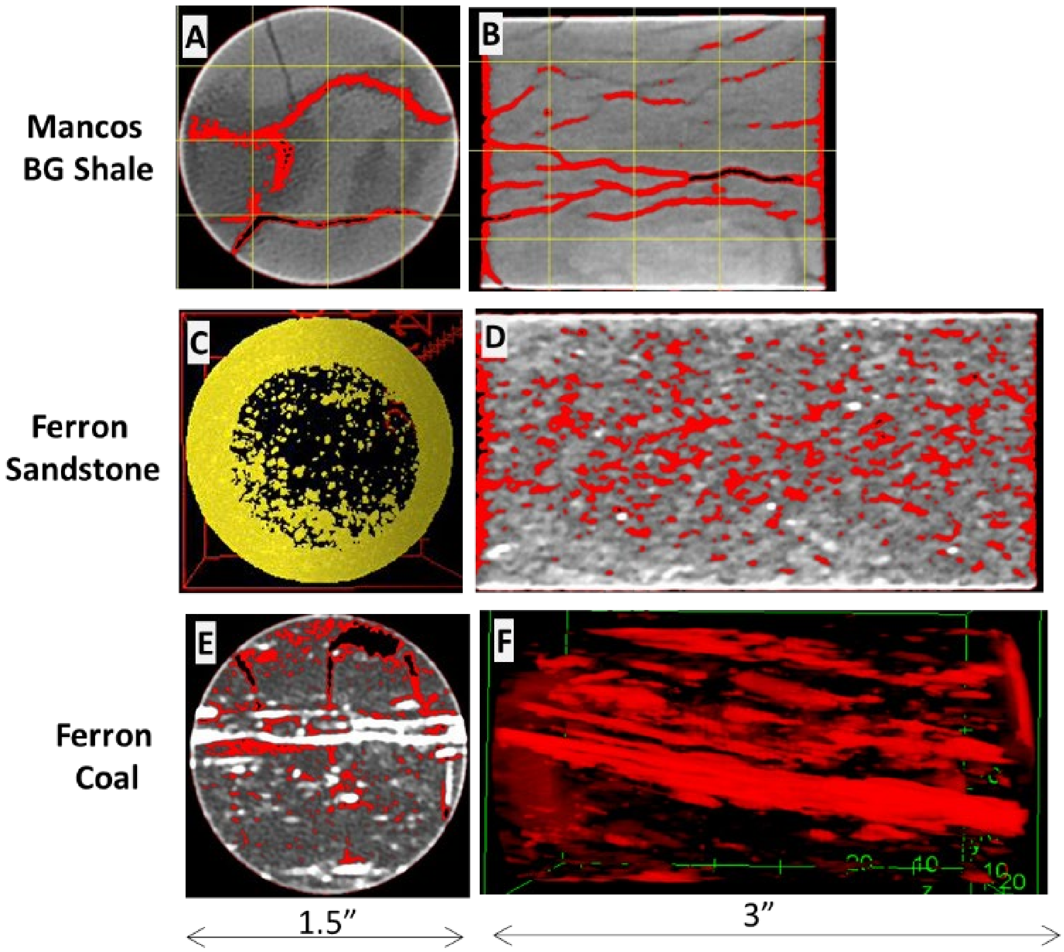

Figure 30. CT-scanned Images of, from top to bottom, Mancos shale, Ferron sandstone, and Ferron coal. The horizontal axis is parallel to bedding.

XII.2 Thermodynamic properties of fluids

The fluids used in the experiments are characteristic of anthropogenic emissions of greenhouse gasses (GHG), following the combustion of fossil fuels in industrial processes. A typical composition of the flue gas in a coal-fired power plant is 0.14 CO_2, 0.10 H_2O, 0.05 O_2, and 0.71 N_2 (Song et al., 2004). The composition of the flue gas after stripping off other byproducts (H_2O, O_2, SO_x, NO_x, and particulate matter) is 0.84 N_2 and 0.16 CO_2. In this research, the simulated flue gas mixture was selected as 80:20 N_2:CO_2. Therefore, the fluids utilized in the experiments are pure and mixed compositions of N_2 and CO_2:

- Pure nitrogen (N_2)
- Flue gas mixture 80:20 N_2:CO_2
- Flue gas mixture 50:50 N_2:CO_2
- Pure carbon dioxide (CO_2)

The experimental procedures and calculations for the flow and adsorption tests (that are described shortly) require the input of fluid properties consistent with the pressure and temperature of the system. The properties of the fluids used - CO_2, N_2, and Ar - are either calculated from equations of state (EOS) or obtained from the public NIST database (NIST, 2021):

- Compressibility (Z) (EOS calculated)
- Density (ρ) (Z-EOS derived)
- Viscosity (μ) (NIST Database)

The configuration of the experimental equipment used to assess storage in the Ferron coal requires considering two temperatures. The fluids will be at room temperature at 24°C during preparation before injection into the rock sample. The in-situ temperature inside an oven containing the coal sample simulates the reservoir conditions, averaging 38°C. The fluid properties are characterized for both temperatures since this is relevant during the experiments and for comprehending the results.

XII.2.1 Compressibility

The compressibility (Z) of non-ideal fluids is described using cubic equations of state (EOS). The mathematical formulation of these EOSs accounts for attractive and repulsive molecular interactions in terms of the critical pressure (P_{CR}), critical temperature (T_{CR}), and the acentric factor (ω) of each substance. A summary of the mathematical description of the equation of state used in this research is provided in Appendix A.

The Peng-Robinson EOS (PR) (Peng & Robinson, 1976) is a commonly used EOS for pressures lower than the critical pressure P_{CR}. Other EOSs evaluated for this project are the Redlich-Kwong (RK) (Redlich & Kwong, 1949), Soave-Redlich-Kwong (SRK) (Soave, 1972) , Schmidt-Wenzel (SW) (Schmidt & Wenzel, 1980), Patel-Teja (PT) (Patel & Teja, 1982) (Figure 31). Recently, researchers have aimed at providing better EOS accuracy at the transition from sub- to supercritical and at pressures higher than P_{CR}. The PT-EOS was selected for the modeling in this study since it replicates the data from the NIST database near the test pressure (P_T) used in the experiments, P_T = 1200 psi (8.27 MPa).

The computational overhead for calculating the compressibility for each EOS is relatively low. However, long experiments and large compilations of experimental data - as in the experiments in this project - may result in repetitive calculations. Therefore the resulting compressibility isotherm curve is fitted by polynomial regression as a function of the pressure $Z_{Y,T}(P)=\Sigma a_{Zi}P^n$, where P is the system pressure in MPa, a_i are the polynomial coefficients, n is the polynomial exponent, Y indicates the particular pure substance, and T is the temperature of the isotherm. Thus, the pressure recorded by the experimental setup is the primary basis for estimating compressibility.

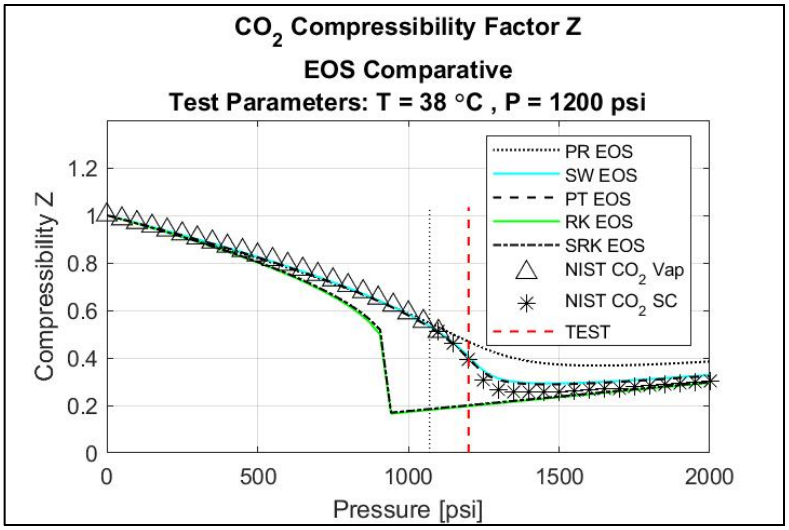

Figure 31 Comparison of various EOSs for calculating CO_2 compressibility as a function of the pressure and its accuracy versus the NIST Database.

The other fluids used in the experiments, Ar and N_2, were modeled using the same PT-EOS and matched well with the NIST database, maintaining properties similar to an ideal gas with Z~1.

The polynomial coefficients for the compressibility are given in Table 7. Refer also to Figure 32 for the compressibility predictions at the temperatures and pressures experienced in the laboratory testing.

Table 7 Compressibility polynomial regression coefficients

	Compressibility Z @ 38 °C						
	Coefficient	**a_{Z5}**	**a_{Z4}**	**a_{Z3}**	**a_{Z2}**	**a_{Z1}**	**a_{Z0}**
CO_2	Subcritical	-1.34E-05	0.000179	-0.00101	0.001031	-0.04843	1.000221
	Supercritical	8.41E-05	-0.00418	0.077585	-0.63718	1.982714	6.21E-07
N_2			6.57E-16	-3.45E-12	1.62E-08	-1.09E-05	1.000863
A			7.62E-16	-3.20E-12	1.30E-08	-3.92E-05	1.000893

The differences between the (compressibility) Z-isotherms for 24 °C and 38 °C, and the fluids used in the research are displayed in Figure 33. N_2 and Ar maintain properties like those of an ideal gas (Z~1) without significant changes between the two temperatures, transitioning from vapor to supercritical at $P_{CR\text{-}N2}$= 492.52 psi and $P_{CR\text{-}Ar}$ = 705.32 psi, respectively. Figure 32 shows a compressibility isotherm for N_2.

The properties of the CO_2 change drastically at around P_{CR} and T_{CR}, which directly impacts this study. Specifically:

- For the room temperature isotherm, the CO_2 transitions from vapor to liquid at a bubble point pressure of P_{BP} = 911 psi (6.29 MPa), yielding a discontinuity in the compressibility curve that is related to the vapor-liquid equilibrium relationships from fundamental thermodynamics. The CO_2 remains in the liquid phase when pressurizing to the testing pressure of 1200 psi (Figure 33).

- The 38 °C compressibility isotherm is continuous (Figure 32, top panel), with the phase vapor-supercritical phase transition at the critical pressure P_{CR}= 1070 psi and temperature T_{CR} = 30.9 °C (304 °K). At the test pressure, P_T = 1200 psi, the CO_2 is in the supercritical phase.

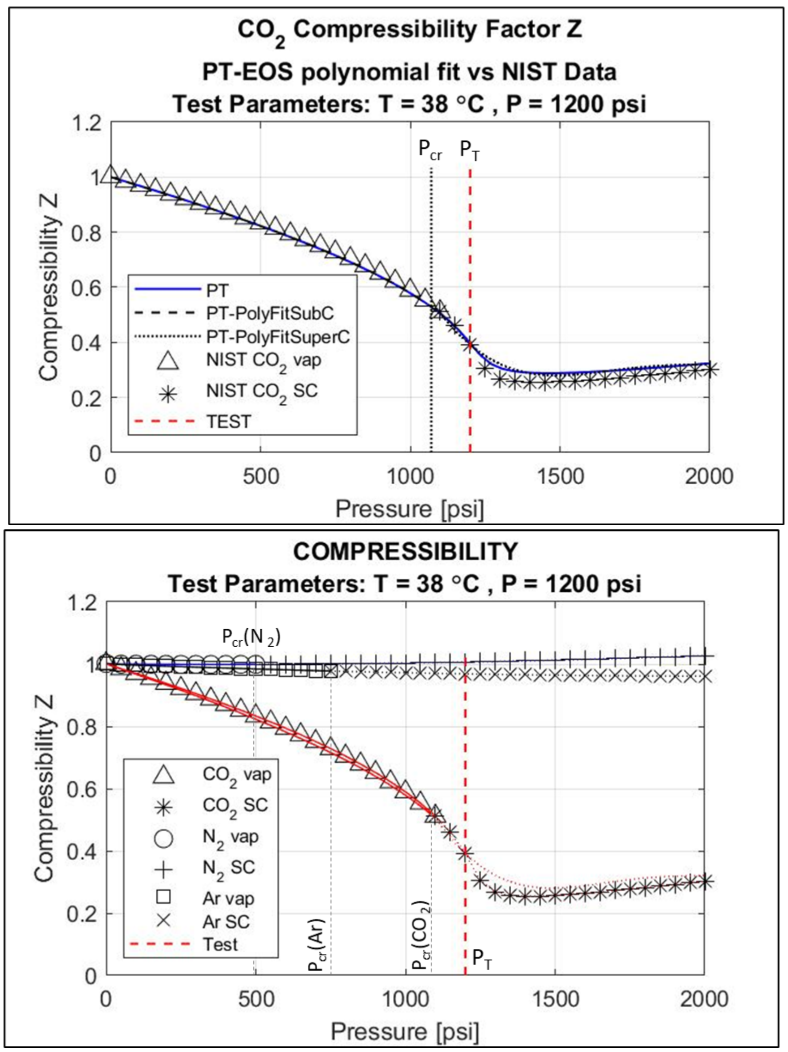

Figure 32 The compressibility curve Z(P) evaluated from the polynomial regression of the PT-EOS. The sub and supercritical segments match the NIST database. These are at 38°C and 1200 psi.

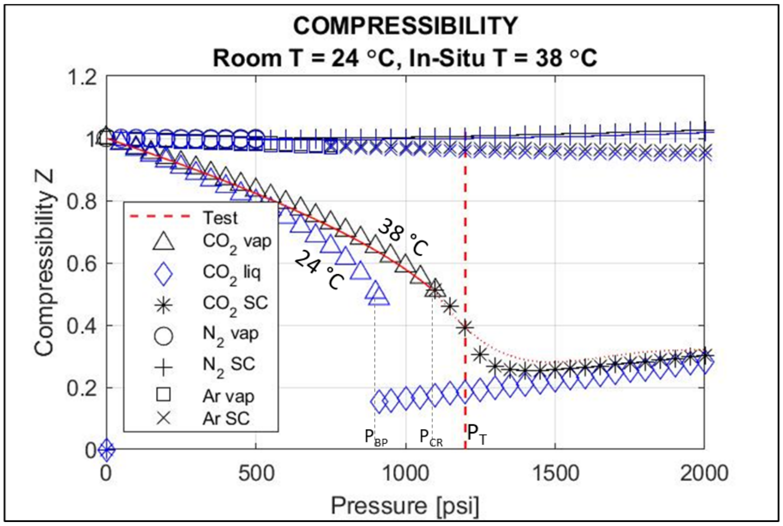

Figure 33. CO_2 compressibility plots for the room (24°C) and in-situ (38°C) temperatures.

XII.2.2 Density

The density of the fluids at experimental conditions is derived from PV=ZnRT, using the compressibility Z from the PT-EOS at the required temperature and pressure. The molar density is calculated from ρ_m = n/V = PRT/Z [mol/m^3]. Mass density is obtained by multiplying the molar density by the molar weight (M) of each molecule $\rho = \rho_m \cdot M$ [kg/m^3], with M_{CO2} = 44.0095 g/mol, M_{N2} = 28.0134 g/mol, and M_{Ar} = 39.948 g/mol.

The resulting density isotherms for 24°C and 38°C are shown in Figure 34. The CO_2 at 24°C is in the vapor phase for pressures lower than the bubble point, having a density of less than 231 kg/m^3. At the bubble point pressure, P_{BP}, the transition to the liquid phase occurs starting with ρ_{CO2} = 725 kg/m^3 and gradually increasing. The density at the test pressure (1200 psig) is ρ_{CO2} = 794.3 kg/m^3. For the case of the 38°C density isotherm, the CO_2 is a continuous curve with a transition from vapor to supercritical at P_{CR}, where the density increases sharply and plateaus at 790 kg/m^3.

The densities of N_2 and Ar increase linearly with the pressure, changing phase from vapor to supercritical at their respective critical pressures, P_{CR}. No significant differences were observed between 24 and 38°C density isotherms.

The most relevant observation of this analysis is the difference in density and phase at temperatures lower than the $T_{CR\text{-}CO2}$ = 30.9 °C. The fluids and surrogate flue gas mixtures used in this research are prepared in the laboratory at room temperature; then, the fluids are pressurized to the test pressure P_T = 1200 psi before injection into the sample. Under these conditions in the pump (before entering the sample), the CO_2 is in a liquid state with a density of $\rho_{CO2\text{-}Liq}$ = 794 kg/m^3, whereas the N_2 is at supercritical conditions with a density $\rho_{N2\text{-}SC}$ = 93.9 kg/m^3. The considerable difference in density and fluid phase leads to a stratification process dominated by buoyancy forces. The details of the thermodynamic path and mechanisms for buoyancy are described in later sections.

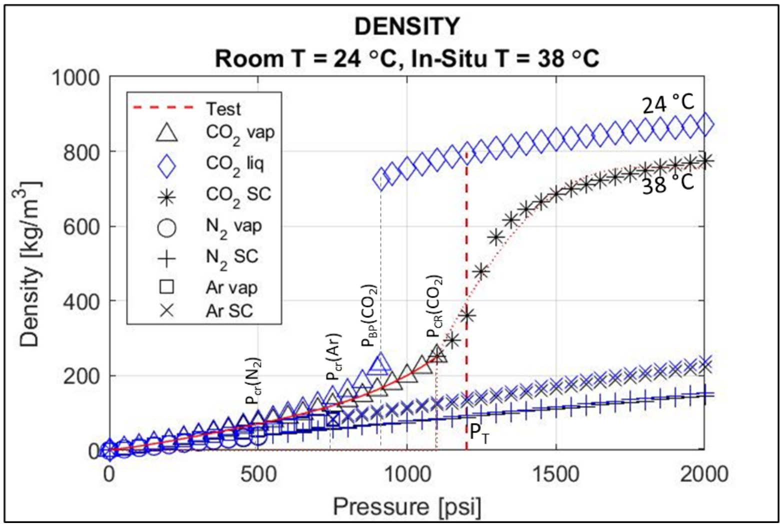

Figure 34. Density isotherms for the test fluids: Ar, N_2, and CO_2, at room and in-situ conditions

XII.2.3 Viscosity

The viscosity of the fluids is a primary input for permeability calculations during flow tests. The viscosity data in this experiment were obtained from the NIST database for room and in-situ temperatures. The viscosity isotherms are also defined functions of the pressure in Figure 35. Table 8 provides the coefficients of polynomial regression for the 38˚C isotherm, $\mu_{Y,T}(P)=\Sigma a_{\mu i}.P^n$ with the viscosity and pressure in SI units (Pa·s and MPa).

Table 8 Viscosity polynomial regression coefficients

VISCOSITY @ 38 ˚C						
	Coefficient	**$a_\mu 4$**	**$a_\mu 3$**	**$a_\mu 2$**	**$a_\mu 1$**	**$a_\mu 0$**
CO_2	Subcritical	5.21E-03	-0.05399	0.227565	-0.17549	15.60317
	Supercritical	0.024435	-0.94629	11.97211	-44.4312	-0.0003
N_2		-0.00341	1.30E-01	-1.74E+00	9.82E+00	2.57E-02
Ar		-0.00269	1.10E-01	-1.63E+00	1.05E+01	1.98E-03

At room conditions, the CO_2 increases its viscosity when the phase change from vapor to liquid occurs at the bubble point. At in-situ conditions (after being injected into a sample at temperature T= 38˚C and a pressure of 1200 psi), all the fluids - CO_2, N_2, and Ar - have a similar viscosity of approximately 0.02 cP [20 µPa·s] (Figure 35). In terms of the flow tests, a fluid mixture of these components will offer nominally the same resistance to flow in a porous medium, with the viscosity ranging from 0.02 to 0.025 cP when the temperature increases from 24 to 38 ˚C.

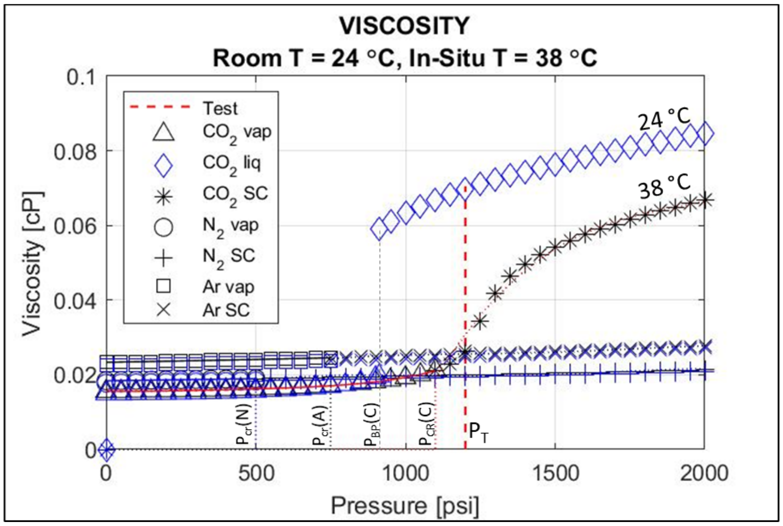

Figure 35. Viscosity isotherms of the test fluids: Ar, N_2, and CO_2, at in-situ and room conditions

XII.2.4 The thermodynamic path of CO_2 during experiments

As discussed previously, Ar and N_2 maintain properties similar to an ideal gas at ambient and in-situ conditions. The CO_2, on the other hand, undergoes drastic changes in phase and compressibility with the temperature change. Figure 36 illustrates the stages, denoted as S1 through S5, during the flow experiments. Figure 37 shows the thermodynamic path of the CO_2 fluid properties.

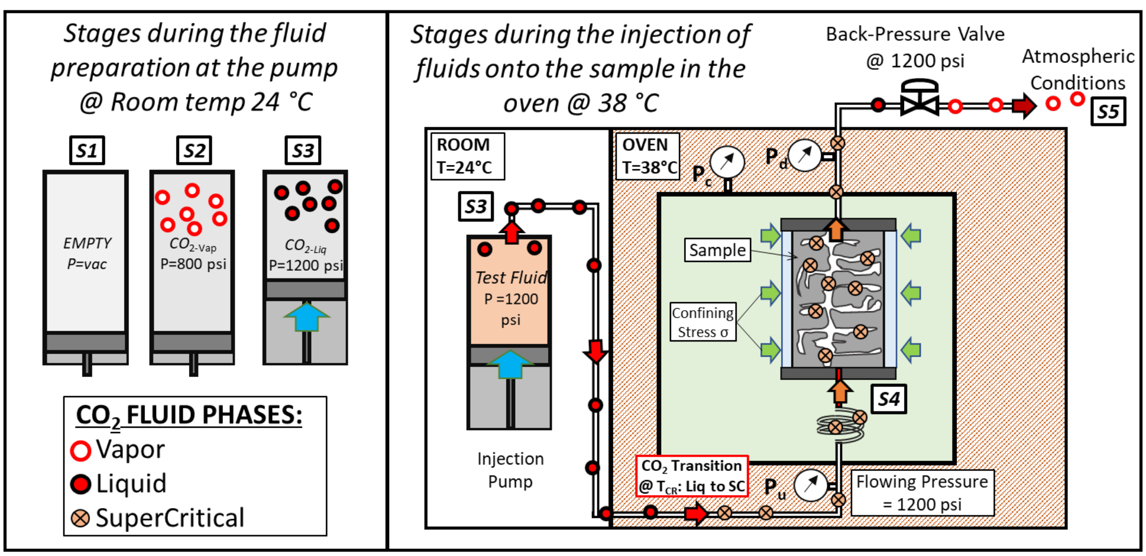

Figure 36. Schematic representations of the CO_2 stages during the experiments: S1 to S3 relate to preparation at room conditions, and S3 to S5 are experienced during injection into the sample in the oven and final venting to the atmosphere, after gas moves through the sample.

During the preparation of fluids at room conditions, CO_2 is transferred from a gas cylinder to the empty pump, filling the pump chamber with fluid starting from a vacuum (S1) and reaching cylinder pressure (S2). Then, the pump chamber is pressurized to test conditions P_T=1200 psi (8.27 MPa) (S3) by actuating the piston upwards and reducing the volume in the pump chamber.[33] A phase change occurs from vapor to liquid at P_{BP}, giving Z_{CO2} = 0.18 and $\rho_{CO2\text{-}Liq}$ = 794.3 kg/m^3. At this stage, S3, for the surrogate flue gas mixtures, the difference in density of the CO_2 compared to the N_2 ($\rho_{N2\text{-}SC}$ = 93.9 kg/m^3) is large and this leads to significant buoyancy effects and fluid stratification.

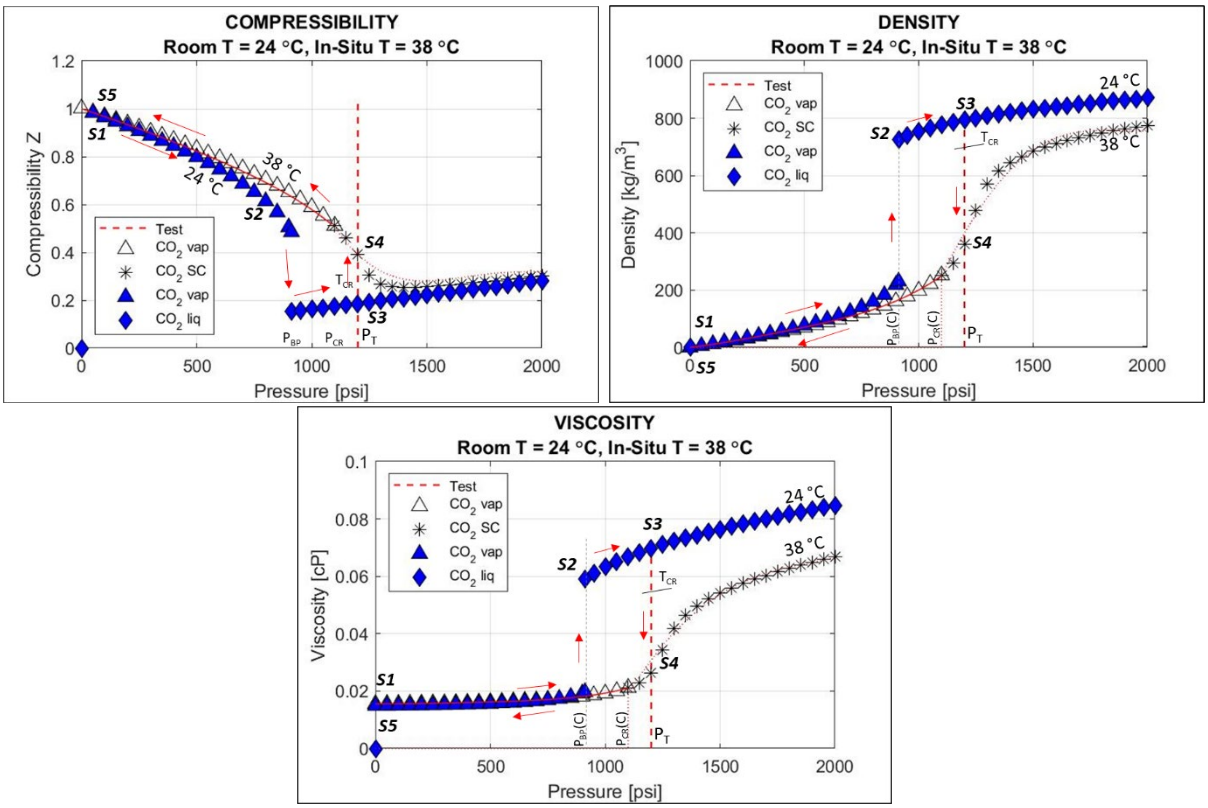

Figure 37. Thermodynamic path of the CO_2 during the experiments.

With injection from the pump (S3)[34] into the sample inside the oven (S4), the CO_2 is heated to 38°C as it flows through the flowlines. This temperature increase causes a phase change from liquid to supercritical at T_{CR} = 30.9°C, and expansion to be consistent with Z_{CO2} = 0.4. The fluid properties entering the sample and interacting with the rock matrix are those at S4 in Figure 37. After flowing through the sample, the CO_2 is decompressed at a back-pressure valve, from 1200 psi to atmospheric pressure (S5). The sudden expansion causes a drop in temperature that may freeze the flowlines and

[33] The valve between the pump and the sample is closed.
[34] The valve between the pump and the sample is opened.

auxiliary equipment. To avoid freezing, the overall flow rate is maintained at a low value of Q=2 ml/min.[35]

XII.2.5 CO_2-N_2 stratification

The CO_2-N_2 gas mixture experiences fluid stratification due to natural convection arising from the density difference between the components (as opposed to forced convection that requires external driving forces such as pressure differential). Hendry et al. (2013) measured the molar composition of a 50:50 CO_2-N_2 mixture in a vertical cylinder at different heights. They observed that the fluids do not segregate entirely into two separate phases but instead develop into a mixed profile; at the bottom of the vessel, the concentration of $CO_{2\text{-}Liq}$ is X_{CO2} = 0.88 wt.% as the denser fluid occupies the lower space while displacing the lighter fluid -$N_{2\text{-}SC}$- upwards. The molar concentration of CO_2 decreases gradually along the vertical axis to a minimum $X_{CO2\text{-}L}$ = 0.27 wt.% at the top of the vessel. This density profile is expressed as a function of the dimensionless distance z'=z/L, where z is the vertical position and L is the vertical length of the cylindrical container. Hendry et al. also determined that the time for fluid segregation was less than 60 seconds – i.e., rapid. The stratification profile of an 80:20 mixture in Figure 38 was extrapolated based on Hendry et al.'s experimental results and represented by a polynomial regression with the coefficients shown in Table 9. $X_{CO2}(z')=\Sigma a_{Xi} \cdot z'^{n}$, where X_{CO2} is the CO_2 composition, and z' is the relative position z/L within the syringe pump chamber. The N_2 composition is $Y_{N2} = 1 - X_{CO2}$.

Table 9. Composition profile for stratified X_{CO2}: Polynomial regression coefficients

	COEFFICIENT	A_X2	A_X1	A_X0
Mix (50:50)		0.5735	0.0821	0.2164
Flue (80:20)		0.3211	0.3161	0.2535

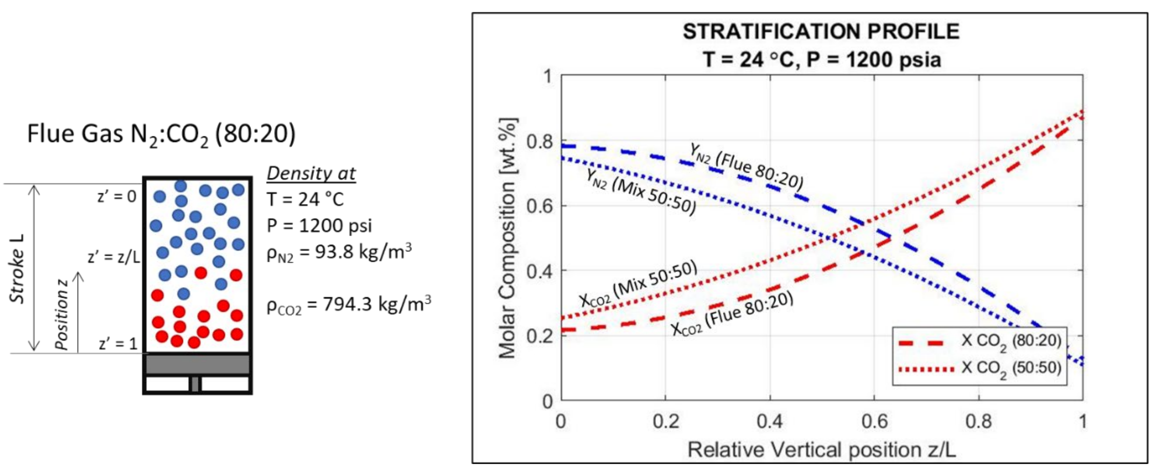

Figure 38. The molar composition of the stratified N_2-CO_2 mixture, based on measurements by Hendry et al. (2018).

[35] This rate may be slightly higher in other experiments described subsequently.

The stratification of fluids is characterized by two independent phenomena: The combined effect of viscous to buoyant forces equilibrium and the fugacity-determined vapor-liquid equilibrium. Both equilibrium criteria produce a density profile that distributes non-uniformly along the vertical axis of the vessel containing the fluids (in our case, the barrel of the pump used to push fluids through the sample).

The thermodynamic principle that causes the density stratification is the vapor-liquid equilibrium (VLE) between the mixture phases. Given the density differences, the CO_2-N_2 binary mixture at temperatures below T_{CR} forms an immiscible solution of a denser phase ($CO_{2\text{-}Liq}$) and a lighter phase ($N_{2\text{-}SC}$). The criterion for vapor-liquid equilibrium is given by the fugacity of the components, which must be equal ($f_1^L = f_2^V$) when the system is energetically stable.

The Grashof (Gr) number is the ratio between viscous and buoyant forces (Bird et al., 2006). Gr indicates the threshold for laminar flow, which in the context of natural convection indicates the condition at which viscous forces restrict the fluid movement. Huang and Li (2018) analyzed the turbulence threshold proposed by several authors with Gr ranging from 10^7 to 10^{12}. Hendry et al. suggested that turbulent flow occurs for Gr between 10^7 to 10^9. The discrepancy between the various authors arose from the experimental setup and the type of fluids used by each party.

Gr is calculated with equation (9), where g is the gravitational acceleration (m/s^2), L_c is the characteristic length (for vertical pipes, this is the length of the containing vessel – the pump chamber in this situation) (m), ρ is the density calculated from the PT-EOS (kg/m^3), Δρ is the difference in the density of the pure species comprising the mixture, and μ is the dynamic viscosity (Pa·s). Figure 39 shows the calculation of Gr for the conditions of the experiment, evaluating the surrogate flue gas composition for room and simulated reservoir (oven) temperature of 24 and 38°C. The estimated length of the stroke of the syringe pump is L = 0.10 m; the pressure-dependent values for density and viscosity using the molar composition of each species as the weighting factor are $\rho_{X:Y} = X_{CO2}.\ \rho_{CO2} + Y_{N2}.\ \rho_{N2}$, and $\mu_{X:Y} = X_{CO2}.\ \mu_{CO2} + Y_{N2}.\ \mu_{N2}$.

$$\mathrm{Gr} = \frac{\mathrm{g} \mathrm{L}_\mathrm{c}^2 \rho \Delta\rho}{\mu^2} \tag{9}$$

Following the notation used for the thermodynamic path in Figure 39, at room temperature Gr increases with the pressure of the pump chamber (from S_1 to S_2) and becomes relevant at 500 psi; turbulent conditions exist, although minimal, thus some stratification is expected. At the bubble pressure, P_{BP}, there is a drastic increase in Gr from $2x10^8$ to 10^9 since the phase of the CO2 change from vapor to liquid, the natural convection becomes turbulent; the buoyancy forces overcome the viscous forces causing the denser component to drop to the bottom of the vessel, and the stratification of the mixture components is imminent at the test pressure in S_3. The increase in temperature when the fluid mixture enters the oven causes a drop in Gr since the density of the CO_2 reduces when transitioning to the supercritical phase.

The flooding of the sample at S_4 occurs under Gr of ~4 x10^8, which is still under turbulent conditions, leading to a partially stratified fluid that might become relevant for fluid transport over long distances. Further study is recommended to evaluate this phenomenon with upscaling to reservoir dimensions.

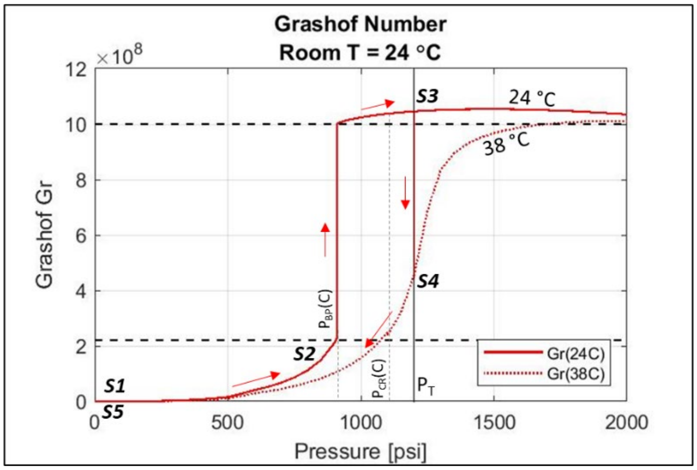

Figure 39. Estimated Grashof number at the different stages of the experiment.

XII.2.6 Stratification Evaluation with a Densitometer

The stratification of the fluids was verified in the laboratory by using a densitometer, comparing the density gradient developed in a surrogate flue gas mixture, to the response of pure flow of N_2 and CO_2, as described in Figure 40 Considering the constituent concentrations of the fluid pumped out towards the sample, the first fluid exiting the pump is the lighter mixture in the upper section of the cylinder, with the exact molar composition at z = L. As the pump piston continues to move at a constant speed (the fluid velocity is determined by the constant flow rate settings of the pump controller), the concentration of the mixture pumped out to the flowlines varies according to the density gradient and the piston position z/L. When the piston reaches the end of the stroke, z' nearly 1, a denser fluid of higher CO_2 concentration is being pumped towards the sample.

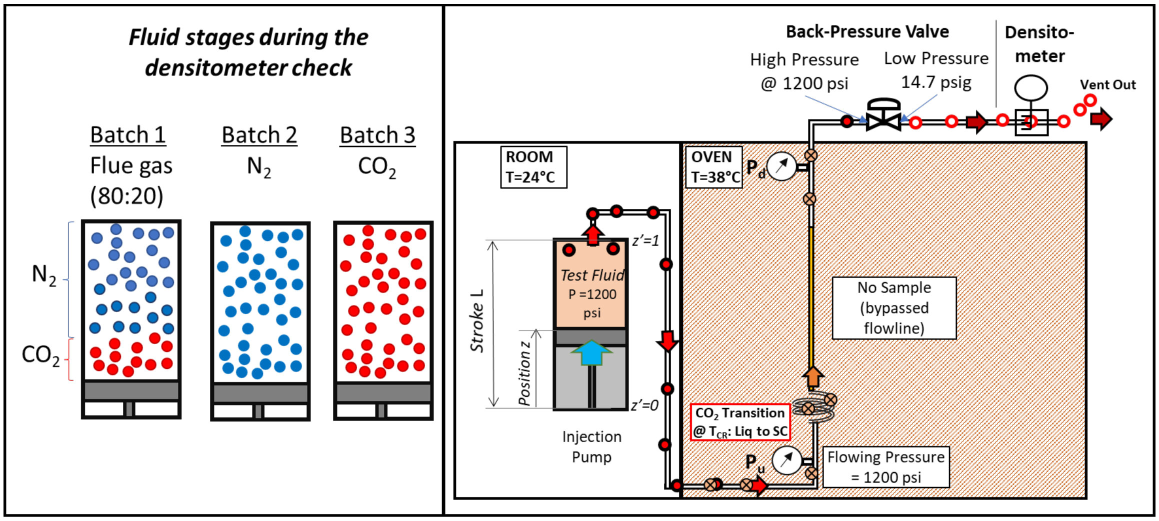

Figure 40. Schematic representations of the fluid batches and the location of the densitometer.

The results of this stratification evaluation are plotted in Figure 41. Starting at 1.3 $kg/m^{3,}$ the surrogate flue gas density follows an increasing density trend as the concentration of CO_2 becomes more prominent while the piston in the syringe pump moves upward from z/L = 0 to z/L=1, where the density reaches 1.48 kg/m^3 After 40 minutes of flow, the flowlines were evacuated, and N_2 was pumped at the same flow rate. Initially, the density read 1.4 kg/m^3, which can be attributed to the remnant simulated flue gas in the flowline. Once the surrogate fluid is displaced out of the flow line, the density decreased to 1.09 kg/m^3, which is the nominal density of N_2 at atmospheric conditions. The third batch of pure CO_2 was then injected after the N_2, with the density increasing to 1.7 kg/m^3. This is the nominal density of CO_2 at STP[36]. This experiment confirms that the fluids entering the rock during permeability tests follow the same pattern -and molar composition- as the stratification profile inside the pump cylinder. This measurement also validates the assumption of using the molar composition as a weighting factor for fluid properties of gas mixtures. The weighted average will be applied to compressibility, density, and viscosity.

The partial pressure of the fluid reaching the sample at any given time is defined from $P_{p-X}= X_i \cdot P_f$, where P_{p-x} is the partial pressure of the denser component, X_i is the concentration of CO_2 at a given time, i, and P_f is the flowing pressure through the sample.

[36] STP is standard temperature and pressure.

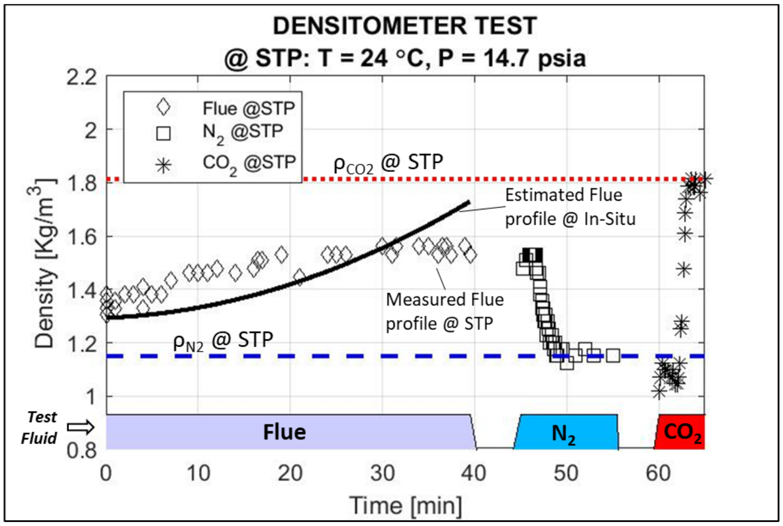

Figure 41. Densitometer measurements (at STP, after the fluid has exited the sample and the oven) and the estimated composition profile at in-situ conditions.

XII.2.7 Weighted Properties of the Fluids

The simulated flue gas was a mixture of nitrogen and carbon dioxide. The mixture's density, viscosity, and compressibility are approximated at local spatial positions in the pump barrel, based on the composition of each species, y_{N2}, and y_{CO2}.

$$\rho_{mix} = y_{N2}.\rho_{N2} + y_{CO2}.\rho_{CO2} \quad (10)$$

$$\mu_{mix} = y_{N2}.\mu_{N2} + y_{CO2}.\mu_{CO2} \quad (11)$$

$$Z_{mix} = y_{N2}.Z_{N2} + y_{CO2}.Z_{CO2} \quad (12)$$

In the foregoing equations, density, ρ_i, viscosity, μ_i, and compressibility, Z_i, are the pure component properties at the respective temperature. Figure 42 displays the calculated mixture properties based on the weighted composition experienced by the simulated flue gas.

XII.2.8 Implications of the fluid stratification

The implications of the fluid stratification in the experiments are:

1) at any given time, the concentration of the constituents in the mixture leaving the pump - and flowing through the sample - varies because of the stratification,
2) it is possible to formulate a measurable criterion for averaged mixture properties such as viscosity, compressibility, and density using the molar concentrations as weighting factors,
3) the partial pressure in the flowline resulting from the molar composition can be determined and is variable, and,

4) there is a predictable variation in the vertical concentration gradient as a function of the Grashof number (which is in turn dependent on the temperature and pressure conditions).

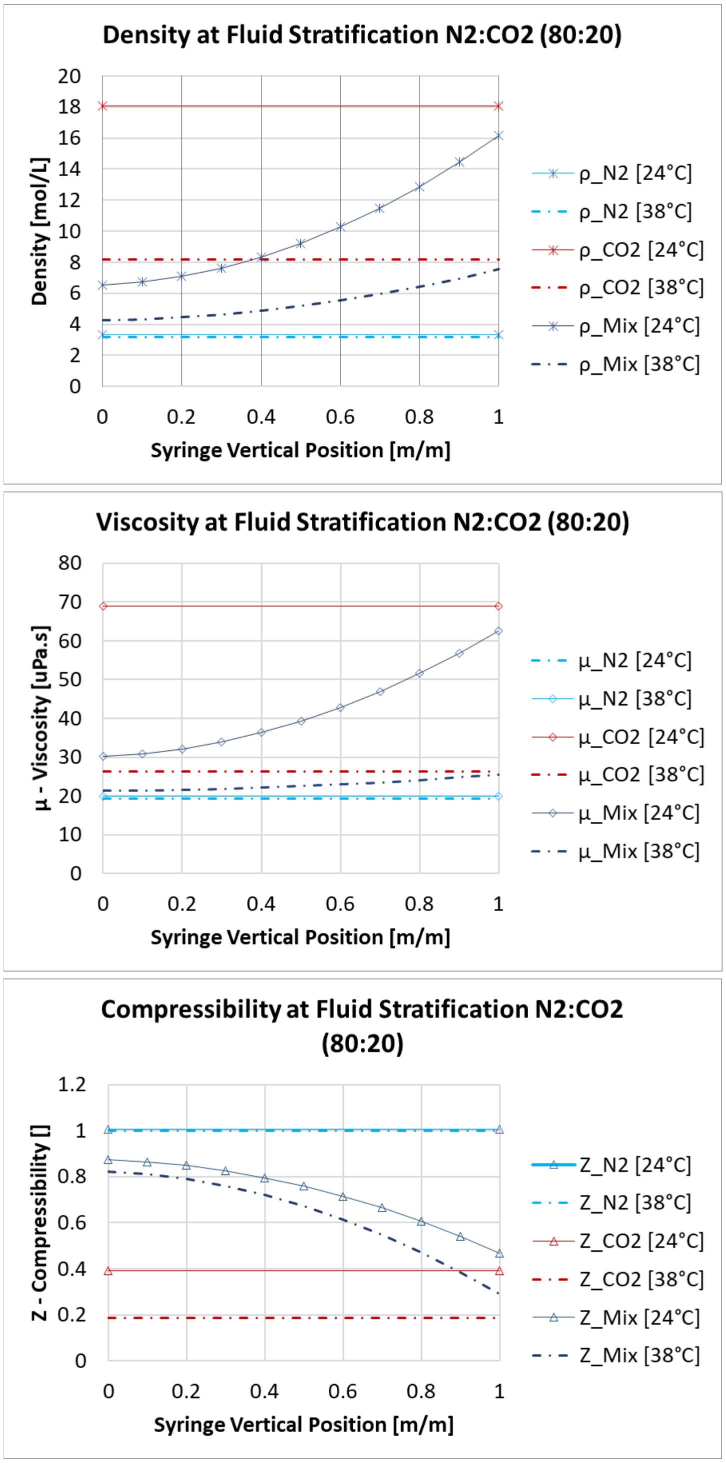

Figure 42. Fluid properties for mixtures after stratification, considering nitrogen and supercritical carbon dioxide.

XII.3 Experimental Equipment

The experimental work entails the injection of carbon dioxide or a flue gas surrogate mixture of carbon dioxide and nitrogen into a Ferron/Emery coal sample to comprehend coupled phenomena (adsorption, mechanical swelling, permeability reduction). The instrument required for this carbon storage characterization was fabricated in the Chemical Engineering Department's laboratories at the University of Utah. As has been indicated, the chemisorption of carbon dioxide is accompanied by dimensional changes in coal samples. This necessitates the ability to measure poroelastic (or otherwise) deformation.

XII.3.1 Poroelastic Measurements

Variations in pore pressure in a reservoir can cause variations in the total in situ stresses (and effective in situ stresses). Concurrently, differential variations in the effective in-situ stresses produce differential deformations in the rock matrix. The deformations in the rock were measured by using a strain gauged cantilever system, measuring the displacement along three orthogonal axes in real-time: two radial and one axial direction, as seen in Figure 43. The strain, rather than deformation, provides a better metric as it relates the displacement compared to the initial length of the solid. One well-known definition for strain is:

$$\varepsilon_i = \frac{\delta_{initial} - \delta_{final}}{\delta_{initial}} \tag{13}$$

where ε is the calculated strain (mm/mm), the subscript, i, indicates the direction of the strain, δ is the dimension in the direction consistent with "i" (mm), either before or after the displacement was experienced. In this research, ε_{t1} and ε_{t2} will be used to denote the radial strains that occur perpendicular to the axis of a horizontally cut core plug and perpendicular or parallel to the subhorizontal bedding planes in the samples, respectively. ε_A is the strain in the axial direction. The sign convention follows geomechanical standards, where a positive strain indicates compression (shrinking), and a negative strain measures expansion (swelling). Following standard practice and neglecting second-order terms, the volumetric strain is approximated as the summation of each of the three individual orthogonal strains ($\varepsilon_V = \varepsilon_{t1} + \varepsilon_{t2} + \varepsilon_A$).

The effective stress σ' (psi) felt by the rock is the difference between the applied stress σ and a fraction of the pore pressure P_p, $\sigma' = \sigma - \alpha P_p$. In general, this relationship is a tensor. However, for the experimentation here the medium can be considered as being isotropic and the effective stress is simply equal to the confining pressure minus some fraction of the pore pressure. For the purposes herein, subtract the entire pore pressure, to give the so-called Terzaghi effective stress. This implies that Biot's poroelastic parameter, α, is unity – consistent with primary deformation in the cleats.

The bulk modulus, K, as shown in Equation (14) is the ratio of a change in the Terzaghi effective mean stress to the consequent volumetric strain.

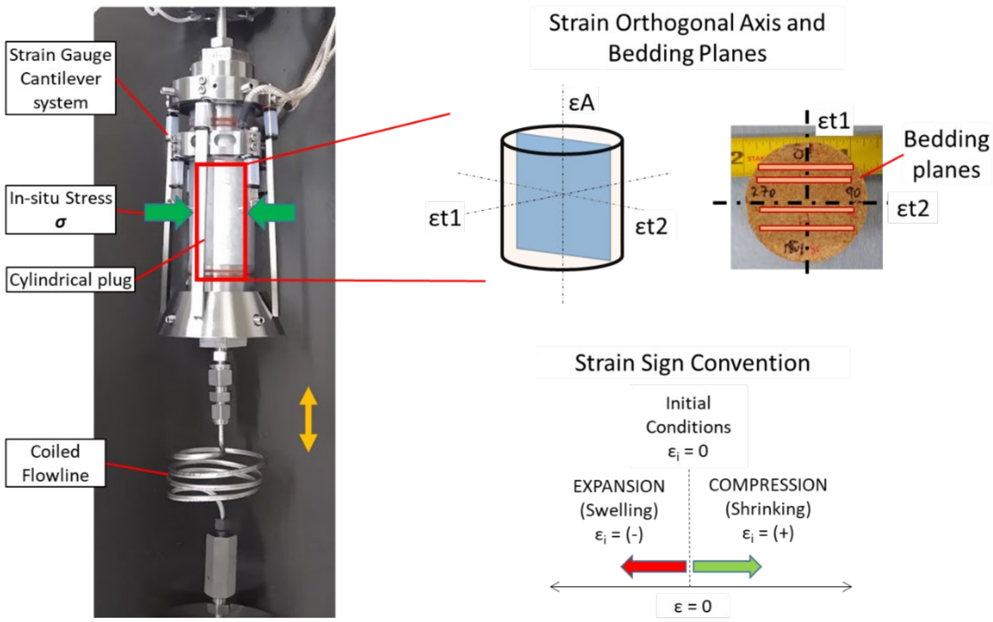

Figure 43. Schematics of the triaxial strain cantilever system. The radial strain measurement devices are aligned parallel and perpendicular to the observed bedding of the rock sample. The sign convention indicates positive strain for compressive events.

$$K = \frac{\Delta(\sigma_{ii}/3 - P_p)}{\Delta(\varepsilon_{ii})} \qquad (14)$$

XII.3.2 Flow Tests

The fundamental properties measured in the apparatus are pressure, temperature, and volume of the fluids. These were recorded continuously throughout the entire experimental protocol. Figure 44 is a schematic of the experimental apparatus and the flow path from the syringe pump inlet to the outlet vented to the atmosphere after leaving the pressure vessel and the back pressure valve. The components of the system are as follows.

a) Sample. A cylindrical plug of a representative rock sample is jacketed with a shrink-fit Teflon membrane that provides a hydraulic barrier between the fluid in the pore network and the fluid in the high-pressure chamber used to provide confining pressure. The sample is connected via the upstream and downstream flowlines to allow injection or extraction of fluids to/from the sample.
b) Syringe pump. This precision pump provides the driving force for the fluids to flow through the sample. It can be operated at constant pressure or constant

flow rate. It has a maximum capacity of 500 mL. The flow rate used in the experiments was between 2 and 5 mL/min.

c) Confining Pressure Chamber (Pressure Vessel). The sample is installed in a pressure vessel. Within the vessel, pressurized hydraulic fluid simulates the in-situ stress conditions.

d) Back-Pressure Valve. Determines the maximum flowing pressure maintained in the sample itself by regulating the exit pressure.

e) Densitometer. Indicates the density of the fluid in the flowline; particularly useful when both nitrogen and carbon dioxide were injected together.

f) Vent. Downstream of the densitometer, exiting fluid was vented to the atmosphere, routed to sampling bags, or diverted to devices for measuring volumetric flow rate.

g) Pressure Sensors. The system included multiple pressure transducers to monitor and record the confining pressure, as well as the upstream and downstream pressures.

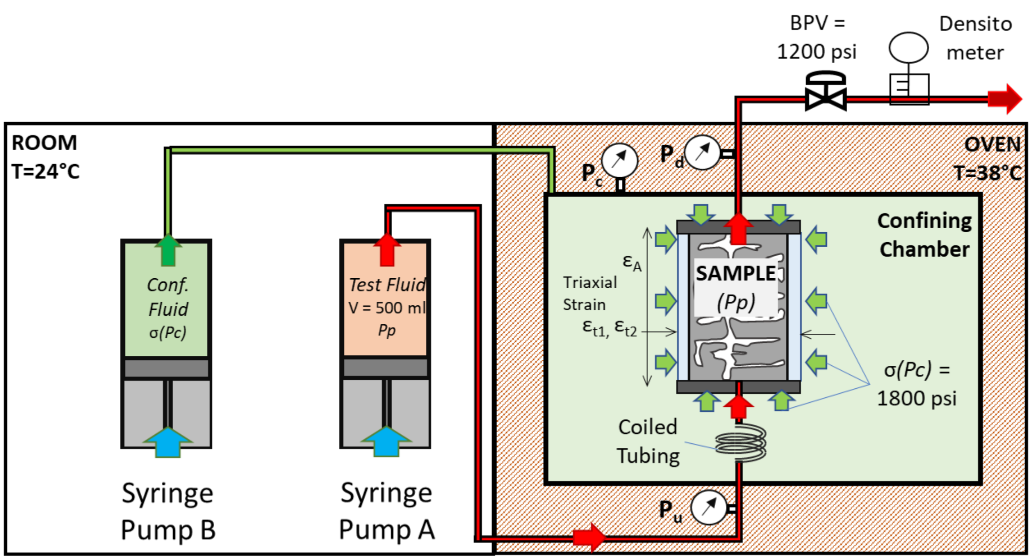

Figure 44. Schematic of a flow tests experiment. Fluid is injected by using a syringe pump (labeled as Pump A) connected through a ported endcap to the jacketed sample. The outlet incorporates a back-pressure valve as a flow restrictor. The confining pressure chamber simulates the in-situ applied stresses. The confining pressure itself is applied with Pump B.

XII.4 Flow in Ferron Coal

The experiments described above assessed the dimensional change of the formations when gases were injected. We anticipate that with dimensional changes there may be changes in the ability to move gases through the samples. Flow measurements were carried out in conjunction with the injection of different gas mixtures.

XII.4.1 Overview

The flow experiments characterized the response of the coal at representative in situ conditions (P = 1500 psi,[37] T = 38°C) to some of the different fluids that compose post-combustion flue gas: N_2, CO_2, and gas mixtures N_2-CO_2: 80:20 and 50:50. Argon was used as an inert fluid for reference and to flush the samples between runs. The experimental setup enables a steady-state flow scenario by injecting fluid at a pre-determined and controlled back pressure that simulates the bottomhole (in situ and at the coal face at depth) injection pressure. The syringe pump used for injection has a 500 mL displacement piston that operates either at constant pressure or constant volumetric rate. The measured parameters in the experiments are the pressure differential between the upstream (inlet) and the downstream (outlet), the flowline temperature, and a densitometer signal. Sample strains were also measured to evaluate the response of the rock when exposed to the various fluids. The permeability, k_g, was derived from the Darcy equation written approximately for a compressible fluid (Song et al., 2004).

$$k_g = \frac{2P_a \mu q_a L}{(P_1^2 - P_2^2)A} \tag{15}$$

where k_g is the absolute permeability to gas (m^2), P_a is the atmospheric pressure (Pa), μ is the pressure-dependent viscosity (Pa·s), q_a is the flow rate at atmospheric pressure (m^3/s), L is the sample length (m), P_1 and P_2 are the upstream and downstream pressure (Pa), and A is the cross-sectional area of flow (m^2). The apparatus is the same that was described in Figure 44. The experimental constraints are shown in Table 10.

Table 10. Operating parameters for the flow tests.

Parameter	Value	Units
Constant Volume Rate	2 to 5	ml/min
Back-Pressure	1200	psi
Confining Pressure	1800	psi
Initial Pore Pressure*	Vacuum	psi
Sample Temperature	38	°C
Room Temperature	24	°C

The downstream pressure (outlet) was controlled by the back-pressure regulator. A flow rate of 5 mL/min (or less) was experimentally optimized to avoid freezing at the back pressure regulator when the CO_2 decompressed from the flowline pressure of 1200 psi to atmospheric pressure. CO_2 flow rates higher than 6 cm^3/minute produced condensation and freezing at the back pressure valve, impeding the proper function of the membrane in the back-pressure valve, complicating the entire experiment.

[37] The experiments were run at a slightly lower pressure than the 1500 psi used for the reservoir modeling. 1200 psi was used reflecting a small reservoir depletion due to previous gas production.

XII.4.2 Sample Preparation

Sample preparation involved heating for 72 hr in an oven at 140°C to eliminate moisture and remnant volatiles, followed by storage in a vacuum desiccator with alumina beads to maintain the moisture level low. After the sample was installed in the pressure vessel (Figures 43 and 44), representative reservoir conditions were replicated by applying a confining pressure, σ, of 1800 psi, and maintaining the temperature in the oven at 38°C for 12 hr, to allow thermal expansion of the confining fluid (Paratherm) and equilibration of stresses within the sample, while maintaining the pore pressure at vacuum conditions. The back-pressure valve was set to 1200 psi.

XII.4.3 Flow Testing with coal

The injection pump was filled with the appropriate fluid and pressurized to 1200 psi, allowing, in the case of carbon dioxide, the transition from a gas to a liquid phase before injection. All processes are assumed to be isothermal. At the beginning of every test, the flowlines and the sample were evacuated. This ensured a consistent and systematic method to compare the development of strains and permeability between flow tests.

XII.4.3.1 Coal Flow Test with Ar and N_2

A flow test with Ar and N_2 measured the response of an inert gas, Ar, and compared this response to the interaction of N_2 with the coal. The sample was flooded with argon at a pore pressure of 1200 psi and this injection was initiated at a constant flow rate. The results are shown in Figures 45A through 45D.

For the argon injection, event A in the plots (Figures 45A through 45D), the fluid is injected at a volumetric flow rate of Q = 5 cm^3/min from time 0 to 0.9 hrs. In the pressure plot, top left, the flowing upstream (P_fu) and downstream (P_fd) pressures indicate steady-state flow with no large variations. The applied hydrostatic pressure, σ, (confining pressure applied to the sample) remained constant during the entire experiment. The plot 'ΔP', bottom left, shows the pressure differential between the inlet flowing pressure, P_fu, and the outlet flowing pressure, P_fd. The differential pressure, ΔP, increases from zero to ~6 psig over the first 0.2 hr, as the fluid is compressed and pressurized until the pore pressure is slightly larger than the back pressure valve setting, at which point the fluid starts exiting the pressure vessel. The flowing pressure remains constant during the injection of the Ar. The 'strain' plot (Figure 45C) shows the linear orthogonal strains, ε_{t1}, ε_{t2} and ε_a,[38] and the volumetric strain, ε_V, which is approximated by summing the three orthogonal linear strains. From the beginning of the injection, the volumetric strain, ε_V, reduces gradually from zero until it stabilizes at ε_V =-0.005 [m^3/m^3]. The negative value indicates expansion, a slight swelling as the pore pressure increases. The permeability, calculated by using gas in Darcy's relationship is k_g = 3.5 mD, remained nominally constant during the argon

[38] Recall that these are two perpendicular radial strains experienced by the core plug and the axial strain.

injection. At time t = 0.9 hr, the argon injection was terminated, followed by the application of a vacuum to remove remanent gas from the pore network, while refilling the pump with N_2.

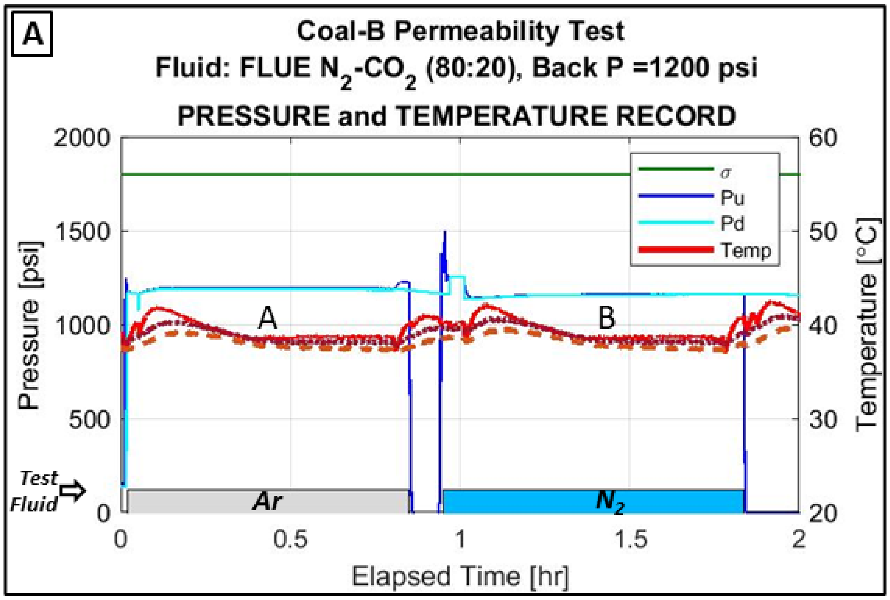

Figure 45A. Synthetic flue gas was injected through Coal B. Before that argon and nitrogen were flowed. This figure shows the pressure response and oven temperature when flowing argon followed by nitrogen.

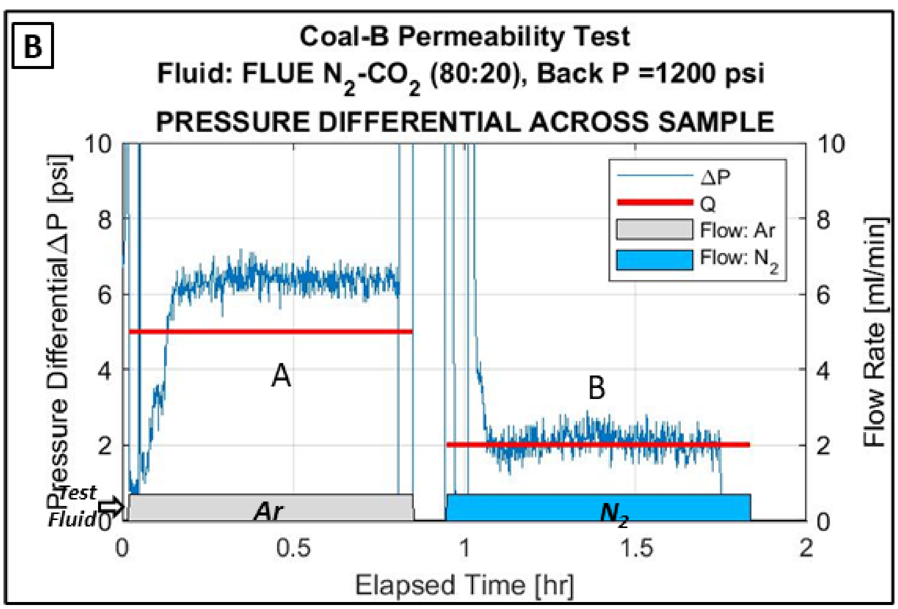

Figure 45B. Synthetic flue gas was injected through Coal B. Before that argon and nitrogen were flowed. This figure shows the differential pressure response (difference between the upstream inlet pressure and the downstream outlet/exit pressure) and the upstream volumetric flow rate when flowing argon followed by nitrogen.

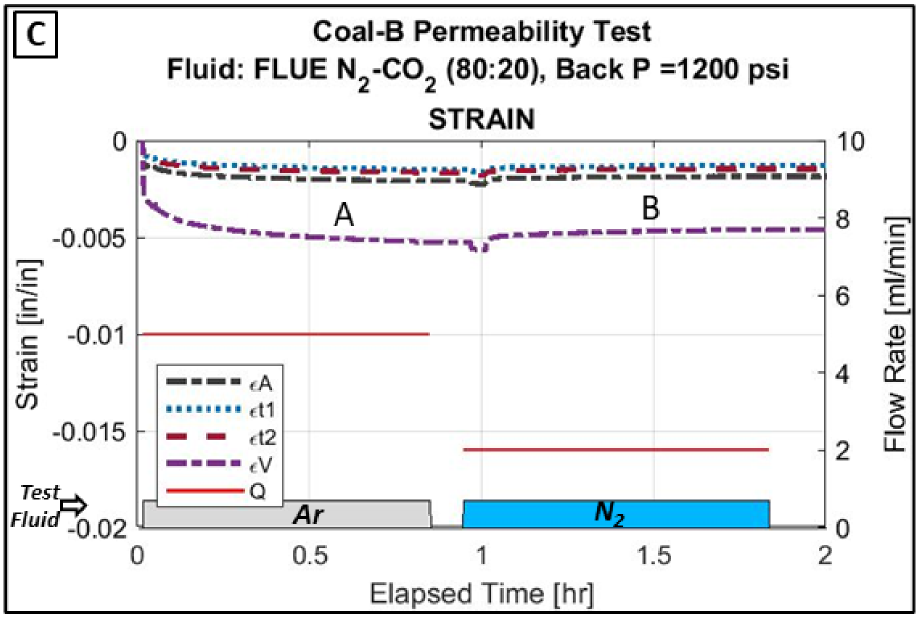

Figure 45C. Synthetic flue gas was injected through Coal B. Before that argon and nitrogen were flowed. This figure shows the volumetric strain and the upstream volumetric flow rate when flowing argon followed by nitrogen. Recall that a negative strain (change in dimension or volume divided by original dimension or volume) indicates expansion.

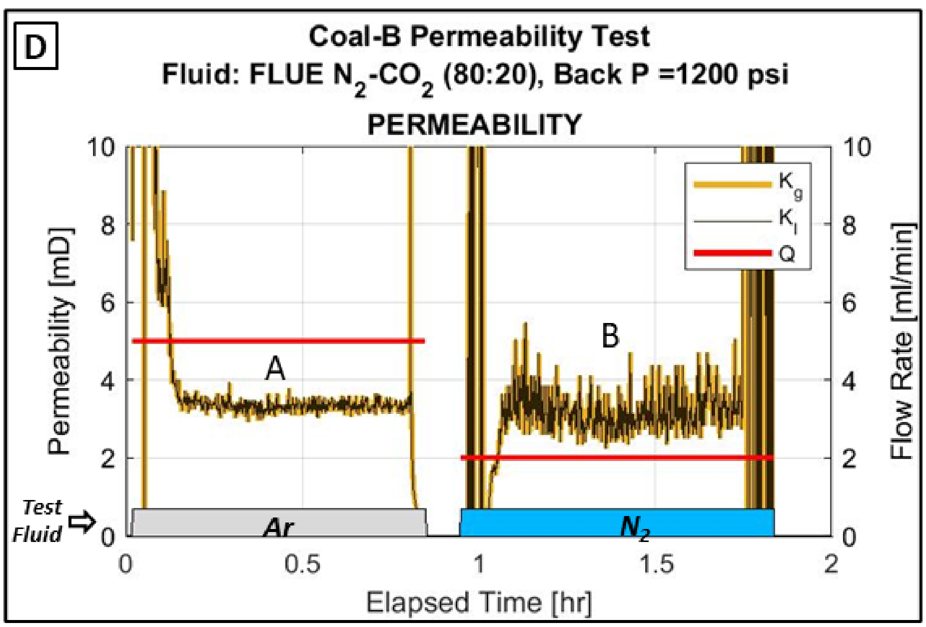

Figure 45D. Synthetic flue gas was injected through Coal B. Before that argon and nitrogen were flowed. This figure shows the absolute permeability to the flowing gas and the upstream volumetric flow rate when flowing argon followed by nitrogen.

The N_2 injection started at t=1.0 hr, at a constant volumetric flow rate of 2 cm^3/min. The overall response is similar to that seen for argon. The lower injection rate generates a constant differential pressure, ΔP, of 2psi, which in turn leads to a relatively constant permeability to nitrogen, k_g = 3.5 mD, (the same as for argon), which suggests consistency between the data input, the measured parameters, and the calculated output. The strain changes slightly due to the lower flowing ΔP for nitrogen.

In conclusion, it was validated that the N_2 in the coal behaved as a relatively inert fluid since it replicates the response of Ar. When nitrogen is injected as an ECBM fluid, methane is extracted from the because of the reduced partial pressure of the nitrogen flowing through the cleats.

XII.4.3.2 Coal Flow Test with CO_2

This flow test (Figure 46A through D) started with applying the confining pressure at σ = 1800 psi and applying a vacuum to remove as much residual gas as possible. This was followed by an initial injection of Ar, event C in the figures, for 1 hr to set the sample at a pore pressure, P_p, of 1200 psi without any adsorption occurring. The behavior is consistent with the previously described argon injection: event A, k_g = 3.2 mD and ε_V = -.005 m^3/m^3.

Next, CO_2 was used to fill the pump piston to 800 psi. This is the maximum bottle pressure from the industrial gas supplier. The pump piston was then "stroked" to compress the carbon dioxide to an injection pressure of 1200 psi, consistent with the pressure in the sample. This increment in pressure was achieved by stroking the pump piston and reducing the pump chamber volume from 500 ml to 160 ml. This reduced remaining volume restricted the amount of CO_2 available for injection and reduced the elapsed time before it was necessary to refill the pump. Regardless, the pump was activated to move this volume of gas into the coal sample. Each pump stroke cycle (injecting the 160 ml of pressurized fluid) lasted ~2.5 hr. Each separate injection cycle (stroke) is represented by a red bar on top of the plots in Figures 46A through D, and these are identified with the events D, E, F, and G.

The first CO_2 injection at an upstream volumetric flow rate of Q = 2 ml/min, event "D", caused an increasing upstream flowing pressure (P_fu), while the downstream pressure (P_fd) was constrained by the back pressure valve which had been set at 1200 psi. The ΔP increased continuously from 3 to 45 psi. The strain plots (Figure 46C) record a drastic and immediate swelling of the coal in contact with the CO_2, from ε_V = -0.005 to -0.025 m^3/m^3 (recall that compression is positive strain and expansion is negative). Greater swelling is recorded by the axial strain measurement, ε_A, with a slight anisotropy between the radial strains: The ε_{t2} strain (parallel to the bedding planes based on pre-test CT scanning) evolved to be larger than ε_{t1} (perpendicular to the bedding planes).

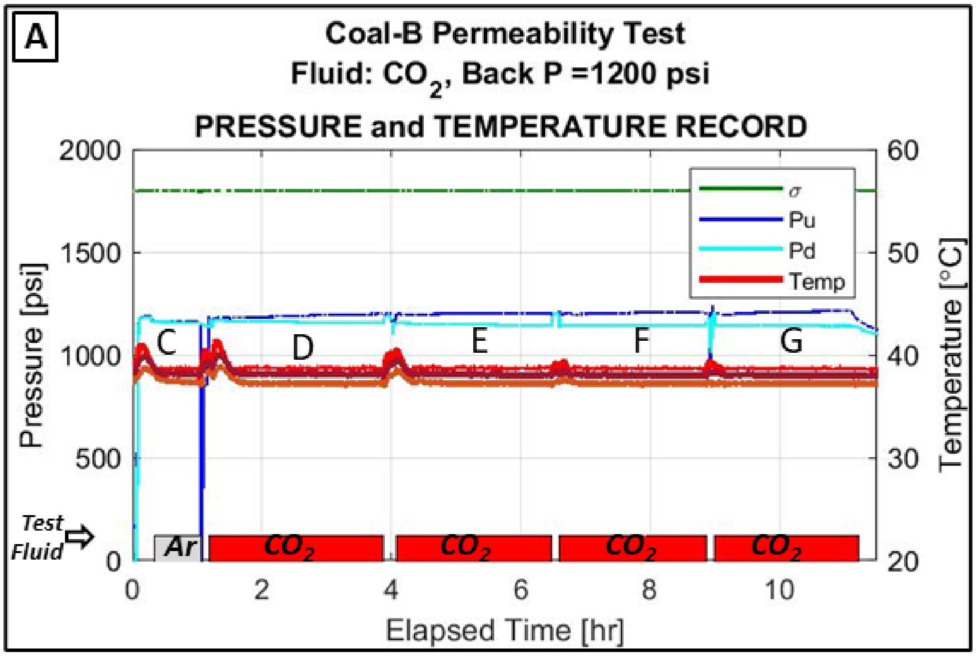

Figure 46A. CO_2 was injected through Coal B. Before that argon was flowed. This figure shows the pressure response (upstream and downstream) and oven temperature when flowing argon followed by CO_2. The confining pressure, σ, is also shown (1800 psi).

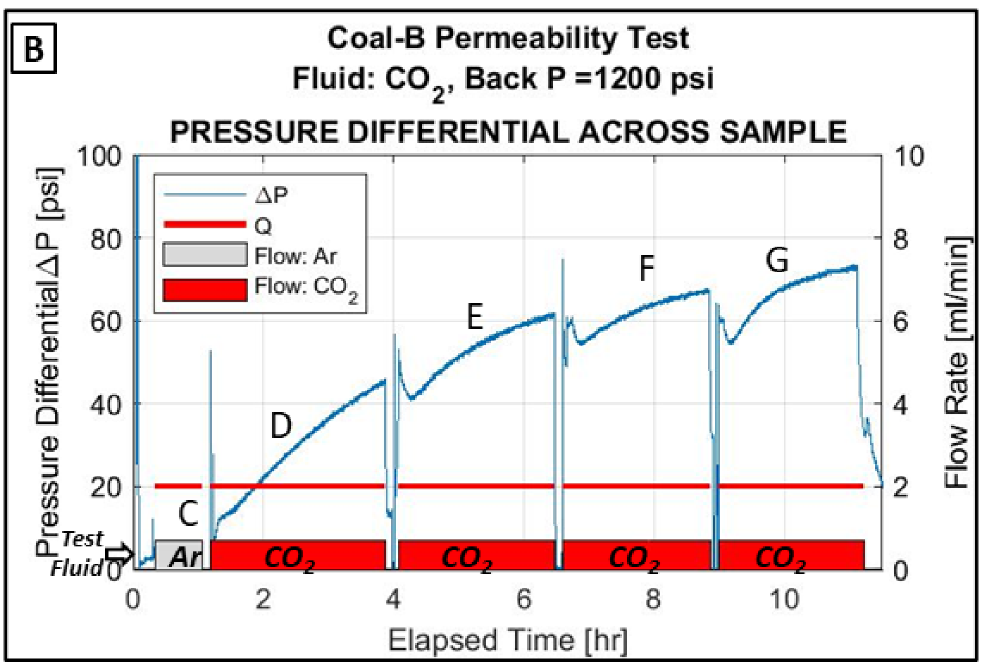

Figure 46B. CO_2 was injected through Coal B. Before that argon was flowed. This figure shows the differential pressure response (difference between the upstream inlet pressure and the downstream outlet/exit pressure) and the upstream volumetric flow rate when flowing argon followed by CO_2.

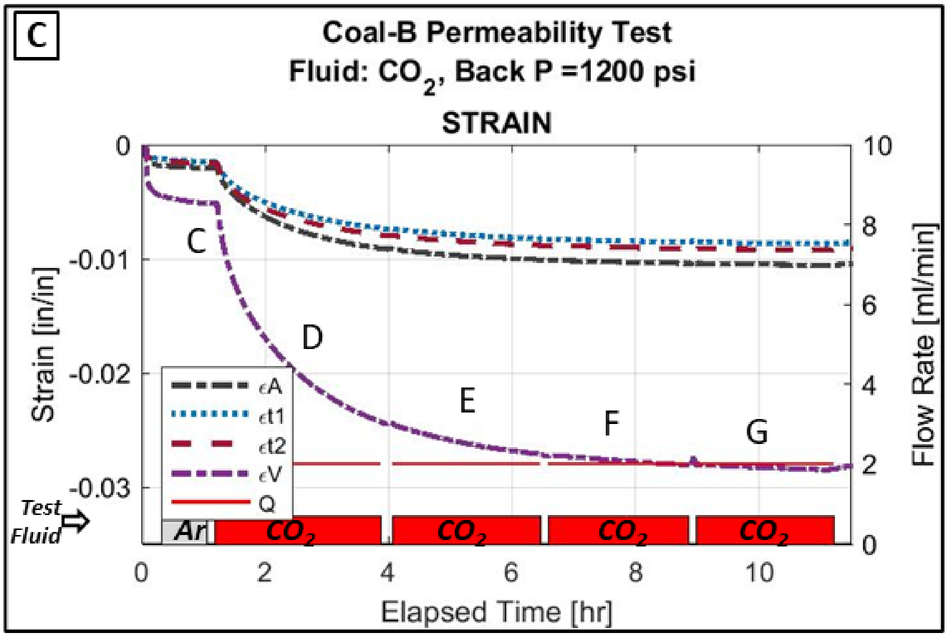

Figure 46C. CO_2 was injected through Coal B. Before that argon was flowed. This figure shows the axial, both radials, and volumetric strains and the upstream volumetric flow rate when flowing argon followed by CO_2. Recall that a negative strain (change in dimension or volume divided by original dimension or volume) indicates expansion.

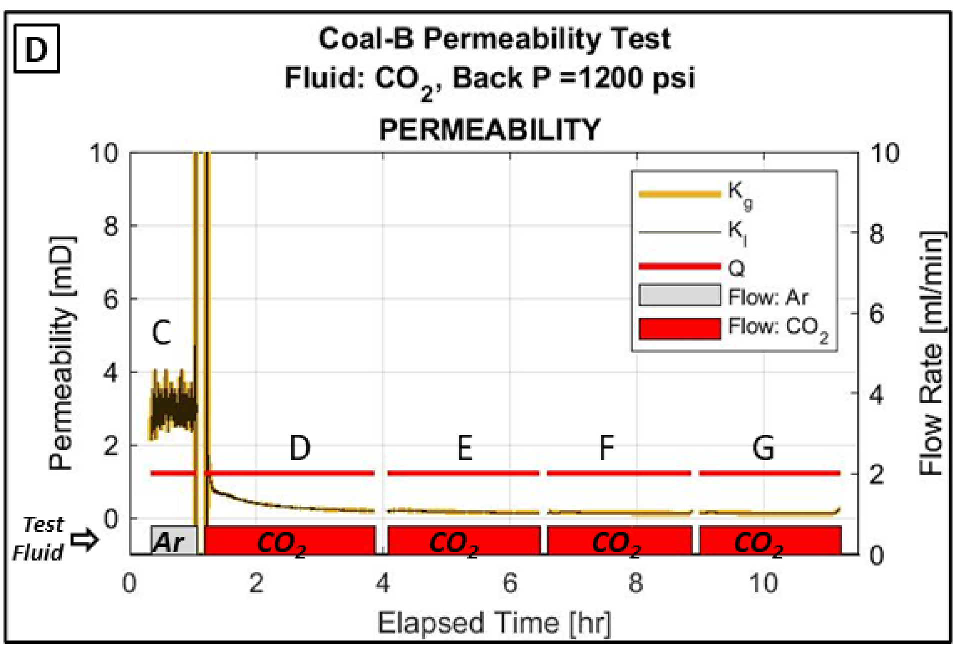

Figure 46D. CO_2 was injected through Coal B. Before that argon was flowed. This figure shows the absolute permeability to the flowing gas and the upstream volumetric flow rate when flowing argon followed by CO_2. Notice the significant reduction in permeability when CO_2 was flowed.

The combined effect of increasing the differential pressure, ΔP, and concurrently reducing the effective stress, σ', (basic pore volume compressibility) with the coal swelling, produced a reduction in the permeability to CO_2 from k_g = 3 to 0.15 mD during injection cycle D.

The subsequent pump strokes, represented by events E, F, and G, maintain the same injection parameters, Q = 2 ml/min, and a back pressure of 1200 psi. The trend of the initial injection continues for the ΔP curve and the volumetric strain, ε_V.

At the end of event G, after an elapsed time of 10 hr of CO_2 injection, the upstream flowing pressure reached P_fu = 1275 psi, producing a ΔP of approximately 75 psi, while the sample experienced a final volumetric strain increase when the strain plateaued at ε_V = -0.28 m^3/m^3. The permeability ultimately reduced to 0.10 mD.

The experiment confirmed and replicated the permeability reduction due to coal swelling attributable to CO_2 flooding, as has been reported by various authors. The swelling-consequent reduction in permeability represents a complication for carbon sequestration projects in coalbed methane fields, despite the high storage capacity of the coal. The processes of mass transport, poroelastic alterations, and adsorption are lengthy, up to 10 hr for the small size sample (3" x 1.5" OD). From an engineering perspective, this can be mitigated because of the geology at this location. The Ferron sandstone is predicted to act as the transportation medium to coal well away from the wellbore progressively bypassing areas of reduced permeability. In addition, periodic hydraulic stimulation (increasing the injection pressure) can provide local fracturing channels that bypass these zones. Even more intriguing considerations follow - where the potential for flue gas injection has been simulated.

XII.4.3.3 Coal flow test with Surrogate Flue Gas

Post-combustion flue gas was simulated with an N_2:CO_2 mixture at a volumetric composition of 80:20 at an injection pressure of 1200 psi. The testing results are shown in Figure 47. The mixture in the chamber of the syringe pump was prepared at room temperature (T=24°C) and a pressure of 800 psi (pressure from the bottles) and then pressurized to 1200 psi, which is the flowing pressure. The mixed gas volume in the pump reduces from 500 mL to 310 mL with the increase in pressure. At a volumetric flow rate of Q = 2 mL/min, this pressurized volume was adequate for continuous flow for 2.5 hours, until the piston reached the end of its stroke.

The experiment started with the evacuation of the flowline and the sample. This was followed by a period of Ar and N_2 injection denoted as events "H" and "I" in Figure 47. The injection of these gases produced a steady ΔP, and relatively constant values were recorded for the absolute permeability, k_g, and volumetric strain, ε_V, over event intervals of 1 hr each. The injection of the simulated flue gas started at a time of t = 2 hr. This entailed pumping three batches of flue gas, indicated by the events J, K, and L, in Figure 47.

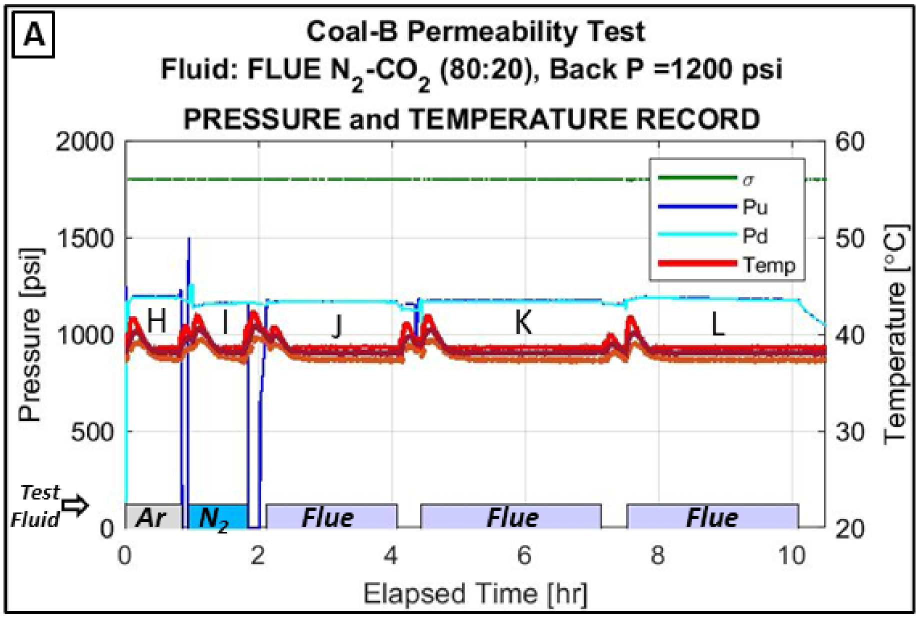

Figure 47A. An 80:20 N_2:CO_2 "mixture" was injected through Coal B. Before that argon and nitrogen were flowed. This figure shows the pressure response (upstream and downstream) and oven temperature. The confining pressure, σ, is also shown (1800 psi).

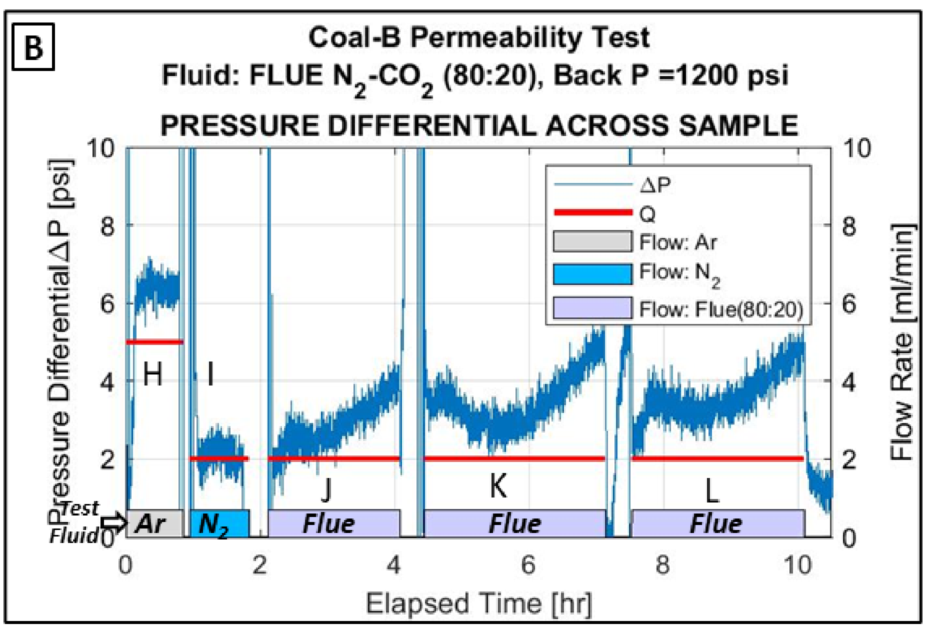

Figure 47B. An 80:20 N_2:CO_2 "mixture" was injected through Coal B. Before that argon and nitrogen were flowed. This figure shows the differential pressure response (difference between the upstream inlet pressure and the downstream outlet/exit pressure) and the upstream volumetric flow rate.

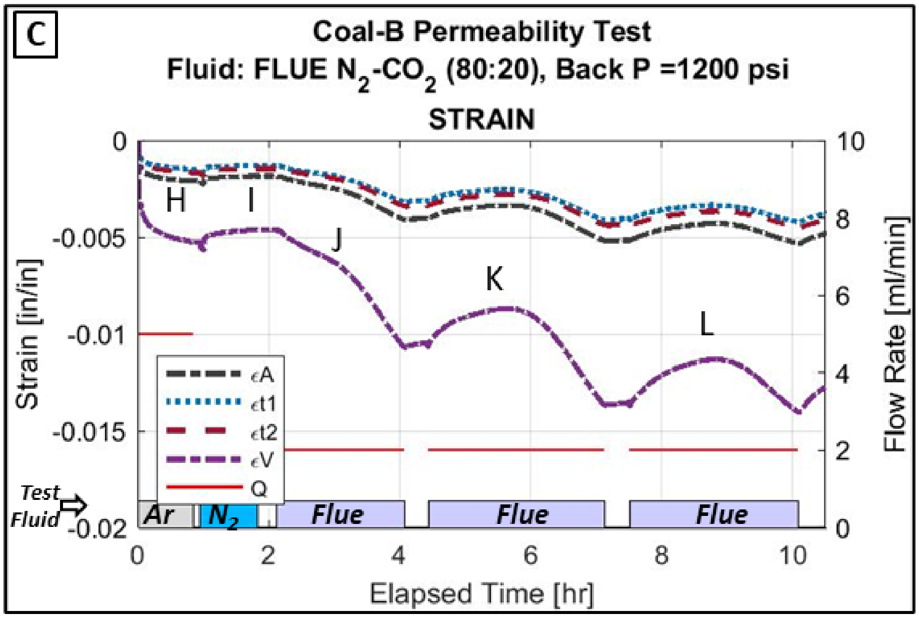

Figure 47C. An 80:20 N_2:CO_2 "mixture" was injected through Coal B. Before that argon and nitrogen were flowed. This figure shows the axial, both radial, and volumetric strains and the upstream volumetric flow rate. Recall that a negative strain (change in dimension or volume divided by original dimension or volume) indicates expansion.

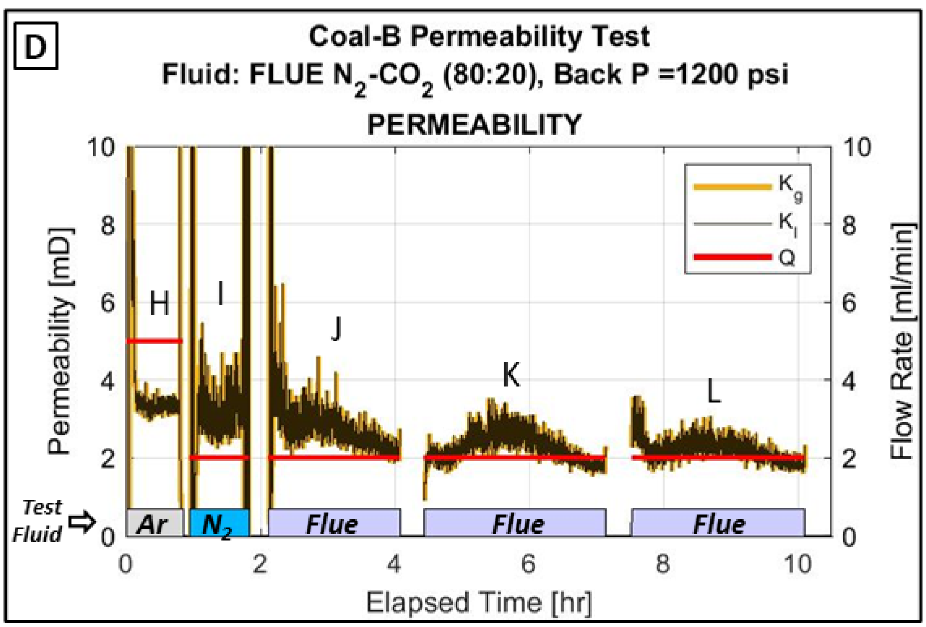

Figure 47D. An 80:20 N_2:CO_2 "mixture" was injected through Coal B. Before that argon and nitrogen were flowed. This figure shows the absolute permeability to the flowing gas and the upstream volumetric flow rate when flowing argon followed by CO_2.

In the initial flue gas injection, event J, no major pressure variations were observed in the pressure record although the differential pressure increased from 2 to 4 psi. The strain record indicates that the coal swelled due to the fraction of CO_2 in the mixture, reducing to ε_V=-0.011 m^3/m^3 by the end of the pump stroke (during event J). The permeability reduced slightly from 2 to 1.8 mD. At the end of event J (t = 4 hr), the coal sample was valved in when the piston had reached the end of its stroke. Isolating the sample by closing the valves maintained the sample pressure, while a new batch of surrogate flue fluid was prepared - refilling and pressurizing the pump to 1200 psi.

Event K occurred over an elapsed time of 5.5 to 7.5 hr. The injection of the simulated flue gas continued at the selected representative in-situ conditions after preparing a new mixture batch in the pump. The pressure differential, ΔP, decreased from 3.5 to 2.5 psi during the first half of pumping batch K (elapsed time 4.5 to 5.5 hr) but ramped up to 5 psi for the second "period" of the batch (elapsed time 5.5 to 7.0 hr). In the strain record, however, the strain reacted differently than had been expected. The strain increased from ε_V = -0.011 m^3/m^3 to ε_V = -0.008 m^3/m^3, indicating a volumetric contraction for the first half of the pumping period. This was followed by swelling with the volumetric strain becoming more negative; ε_V = -0.014 m^3/m^3 by the end of the pump stroke at t = 7.0 hr. Figure 47C shows humps in the strain behavior over individual injection batches. The 'hump' pattern in the strain during event K correlates with the ΔP curve:

When the coal shrinks, the flow channels (cleats and fractures) open, resulting in a reduction of the pressure differential; when the coal swells, there is more resistance to flow with the subsequent increase in the ΔP.

The permeability fluctuates from 1.8 mD when 'event K' starts increasing to 2.3 mD at the maximum shrinkage and reducing further down to 1.5 mD once the coal swells. **What is the cause of this behavior and why is it so important from an operational perspective?**

Event 'L', from t = 7.5 to 10 hr, follows the same pattern as event 'K', repeating the shrinking and swelling cycle when flowing a batch of simulated flue gas. The maximum swelling occurs at ε_V = -0.014 mm^3/mm^3 suggesting a final stabilization and this is an indication of the maximum storage capacity with flue gas injection during this cycle.

The hypothesis for the humped behavior is the stratification of two supercritical fluids[39] in the vertically oriented pump chamber, due to the large density difference between the species (ρ_{N2} = 3.1 mol/l, ρ_{CO2} = 17.9 mol/l) when preparing the mixture in the pump

---

[39] Nitrogen has a critical point of 126.2 K (−147 °C) and 3.4 MPa (34 bar). Therefore, nitrogen in the gas cylinder at 1200 psi (8.3 MPa) is a supercritical fluid. The critical point for carbon dioxide is critical temperature (304.13K, 31.0°C) and critical pressure (7.3773 MPa, 1,070 psi).

chamber. The concentration of each species is determined as a function of the vertical position z (or the normalized vertical position, z/L) as indicated in Figure 48. As the piston moves upward at a constant rate, yielding an upstream volumetric flow rate,[40] Q, the mixture leaving the pump -and injected into the sample - has a concentration that is a function of z/L. Since the pump operates at a constant rate, the normalized horizontal axis, z/L, can also be considered as dimensionless time, or dimensionless volume.

The polynomial fit for the estimated CO_2 concentration in the flow stream entering the sample is $Y_{CO2} = Ax^2 + Bx + C$ [wt.%]. (A = 0.5735, B = 0.0821, and C = 0.2164). The concentration of N_2 is $Y_{N2} = 1 - Y_{CO2}$. These concentrations are plotted in the upper left-hand panel of Figure 48.

For every flue gas batch, extrapolating the measurements by Hendry et al., 2013, the estimated concentration at the beginning of the injection time (z/L=0) is N_2 dominated (y_{N2} = 0.87, y_{CO2}=0.13 wt.%). Equality in the concentrations occurs at z/L = 0.63. By the end of the stroke (z/L=1) the remanent mixture is mostly CO_2 (y_{N2} = 0.87, y_{CO2}=0.13 wt.%).

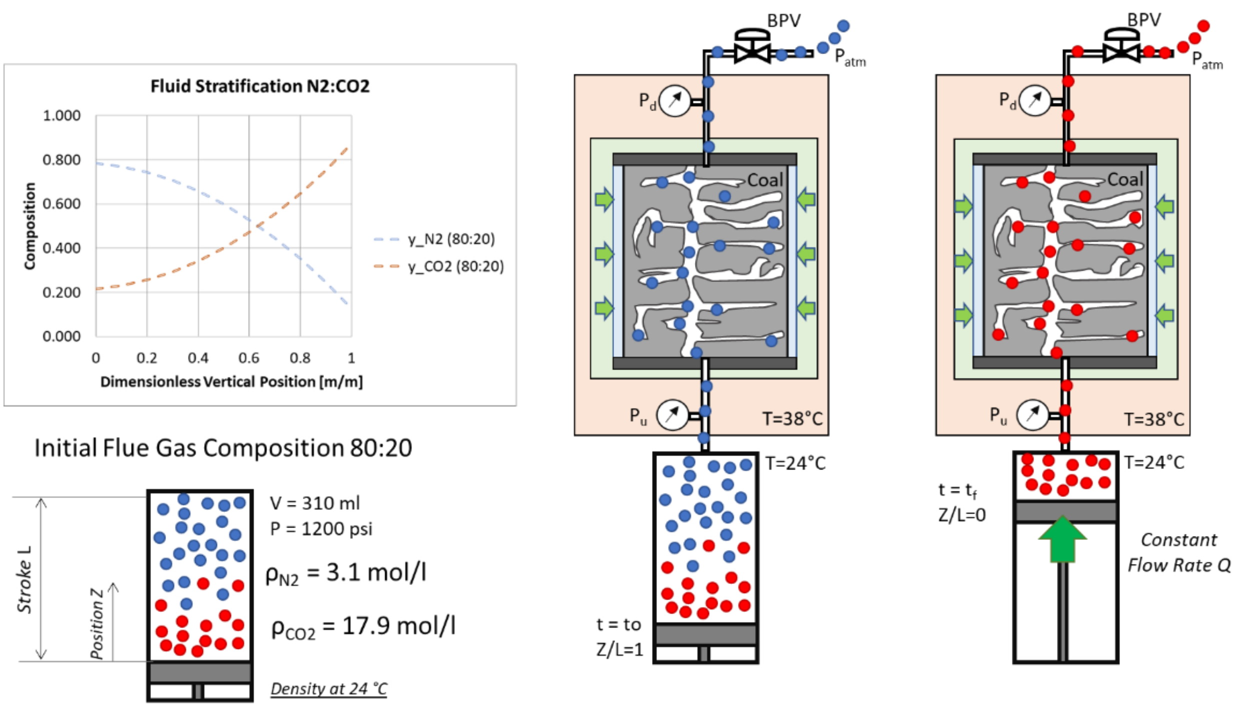

Figure 48. Schematic views of the fluid stratification and timing for surrogate flue gas injection into the sample. The upper left panel is a prediction of the concentrations (resulting from stratification). The two panels on the right show the initial injection of nitrogen, followed by CO_2 predominantly entering the sample.

[40] It is a precision screw pump.

Referring to the experimental data shown in Figure 49, for events J and L, mixture concentrations are analyzed in conjunction with the measured strains. Refer to Figure 49. For the case of the initial adsorption, event “J” in Figure 47, there are two distinguishable patterns of sorption. When the mixture is dominated by nitrogen, the sample swells modestly (or recovers/contracts after previous CO_2 exposure). Once the mixture becomes more CO_2-dominated, the rate of swelling increases and continues until the end of the pump stroke. For event “L” in Figure 47, at the beginning of the flue gas batch injection, the larger concentration of N_2 allows desorption of the CO_2 from the coal, relaxing the adsorption-induced stresses and causing a contraction of the coal matrix. When the concentrations equalize, $y_{N2} = 0.5$, $y_{CO2}=0.5$ wt.%, the relative sorption changes the induced strains in the coal. When the CO_2 concentration becomes larger, the adsorption onto the coal resumes with the resulting swelling and reduction in the flow paths (cleats and fractures) and permeability.

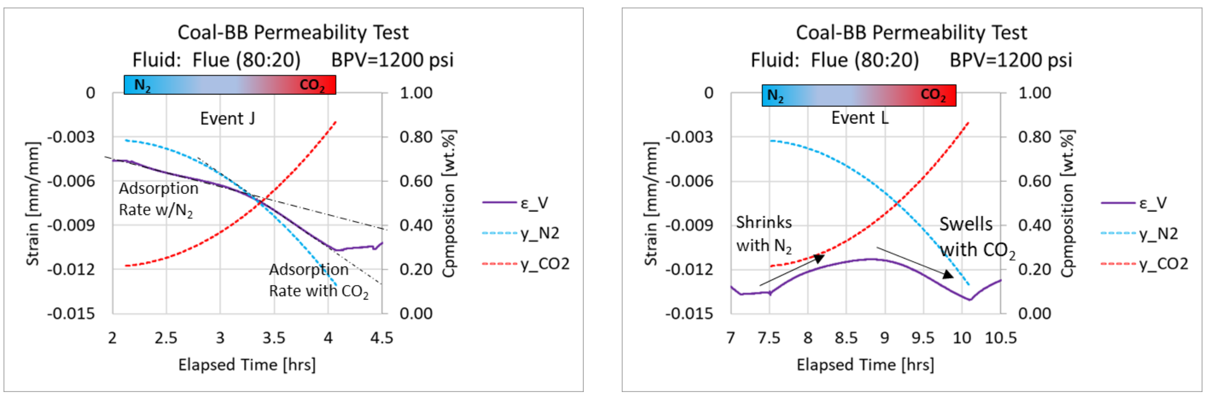

Figure 49. Flow test results for a model flue gas (nitrogen to carbon dioxide at 80:20) in coal. Comparison between the first batch injected (event “J”), and a later batch (event “L”) in the same experiment.

XII.4.3.4 Flue Gas Experiment Repeated in Sister Coal Sample

The experiment described above was repeated using a sister coal sample (Coal-AA) to verify the observations and confirm the coal’s response to simulated flue gas injection under supercritical conditions. The repeated experiment was run for a longer time to evaluate the consistency and behavior of each batch of flue gas. Six batches were prepared and pumped sequentially, in an operation lasting over 22 hours, in Figures 50A through D.

The sample was gradually “filled” with Ar (from an evacuated baseline up to 1200 psi), followed by a 1 hr period of N_2 pumping. During these injections, the sample swelled to ε_V = -0.007 m^3/m^3 due to an increase in the pore pressure, which is slightly larger than the swelling experienced by the sister sample Coal-BB (ε_V = -0.005 m^3/m^3). The strain record also displays the strain associated with subsequent CO_2 injection The pressures fluctuated during the initial period of pumping, complicating a measurement of steady permeability. The permeability of N_2 and CO_2 from the previous test are indicated with dashed lines as a reference.

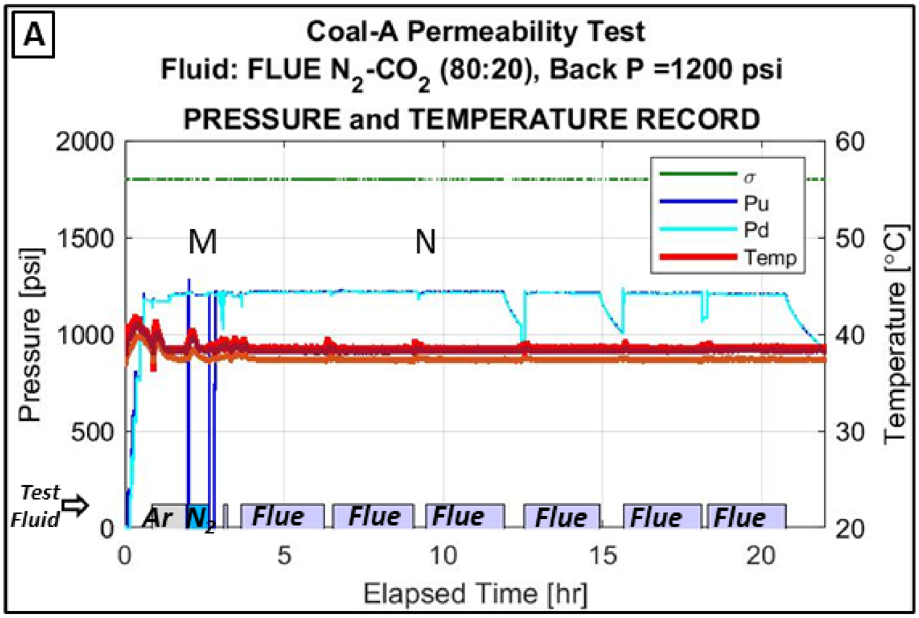

Figure 50A. An 80:20 N_2:CO_2 "mixture" was injected through Coal A. Before that argon and nitrogen were flowed. This figure shows the pressure response (upstream and downstream) and oven temperature. The confining pressure, σ, is also shown (1800 psi).

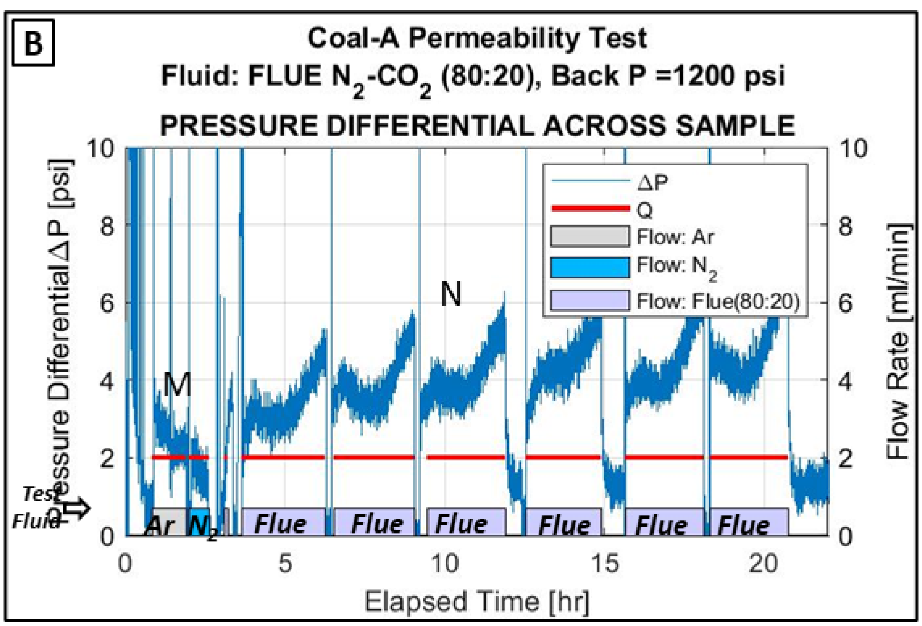

Figure 50B. An 80:20 N_2:CO_2 "mixture" was injected through Coal A. Before that argon and nitrogen were flowed. This figure shows the differential pressure response (difference between the upstream inlet pressure and the downstream outlet/exit pressure) and the upstream volumetric flow rate.

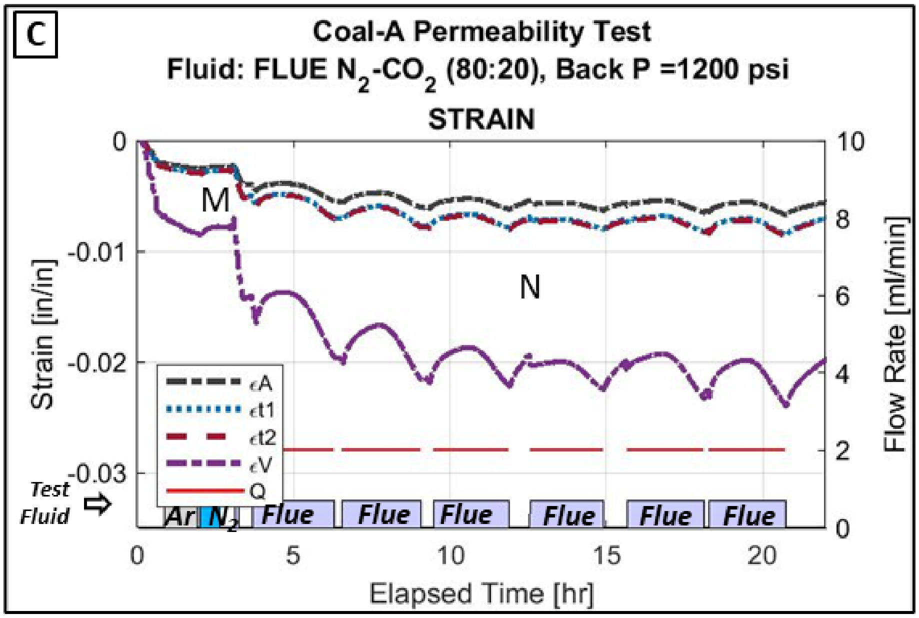

Figure 50C. An 80:20 N_2:CO_2 "mixture" was injected through Coal A. Before that argon and nitrogen were flowed. This figure shows the axial, both radial, and volumetric strains and the upstream volumetric flow rate. Recall that a negative strain (change in dimension or volume divided by original dimension or volume) indicates expansion.

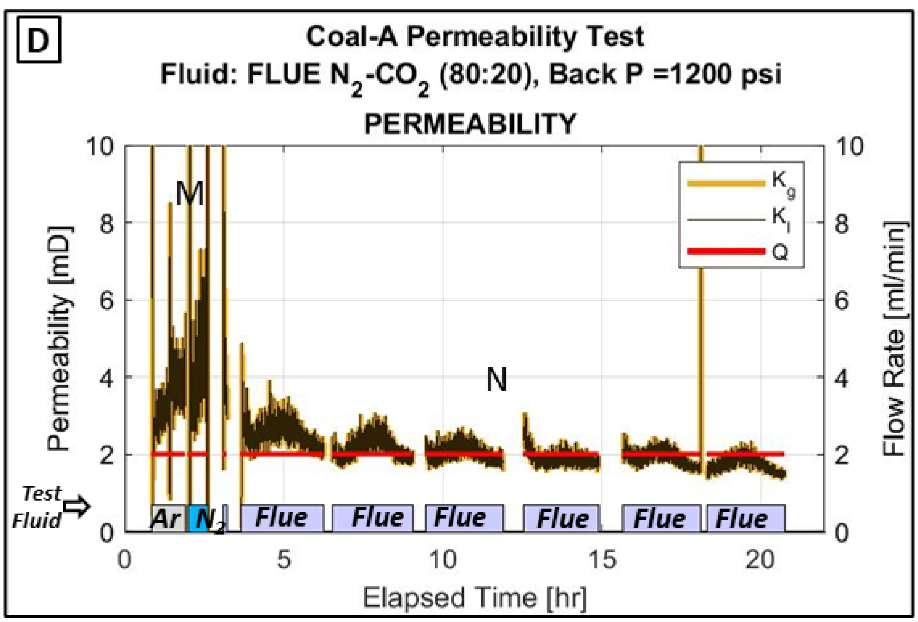

Figure 50D. An 80:20 N_2:CO_2 "mixture" was injected through Coal A. Before that argon and nitrogen were flowed. This figure shows the absolute permeability to the flowing gas and the upstream volumetric flow rate.

A short flow period of simulated flue gas at time t=2.9 hr, (Event "M") increased the volumetric strain to ε_V=-0.015 m^3/m^3. A temporary malfunction of the back pressure valve was the reason for the unstable pressures. Once the hardware issue was fixed, the flow remained steady, and the flue gas was injected under the appropriate conditions. The subsequent flue gas batches repeated the desorption/sorption sequences (Event "N"). As observed in the previous experiment, there was a series of continuous humps, oscillating between ε_V -0.020 and -0.024 m^3/m^3. The permeability followed the adsorption/desorption fluctuations and varied between 5 and 2 mD.

The periodic behavior extending over six sequences of flue gas batches in a different coal sample confirms the possibility of developing a strategy of **directly** injecting the flue gas at supercritical conditions **without a dramatic reduction in the permeability and increase in required injection pressure**.

Unlike adsorption isotherms at subcritical conditions where the adsorption is described only as a function of the pressure, this phenomenon should be related to a combination of properties - like chemical potential, and compressibility of the supercritical fluids surrounding the attachment sites for adsorption in coal.

As a very positive outcome for practical injection operations, the resulting average permeability during flue gas injection (k_g = 2 mD) does not "collapse" due to swelling as was the case for pure CO_2 injection (k_g = 0.1 mD). The shrinking and swelling cycles for every batch of stratified flue gas provide a self-healing mechanism, assuring flow deeper (farther) into the reservoir with less injection cost while retaining the storage capability for the fractional volume of pure CO_2.

XII.4.3.5 Gas Mixture 50:50

This flow experiment evaluated the coal's response to a 50:50 gas mixture of N_2:CO_2. The fluid stratification profile is described in Figure 48. This flow test followed the same sequence as for the previous simulated flue gas measurement, starting from vacuum conditions for the pore pressure, followed by a period of Ar injection, at event "O". Refer to Figures 51A through D. The initial swelling and the permeability mimic the previous experiments, with ε_V = -0.003 (m^3/m^3) and k_g = ~2.5 mD, respectively.

The injection of this 50:50 gas mixture starts with event "P". The CO_2 fraction in the mixture adsorbs in the coal and produces a rapid swelling, to ε_V = -0.015 [m^3/m^3]. The pressure differential, ΔP, in the early segment of event "P" (t = 1.6 to 2 hr) was not stable since steady-state flow had not been achieved, (requiring fine-tuning of the system settings, mainly adjusting the backpressure valve, and compensating for fluid compression) to achieve a constant downstream "restriction" at 1200 psi. Consequently, the calculated permeability is low. The later part of event "P" (t = 2 to 3 hr) experiences a differential pressure increase up to 70 psi corresponding to the increase in swelling, since the concentration of CO_2 in the fluid injected increased with time, according to the fluid stratification.

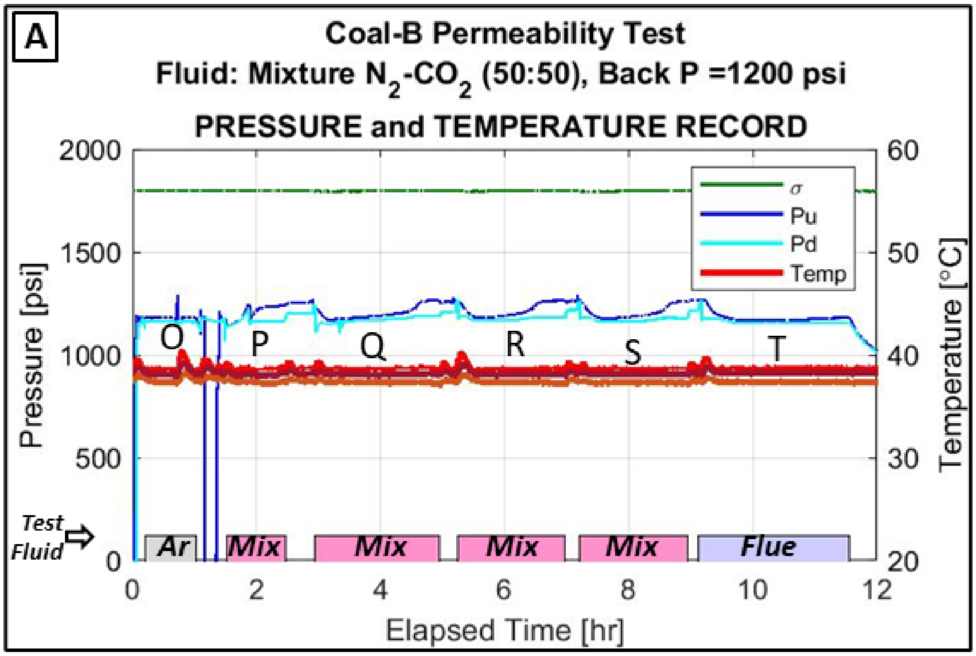

Figure 51A. A 50:50 N_2:CO_2 "mixture" was injected through Coal A. Before that argon was flowed. This figure shows the pressure response (upstream and downstream) and oven temperature. The confining pressure, σ, is also shown (1800 psi).

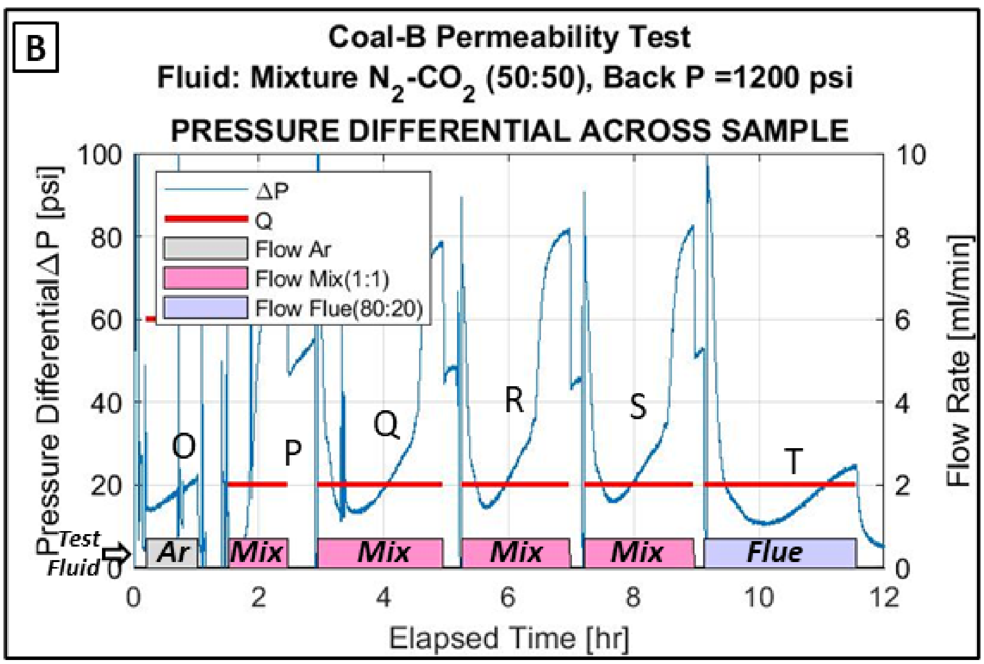

Figure 51B. A 50:50 N_2:CO_2 "mixture" was injected through Coal A. Before that argon was flowed. This figure shows the differential pressure response (difference between the upstream inlet pressure and the downstream outlet/exit pressure) and the upstream volumetric flow rate.

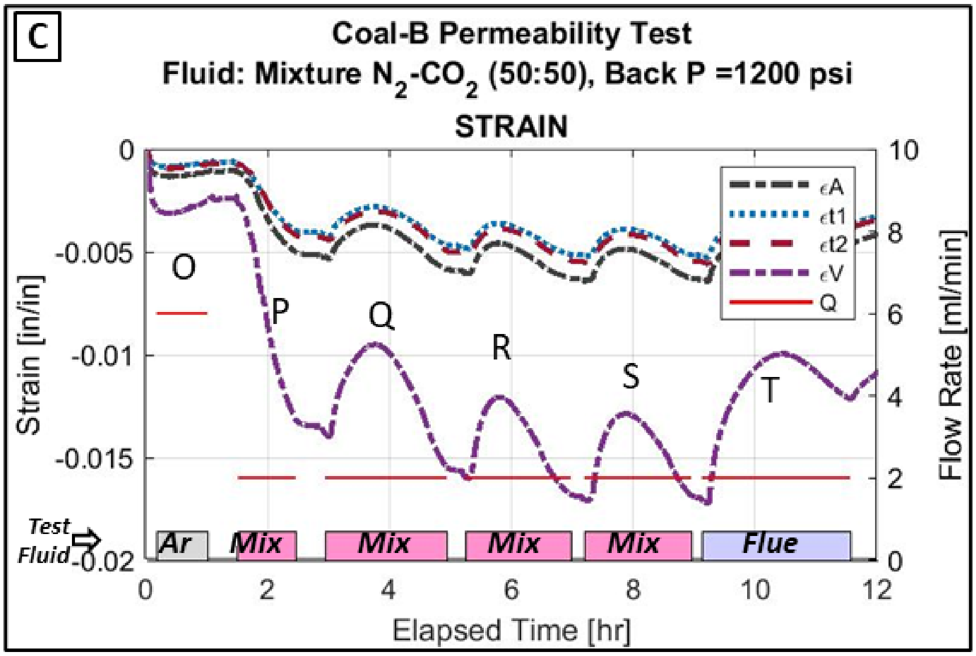

Figure 51C. A 50:50 N_2:CO_2 "mixture" was injected through Coal A. Before that argon was flowed. This figure shows the axial, both radial, and volumetric strains and the upstream volumetric flow rate. Recall that a negative strain (change in dimension or volume divided by original dimension or volume) indicates expansion.

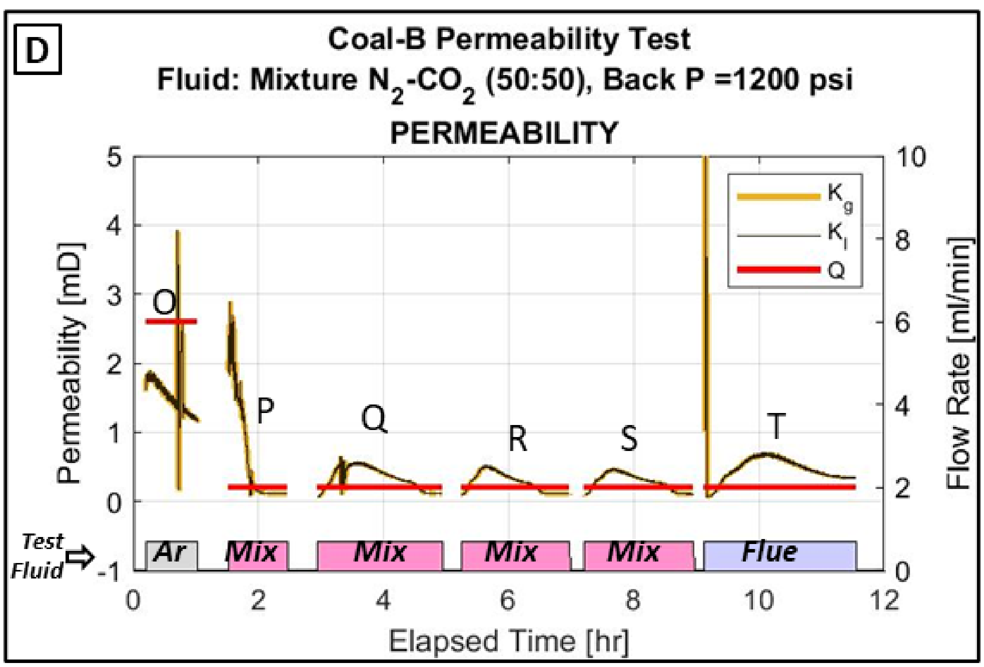

Figure 51D. A 50:50 N_2:CO_2 "mixture" was injected through Coal A. Before that argon was flowed. This figure shows the absolute permeability to the flowing gas and the upstream volumetric flow rate.

The subsequent batches of the 50:50 mix, events “Q”, “R” and “S”, presented a similar response. The strain record shows the ‘humped’ pattern caused by the desorption and adsorption cycles according to the CO_2:N_2 concentration from the supercritical stratification. The shapes of the strain curves for the 50:50 mix seem to be asymmetrical (shifted to the left, see Figure 51C), compared to the symmetrical pattern for the simulated flue gas (80:20). The higher CO_2 content produces earlier swelling. The maximum swelling was ε_V = -0.015 m^3/m^3. In the pressure record, there are two distinct periods.

1. In the first half of the 50:50 mix batch (N_2-dominated), both the upstream and downstream flowing pressures are close to each other, starting at ΔP ~10psi, but the differential pressure gradually increased.
2. When the second half of the batch (CO_2 dominated) reached the coal sample, the flowing downstream pressure (denoted as P_fd in Figure 51A, light blue, primary vertical axis) remains at 1200 psi, whereas the flowing upstream pressure (P_fu, dark blue, primary vertical axis) increased in response to the swelling produced by the CO_2, leading to a ΔP of 75 psi.

For every batch, the calculated permeability started at k_g ~0.9 mD but decreased to k_g ~ 0.2 mD by the end of each period.

Event “T” corresponds to the injection of simulated flue gas with an 80:20 composition, to evaluate the repeatability of the experiment. There was no evacuation or flushing with inert gas between the 50:50 mix and the simulated flue gas that would “reset” the stresses or adsorption conditions in the coal. The injected flue gas immediately produced the anticipated desorption attributable to the stratified fluids: Shrinkage -desorption- occurred for the N_2 dominated fluid, followed by swelling -adsorption- for the CO_2 dominated fluid in the batch. The profile of the strain hump is again symmetrical, but it finishes at a lower value ε_V = -0.012 m^3/m^3, due to the reduced concentration of CO_2 available in the flue gas batch.

XII.4.4 Cleat Closure

The reduction of permeability when injecting pure CO_2 remains one of the setbacks for potentially implementing sequestration projects in coal. The experiments performed with different mixtures of CO_2 and N_2 measured the volumetric expansion as an adsorption response. No swelling was observed when flowing Ar and N_2 since they are both inert gasses; the measured volumetric swelling (ε_V of 0.005 m^3/m^3) corresponds to a baseline for poroelastic effects when increasing the pore pressure is 1200 psi. Flooding with pure CO_2 demonstrated immediate swelling, with a maximum volumetric strain of ε_V = -0.028 m^3/m^3. Therefore, the swelling mechanisms are directly related to the adsorbed CO_2, or rather, the available CO_2 in the flow path in contact with the coal-related to the concept of partial pressure, based on the injection of stratified N_2:CO_2.

The flow experiments with the gases of N_2:CO_2 (80:20) "flue" and (50:50) "mixtures" provide an indication of the cleat closure, based on the assumption that the swelling of the coal reduces the width of the cleats, with the consequent drop in the permeability.

Figure 52 is a "close-up" of the strain and permeability responses for simulated flue gas (80:20) and mixed (50:50) gases, from events "L" and "S". These two selected periods occurred after flowing for ~7 hr in their respective experiments. The plots use equal scales in the vertical and horizontal axis for better comparison. In both experiments, the injection volumetric flow rate was Q = 2 mL/min, the backpressure was 1200 psi, and the fluids at the pump were pressurized to a supercritical condition before introduction into the flowline/sample (i.e., the pressure and composition were established in the piston of the pump).

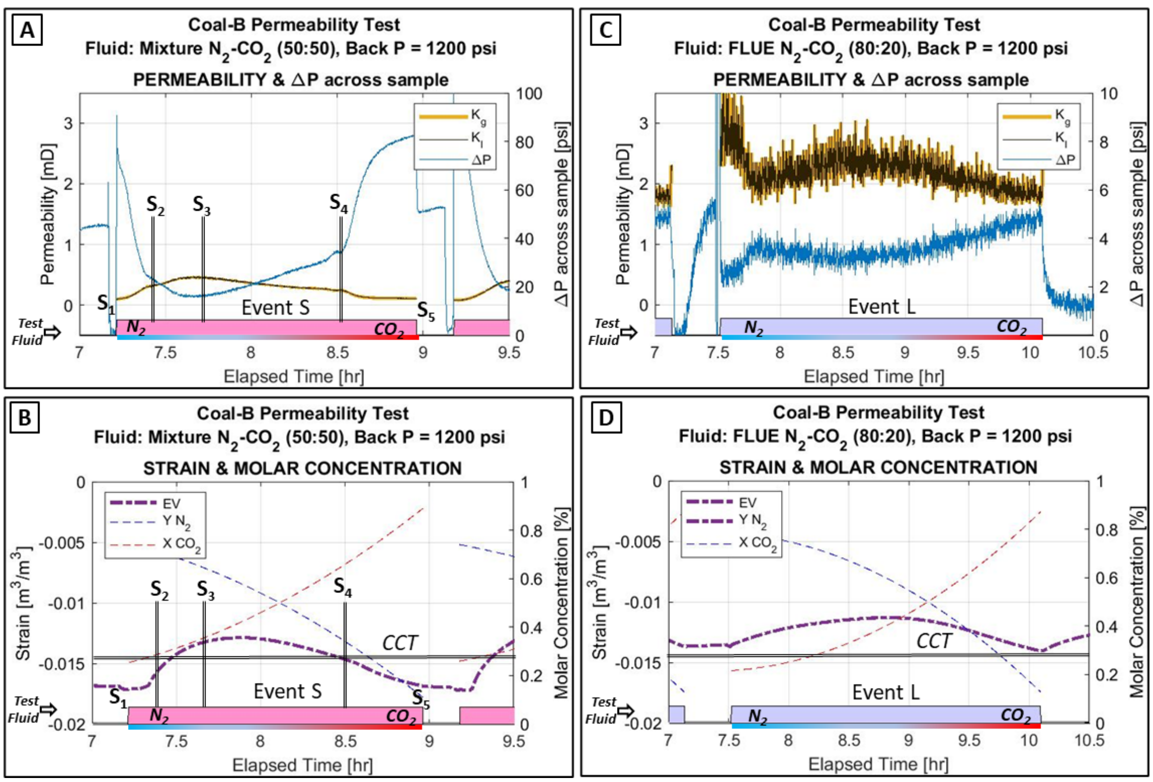

Figure 52.Strains and permeability as proxies for cleat closure.

The strain curves measure the cyclic desorption and adsorption as described previously, with a shift in the symmetry due to the gas stratification. The swelling for the flue gas (80:20) is consistently lower (ε_V=-0.0012 m^3/m^3) than for the mixed gas (50:50) (ε_V=-0.0015 m^3/m^3), because of the CO_2 available in the cleat and pore networks. The swelling is proportional to the adsorbed gas, hence to the storage capacity of the rock, at in-situ and flowing conditions.

Cleat closure is hypothesized to be represented by swelling observed during the cyclic responses during the mixture 50:50 flow tests. Figures 52A and 52B show the cycle elapsing from 7.2 to 9 hr (Event S from Figure 51), and it is a representative response of this phenomenon after two cycles of repetitive flow patterns. The ΔP curve in Figure 52A, which is the pressure differential across the sample, indicates a significant change in its pattern at two particular inflection points, labeled S_2 and S_4 (S_1 and S_5 are the beginning and end of the S cycle, respectively). S_1 reflects initial swollen conditions remaining from the previous injection cycle. From S_1 to S_2, an N_2-dominated mixture flows through the sample. The differential pressure decreases from 70 to 22 psi, whereas the volumetric strain (Figure 52B) shows a rapid shrinking of the coal. This shrinkage of the matrix material allows the cleat (natural fractures in the coal) apertures to increase as indicated by the increase of permeability. The interval from S_2 to S_4 is a period of continuous flow in a relatively high permeability corresponding to low differential pressure. However, as the concentration of CO_2 increases, a transition from a desorption condition (coal shrinking) to an adsorption environment (coal swelling) occurs in S_3. This is seen on the volumetric strain curve, which reaches a minimum shrinkage at the peak of ε_V at -.013 m_3/m_3. After S_3, the coal begins a swelling phase, with the ε_V curve on a negative slope.

In the period from S_4 to S_5, the differential pressure rapidly increases from 33 to 81 psi, indicating that the existing flow paths have been compromised by the coal swelling. The differential pressure and permeability in this period are comparable to the developed during CO_2 flooding (Figure 46) at 70 psi and 0.3 mD, respectively. The fluid viscosity remains practically unchanged at 0.026 cP (26 μPa·s), ruling out resistance to flow arising from mobility changes. By the end of the cycle, near S_5, the CO_2-dominant fluid maintains adsorptive and swelling conditions in the coal.

The key indicator for cleat closure occurs at S_4, at 8.5 hr. At this point, the volumetric strain reads $\varepsilon_V = -0.015\ m^3/m^3$. This strain value could be considered as the cleat closure threshold (CCT) at which the cleats in the coal will remain open. The multiple cycles performed with the 50:50 gas mixture (events Q, R, and S) indicate the same pattern in the differential pressure, ΔP, curve, rapidly increasing after a specific swelling of ε_V ranging from -0.013 to -0.015 m^3/m^3.

Furthermore, by using the same cleat closure threshold (CCT) for the flow experiment with the simulated flue gas (80:20 N_2 to CO_2) in the same Coal-B sample (Figures 52C and D: event L spanning from 7.5 to 10 hr) $\varepsilon_V = -0.015\ m^3/m^3$ is never exceeded; therefore the permeability remains higher at k_g >2 mD, rather than dropping to the 0.2 mD range which was experienced with swelling exceeding a certain threshold. The increasing ΔP curve indicates that the cleats are closing, but not to the extent of causing a pressure differential larger than 5 psi.

The measured cleat threshold is not unique or quantitative. The observations suggest that it does reflect a critical level of cleat closure where permeability will be significantly impaired by adsorption-related matrix swelling.

XII.4.5 Adsorption

The ultimate objective of this research is to optimize the transfer and storage of CO_2 in coalbed reservoirs. The Ferron coal has a high affinity for CO_2, being able to store large quantities of CO_2 by adsorption. However, the adsorption of pure CO_2 onto the coal causes drastic swelling of the bulk volume (the so-called matrix), reducing the aperture of the cleats and consequently reducing the permeability of the system. The injection of a surrogate flue gas suggested a methodology to overcome this loss of permeability. A remaining challenge was to estimate the amount of CO_2 potentially stored under flowing conditions.

CO_2 adsorption isotherms on the Ferron coal were performed by two independent laboratories (Lab-A: Schlumberger, Lab-B: Micromeritics) using a sister sample of Ferron coal from the same location as the samples used in the other experiments in this work program. Lab A followed preparation procedures established in ASTM D3173-73. This enabled testing at an equilibrium moisture content. The preparation by Lab B consisted of heating up to 110°C for 12 hr in a vacuum environment for degassing any remnant volatile components.

Note: For pressures larger than P_{CR}, the isotherm does not correlate with standard isotherm profiles and does not yield traditional Langmuir or BET parameters. Instead, for subcritical pressures, a polynomial regression of the adsorbed volume to the pressure is shown in Figure 53, with the resulting curve labeled 'ADS poly-fit', and the polynomial coefficients are reported in Table 11.

Table 11. Isotherm polynomial regression coefficients for CO_2 adsorption at 38°C - subcritical conditions

a_{Z4}	A_{Z3}	A_{Z2}	A_{Z1}	A_{Z0}
0.0302	-0.4509	1.1716	5.1446	0.3315

Figure 53 is for pure carbon dioxide. Various researchers have considered adsorption for mixed gases. Puri and Yee (1990) anticipated that the adsorption of mixed gases depended on the partial pressure of the constituents, rather than the overall fluid pressure. Therefore, the mass adsorption isotherms must be considered as a function of the amount of CO_2 present in the solution in the cleats and the matrix, leading to the partial pressure. The fluid stratification discussed earlier provides the molar composition of the fluid entering the sample at any given time. By integrating the molar composition with the pressure record during the flow experiments in the Ferron coal in

Figure 54, the calculated CO_2 partial pressure is used as a reference to estimate the adsorbed fluid when nitrogen and carbon dioxide are both present.

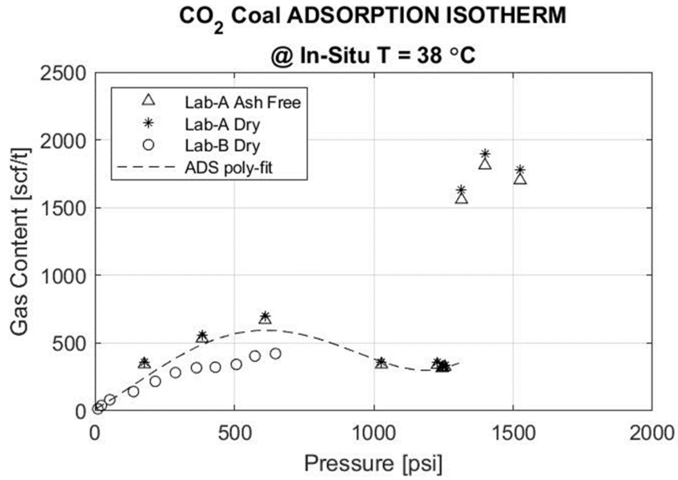

Figure 53. Adsorption Isotherms from independent laboratories in Ferron coal. Results are shown on a dry basis, on an ash-free basis, and on a dry, ash-free (daf) basis.

The inlet pressure record, combined with the molar composition at a given time, t, provides enough information to estimate the partial pressure of the CO_2 in the sample. As a reminder, the volume of the surrogate flue gas mixture during each cycle is 120 ml, pumped at 2 ml/min, over two hours of continuous pumping. The final adsorbed gas curve (secondary axis in Figure 54) results from the adsorption isotherms as a function of the partial pressure, instead of the total pressure, at a given time, t, leading to the 'humped' behavior for the adsorbed mass of CO_2, replicating the response of the volumetric strain measurements. *This observation corroborates the importance of cyclic phases of the fluid mixture, first dominated by the lighter and inert N_2, followed by the denser and chemically active CO_2, leading to the periodic desorption and adsorption processes.*

The CO_2 is adsorbed and the coal swells, reducing the cleat apertures and reducing the permeability; then, the CO_2 is partially desorbed as a more nitrogen-rich component is injected, restoring the strains and "self-healing" the permeability.

The average adsorption in each batch of synthetic flue gas mixture is 490 scf/ton. Utilizing flue gas with a composition of 80:20 CO_2:N_2 reduces the storage capacity to 77% of the maximum carbon dioxide storage capacity in these Ferron coal coals. That maximum storage capacity at 1200 psi was 636 scf/ton. Additionally, the transport capacity of the coal remains favorable (with a permeability of ~2.7 mD) avoiding the closure of the cleats that occurs when flooding with pure CO_2, where the permeability dropped to 0.2 mD.

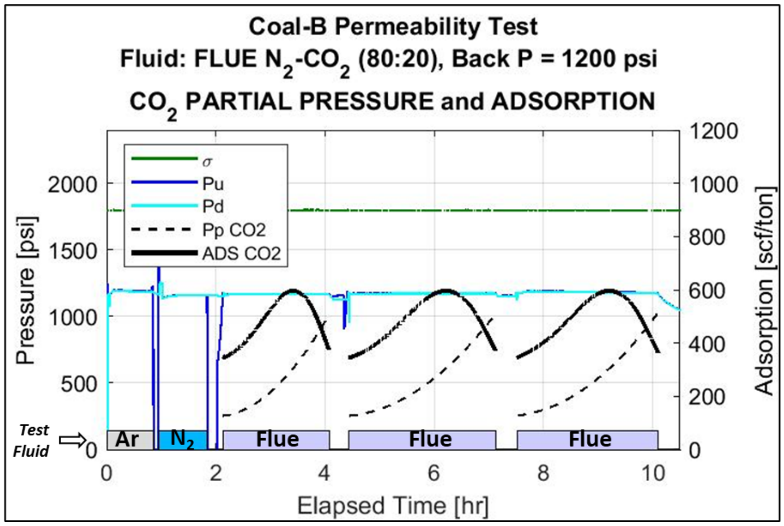

Figure 54. CO_2 partial pressure and the estimated carbon dioxide adsorption during flue gas experiments in a Ferron coal sample.

XII.4.6 Summary of Flow Measurements

The characterization of the Ferron coal and various fluids provided consistent data for evaluating the chemo-poroelastic flow properties of the system. CO_2 in either the highly conductive and relatively inert (to adsorption and volume change) Ferron sandstone or the fluid-sensitive Ferron coal demonstrates a lower pseudo-drained bulk modulus compared to N_2 and the flue gas mixture. This will be described further in a later section.

When mixtures of carbon dioxide and nitrogen were injected, the thermodynamic properties of the supercritical fluids promoted fluid segregation that suggests an enhanced flow method, reminiscent of WAG (Walter-Alternating-Gas), where the CO_2 reaches the storage sites within the coal. At the same time, the N_2 prevents the well-known issue of coal swelling and reduction in permeability, while maintaining some storage capacity.

Using flue gas injection as a method of enhanced coalbed methane recovery and carbon dioxide sequestration could provide a major advantage by reducing the cost of surface equipment for CO_2 extraction via amine plants (or similar). However, some impurities from the flue gas must be removed to eliminate competitive adsorption effects, as reported by other authors (Hefti & Mazzotti, 2018; Ottiger et al., 2008).

XII.4.7 Future Work

From a scientific perspective, future work could include.

Developing an accurate thermodynamical model to determine the concentration profile

- Elaborate on the concepts of Grashof number and vapor-liquid equilibrium to confirm that stratification might be manipulated at an industrial scale, and to evaluate whether it is inhibited by miscibility
- Consider stratification further by incorporating temperature gradients that would be observed in an actual well during injection (increasing with depth and likely decreasing with injection time)
- Apply concepts of flue gas stratification to commercial reservoir modeling platforms

Bench-scale experimental work for realistic field configurations:

- Evaluate the vertical fluid stratification while convective flow occurs horizontally as fluid moves through a subhorizontal reservoir, possibly in a horizontal well
- Flue gas mixture alternating with water flooding (WAG). Slugs of water are often injected during conventional carbon dioxide enhanced oil recovery to improve the distribution of the flow aerially and spatially through a reservoir (conformance)
- Fluid transport considering coal interfingering with sandstone. This is a unique geologic feature where the sands may significantly improve injection performance by allowing injection to bypass swollen low permeability localities.
- Modify the laboratory apparatus for measuring additional parameters in real-time, including improved density measurements, in line CO_2 molar composition (infrared), and recording (automatically rather than manually) the volume displaced in the pumps (confining and flowing volumes).

XII.5 Experimental Evaluation of Bulk Moduli

XII.5.1 Test Description

The ultimate objective of this test was to characterize the bulk modulus (K) of each of the lithotypes in the coal system (Mancos shale, MBG-Sh; Ferron sandstone, F-SS; and Ferron (or Emery) coal, F-Coal) when flooded with three types of fluid (N_2, simulated flue gas, CO_2 and under vacuum). The choice of measuring K of the samples is based on the instrument configuration, where the simulated in-situ stress σ is applied evenly around the sample (the confining pressure). Recall that the bulk modulus is indicative of how much volumetric strain (and indirectly deformation) a sample will experience as the effective stress changes. Recall further that the effective stress changes as the pore pressure is changed. Note also that there is supplementary deformation associated with chemisorption. Results from the tests are compiled in Appendix B. Some representative data are described in the text.

Average/representative in-situ conditions for some parts of the reservoir are a formation or pore pressure P_p = 1200 psi and a Terzaghi effective total stress σ = 1800 psi, calculated from the average of the principal stresses at a depth of 2500 ft, according to Andersonian fault types for a normal faulting stress distribution ($\sigma_V > \sigma_H > \sigma_h$)[41]. The pressure setting is also consistent with the maximum allowable working pressure of the flowline components used in the laboratory experiments, MAWP = 2500 psi. In a field setting (see earlier discussion for simulations), the bottomhole injection pressure would be maintained at less than the minimum total horizontal stress, σ_h, to avoid hydraulic fracturing.

The bulk modulus assessment consisted of gradually increasing the applied stress σ (confining pressure increased at a constant pump rate) from an initial value σ_o to the largest in situ stress used in the experiment, σ_f = 1800 psi (consider this as the loading period). This was followed by a reduction in the confining pressure (a surrogate for average total in-situ stress conditions) back to σ_o (consider this as the unloading period). The experiment was performed at increasing and decreasing flowline pressures to evaluate the difference between loading and unloading cycles - anticipating hysteresis, the consequences of variations in the Terzaghi effective stress, and the effect of fluid type at different pore pressures. Each cycle was repeated twice to assess consistency.

Table 12 summarizes the tests performed, indicating the different pore pressure and the initial and final values of the confining pressure for every cycle of loading, and unloading. The initial confining pressure, σ_o, was maintained at 100 psi above the pore pressure value to avoid rupturing the jacketing sleeve (i.e., the confining pressure must always exceed the pore pressure). The table shows:

- Test – A designation of an individual test where a loading/unloading cycle is applied.
- Fluid – The fluid injected into the sample during a specific test.
- Pore Pressure – The fluid pressure was maintained in the sample (the back pressure regulator was set to this value).
- σ_o – The confining pressure at the start and the end of the loading-unloading cycle.
- σ_f – The confining pressure at the peak of the loading-unloading cycle.

XII.5.2 Calibration: Aluminum

A test calibration/validation was performed by using an aluminum billet of the same dimensions (1.5" diameter by 3" long) as the rock plugs. Figure 55 shows the strains and confining pressure (no fluid pressure) measured when this aluminum sample was loaded. The pressure transducers and strain gauged cantilevers had been independently

[41]Note the designation of the subscripts for the stresses. “V” indicates stress acting in a vertical direction, largely related to the weight of overlying material. “H” indicates the value of the largest horizontally acting total stress. “h” analogously indicates an orthogonal stress, acting in a horizontal direction which has the smallest value of any stress acting in the horizontal plane.

calibrated. The slope of a plot of effective stress[42] versus volumetric strain was 9.8 x 10^6 psi, corresponding to the published bulk modulus for this grade of aluminum in the literature, validating the setup and the process.

Table 12. Bulk modulus analysis.

Test	Fluid	Pore Pressure (psig)	σ_o (psi)	σ_f (psi)
1	Vacuum	-10	100	1800
2	N_2	0 (atm)	100	1800
3		500	600	1800
4		1200	1300	1800
5	N_2/CO_2 blend	0 (atm)	100	1800
6		500	600	1800
7		1200	1300	1800
8	CO_2	0 (Atm)	100	1800
9		500	600	1800
10		1200	1300	1800

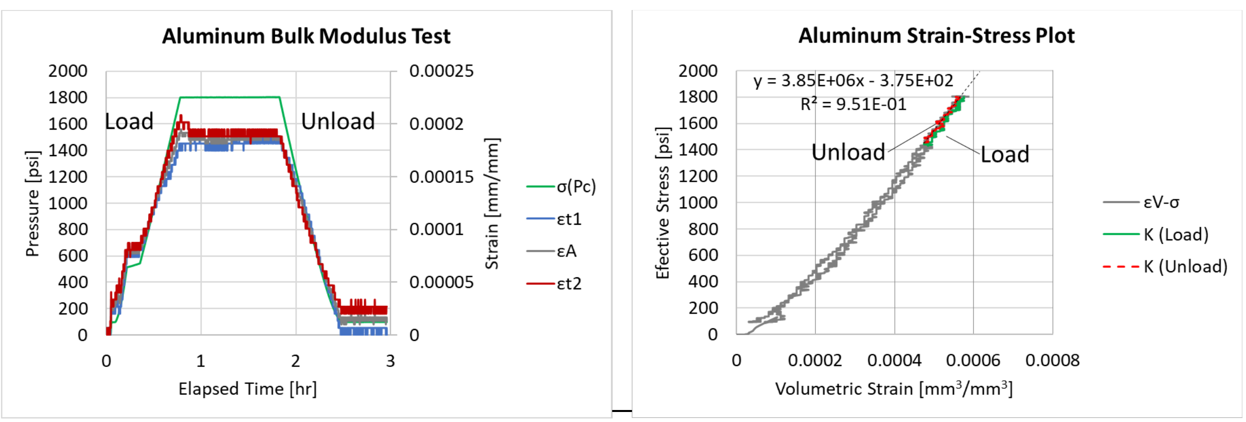

Figure 55. Bulk modulus measurements on an aluminum calibration sample. The panel at the left shows pressure and strain increases with time and the plot at the right shows stress versus strain. The axial cantilever may have malfunctioned, and the axial strain was taken as the average of the two radial strains.

XII.5.3 Coal Bulk Modulus Analysis

This section describes the bulk modulus analysis in the Ferron coal sample.

[42] In this case, the effective and total stresses are equal because the pore pressure is zero.

XII.5.3.1 Evacuated Coal Bulk Modulus Analysis

The bulk modulus measurements with an evacuated Ferron coal evaluated mechanical response with nominally no fluids present. There were two loading-unloading cycles in the applied stress σ (confining pressure) from 100 to 1800 psi to 100 psi at 6 ml/min (refer to Figure 56).

- For the first cycle, A, confining pressure was applied and held at a maximum value of 1800 psi for 10 minutes, aiming to compress the sample and accommodate deformation of internal rock features.
- The second cycle, B, was completed with no waiting between the loading and unloading stages.

The stress-strain curves mostly overlaid each other and followed an anticipated behavior: smaller stress vs. strain slope for low effective stress and a steeper curve for larger effective confining pressure, σ'. The stabilized slope for the initial loading cycle A (bulk modulus) is 2.68 x 10^5 psi, which is slightly lower than the second loading period (2.90 x 10^5 psi). The estimated bulk modulus determined from the slope of both unloading cycles is nearly identical 3.50 x 10^5 psi and 3.59 x 10^5 psi, respectively. As is expected, the unloading modulus is larger than the loading modulus.

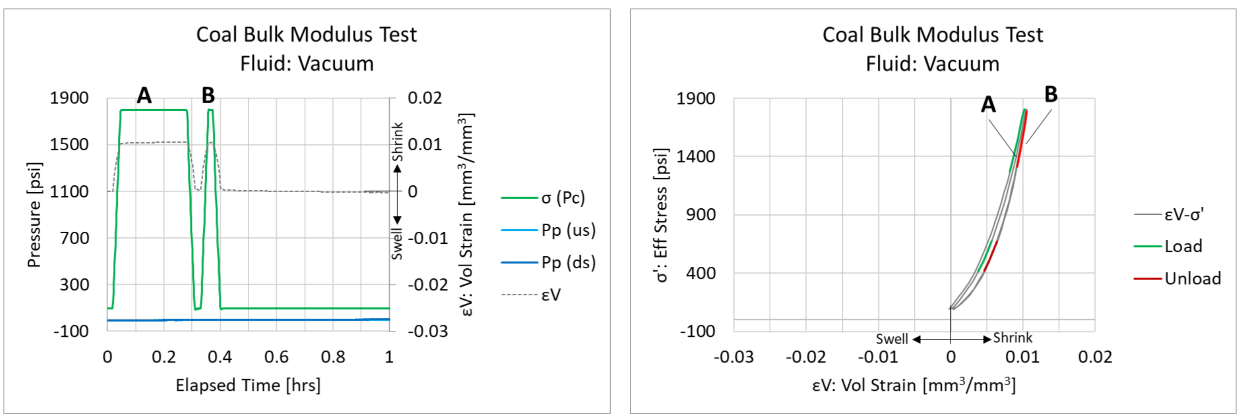

Figure 56. Bulk modulus experiments on evacuated Ferron coal. At left, confining pressure, pore pressure, and volumetric strain are plotted against time. At right, the effective mean stress is shown versus volumetric strain.

XII.5.3.2 Coal with Nitrogen (N_2)

Coal flooded with N_2 is not expected to have considerable chemical potential, hence no intermolecular interactions of adsorption. The experimental sequence of events from A to F (Figure 57) generated a stress-strain plot (like that for the Ferron sandstone, described subsequently) where each loading and unloading cycle overlaid each other, with only compressive deformation observed. The maximum strain for the coal at event F is ε = 0.0099 mm^3/mm^3.

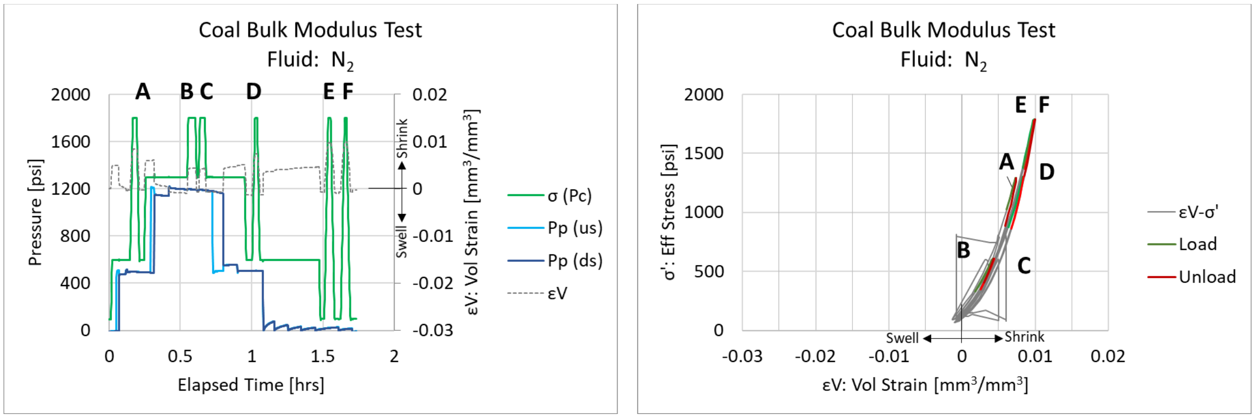

Figure 57. Bulk modulus experiments: Ferron coal flooded with N_2. At left, confining pressure, pore pressure, and volumetric strain are plotted against time. At the right, effective mean stress is plotted against volumetric strain.

XII.5.3.3 Coal with CO_2

The ultimate objective of this project is to evaluate the storage of CO_2 in coal. The adsorption of CO_2 onto the coal matrix produces swelling. This test was carried out for 60 hr to accurately record chemo-poroelastic response to every change in pore pressure or applied stress with an adsorptive pore fluid. The record can be described by two different periods; the first period includes events A, B, and C and experienced the swelling process, and the second period encompasses the chemo-poroelastic recovery back to original conditions, from events C to E. The response is illustrated in Figure 58.

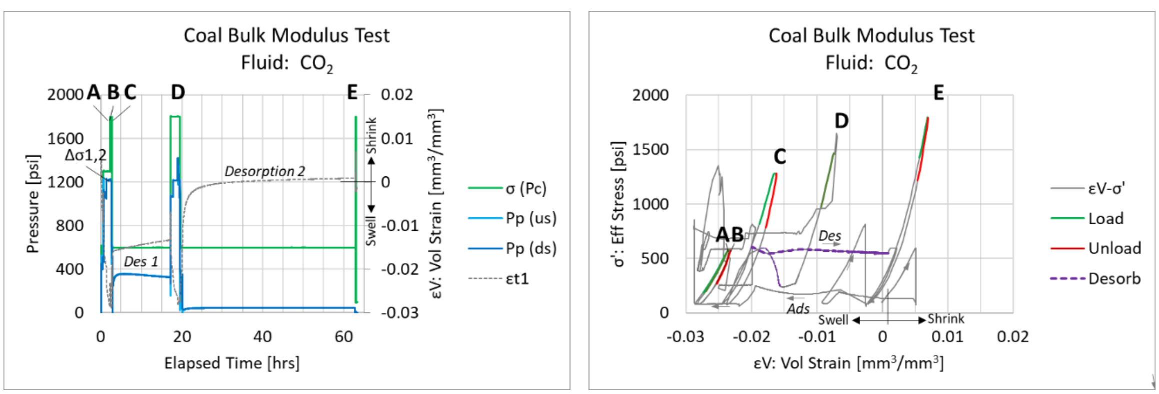

Figure 58. Bulk modulus experiments: Coal flooded with CO_2.

XII.5.3.4 Coal with CO_2 Flooding: Swelling Period

Swelling is immediately observed during the initial flooding of CO_2 - within the first 4 hr of the test (Figure 59). The test starts with a vacuum applied to the sample and the flowline, and the in-situ pressure σ is increased from zero to 600 psi. This event is labeled as "Δσ-1" in Figure 59. This increase in the confining pressure compresses the sample with a volumetric strain ε_V of 0.005 mm^3/mm^3, causing a positive spike in the time record and a positive slope in the σ'-ε_V curve. Shortly after this “event”, the sample is flooded with CO_2 to 500 psi and the system is closed to let the pressure stabilize within the sample. The presence of CO_2 during this period, from 0.02 to 0.5 hr, causes an immediate swelling of the coal as evidenced by a decrease in the volumetric strain from +0.005 to approximately -0.008 mm^3/mm^3. The pore pressure in this interval decreased down to 400 psi in compensation for the change in volume and the adsorption that occurred.

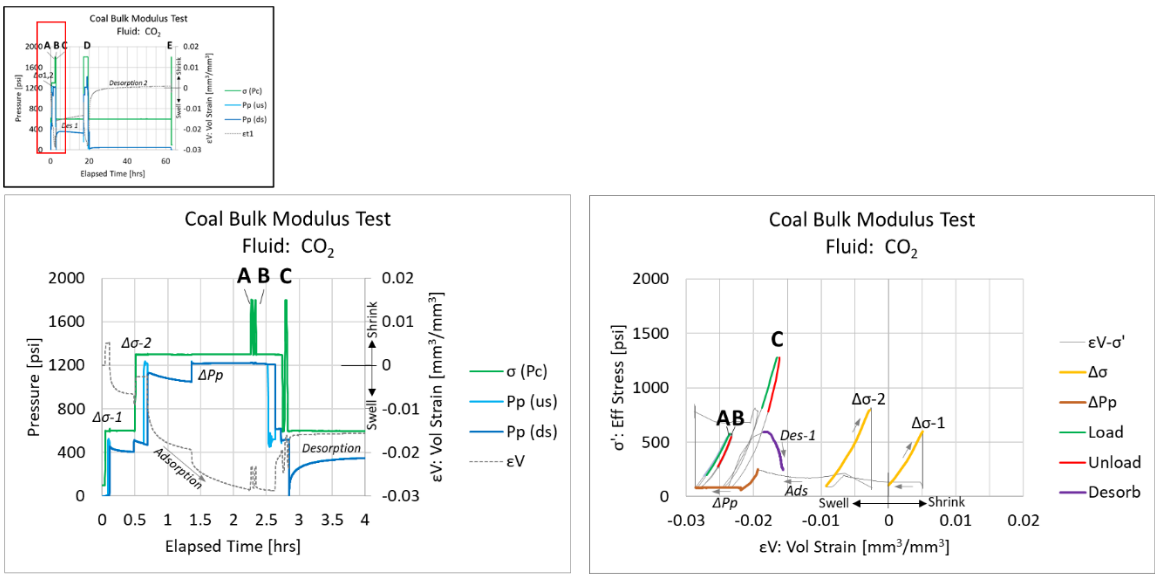

Figure 59. Bulk modulus experiment with coal flooded with CO_2. The two lower figures denote a swelling period. The inset is a replica of Figure 58, showing the entire test.

The second compression, “Δσ-2”, occurs at t = 0.5 hr and is demarcated by increasing the confining pressure to 1300 psi, with a slight compression. At 0.7 hr, the pore pressure was increased from 400 to 1200 psi, causing a second period of swelling until 1.4 hr. The increase in volume reaches a strain of approximately -0.019 mm^3/mm^3, with the pressure decreasing to 1048 psi.

At t=1.4, an event labeled as “ΔPp”, describes where the sample was internally pressurized to a constant pore pressure of 1200 psi for 1 hr (downstream valve was closed). The maximum volumetric strain observed was about 0.028 mm^3/mm^3. At t = 2.4 hr, the pumping was terminated.

Events A and B are the loading and unloading cycles where the confining pressure σ was varied from 1300 to 1800 psi and back to 1300 psi, producing similar slopes in the ε_V-σ' plot (local values of the bulk modulus).

At t=2.5 hr, the pore pressure was reduced to 600 psi, which caused the sample to shrink to a volumetric strain of approximately -0.02 mm^3/mm^3. Loading cycle C involved increasing the confining pressure from 600 to 1800 psi.

XII.5.3.6 Coal with CO_2 Flooding: Desorption Period

The desorption process started at an elapsed time of 2.8 hr. With the total in-situ stress (i.e., the confining pressure) maintained at 600 psi, the flowline pressure was instantaneously vented to the atmosphere, allowing the CO_2 to degas from the sample. In the time elapsed between events C and D (over 13 hr, Figure 58), compressive strain (dashed gray curve, secondary axis) increased while the pore pressure decreased.

Desorption of the CO_2 from the coal after "returning to" atmospheric pressure is evaluated from period C to period E (for 40 hr). Refer to Figure 60. The pore pressure was brought down to atmospheric, and the desorbing carbon dioxide was vented. The confining pressure was reduced to 500 psi. The amount of residual carbon dioxide in the sample was unknown. The sample was valved in. The pore pressure increased to 45 psi and the effective stress remained stable at σ' = 450 psi, while the strain gradually decreased back to nearly zero, initial conditions for the sample.

During the final event (E), the confining pressure was increased from 100 to 1800 psi. Since a significant amount of the CO_2 had likely been desorbed and the sample had been returned to initial stress conditions, the sample underwent an actual compression as observed with the positive strain values.

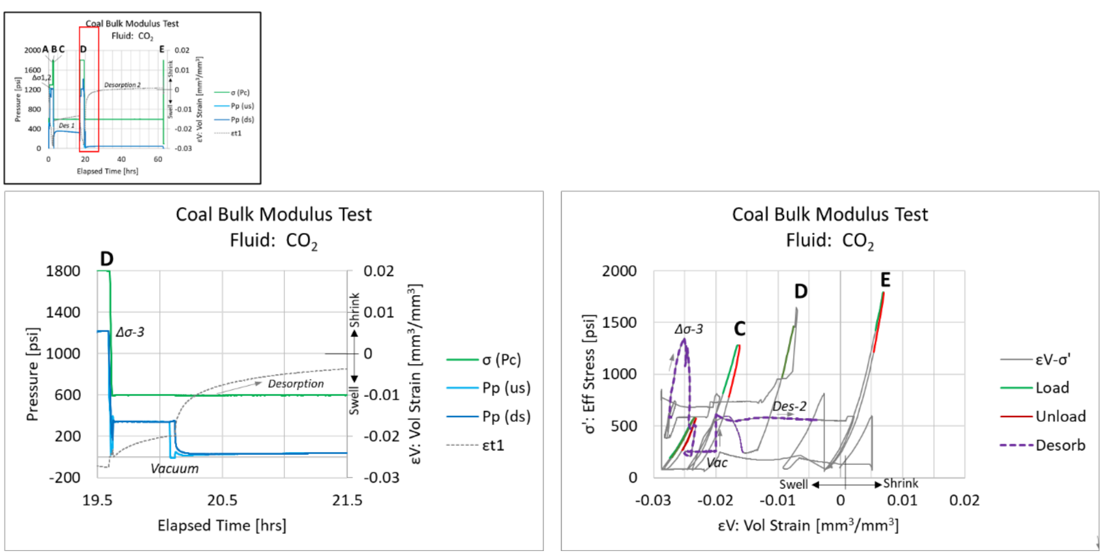

Figure 60. Bulk modulus experiment for coal flooded with CO_2. This shows what has been designated as the desorption period. The inset is a replica of Figure 58, showing the entire experimental chronology.

The desorption process is observed in a similar experiment, recorded in a video clip https://youtu.be/mn3B1LG0p5k (Vega-Ortiz & McLennan, 2021). After flooding the coal with CO_2 up to 1600 psi, the sample was taken out of the pressure chamber and exposed to atmospheric conditions. It was sprayed with a soapy water solution. The desorption of the CO_2 occurs mostly through the cleats and fractures, evidenced by the stream of bubbles of soapy water. Also, small bubbles burst randomly in the coal bulk matrix indicating the location of microfractures conducting the CO_2.

XII.5.3.7 Coal with Surrogate Flue gas (N_2:CO_2 80:20)

The coal sample, when flooded with a gas mixture (Figure 61), produced a combined response of shrinking and swelling dominated by the adsorption of the CO_2 fraction. The adsorption depends on the pore pressure. The maximum swelling $\varepsilon_{V\text{-flue}}$=-0.0029 mm^3/mm^3 occurs at the beginning of events B and C, where the pore pressure is 1200 psi. Compared to the maximum swelling with pure CO_2 in a Ferron coal, the measured volumetric strain is reduced by 90% or thereabouts. **There is significantly less swelling when a flue gas proxy is injected.**

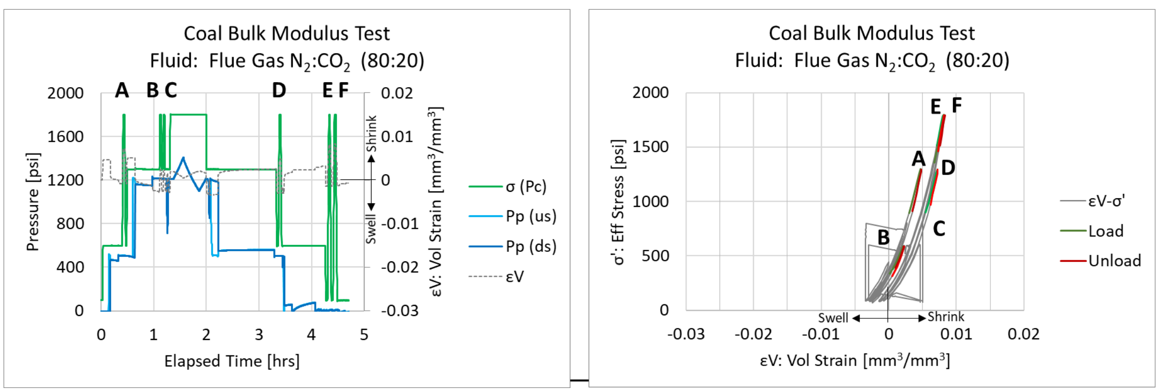

Figure 61 Bulk modulus test: Coal flooded with flue gas proxy (N_2:CO_2, 80:20).

XII.5.4 Sandstone with CO_2 as the Pore Fluid

The Ferron sandstone is interfingered with the Ferron coal seams and might serve as a high permeability pathway. The constituent minerals (largely SiO_2) are nominally chemically inert to CO_2 and no interaction between solids and liquids is expected (there is no carbonate and less than 10% illite and kaolinite). Events A through F (Figure 62) follow the same sequence as for when nitrogen is injected. However, the sandstone sample saturated with CO_2 showed a progressive volumetric reduction from cycle to cycle. In Figure 62, this is noticeable in the strain offset between events A and D. Superficially, one cannot readily determine if this is phenomenological or methodological. However, this compression is likely caused by the thermodynamic properties of the CO_2, which is transitioning from a gaseous to a supercritical phase, reducing its volume and increasing the density in the process. In the time record between events A and B, the pore pressure decreases slightly from 1200 psi (blue curve, primary vertical axis), while the strain curve (dashed gray, secondary vertical axis) has a positive slope. As the fluid compressed, the rock matrix reduced in size as the pore network accommodated the shrinking fluid volume.

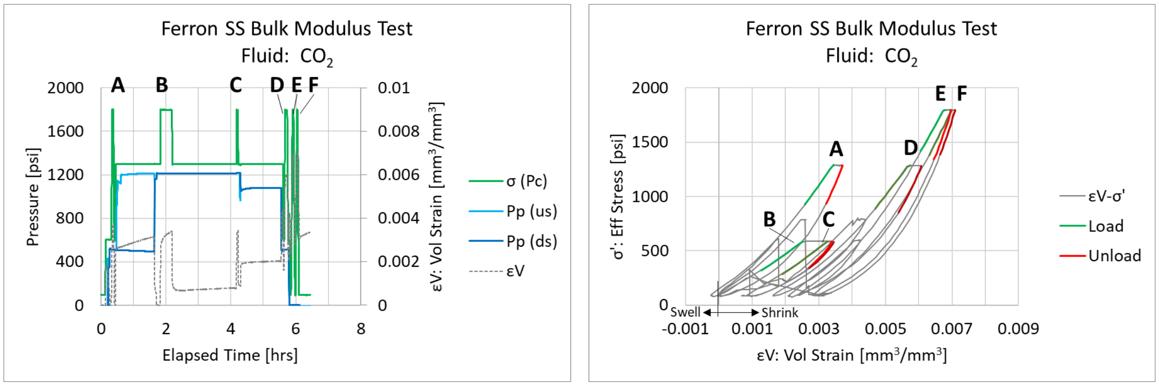

Figure 62. Bulk modulus experiments: Sandstone flooded with CO_2. At left is the experimental chronology. At the right is the progressive reduction in sample size associated with phase change from gaseous to supercritical.

XII.5.5 Shale with CO_2

As a reminder, the mineral composition of the Mancos shale that was evaluated is 30.7 wt.% carbonate, 58.3 wt.% silicates, and 11 wt.% of clays (illite and kaolinite).

The sample was initially confined with a surrogate in situ stress of 1300 psi, while maintaining the sample evacuated, (event Δσ in Figure 63). The application of the confining pressure caused the sample to shrink by a volumetric strain of 0.0015 mm^3/mm^3. Upon flooding the sample with CO_2 to a pressure of 1200 psi, event ΔPp, the shale sample swelled to -0.0022 mm^3/mm^3. Events A and B are loading and unloading cycles of the swollen sample, although the slopes in the ε_V-σ' plot develop with a positive magnitude. Decreasing the pore pressure to atmospheric pressure during the period from 0.8 to 1.0 hr returns the volumetric strain to the initial compressed state at 0.0014 mm^3/mm^3. Loading cycle C occurs with the CO_2 already degassed.

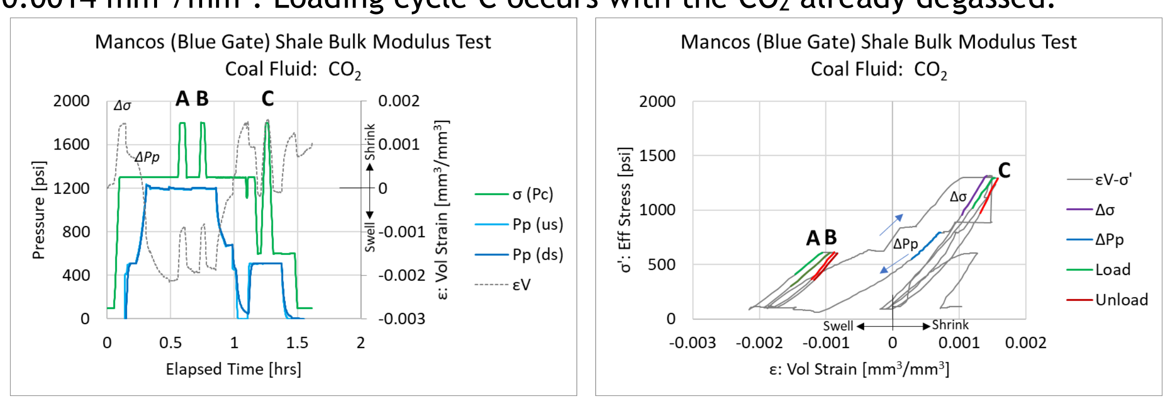

Figure 63 Bulk modulus experiment where a Mancos Shale sample was flooded with CO_2.

XII.5.6 Variation of Modulus by Lithotype at In-Situ Conditions

Figure 64 is a summary of the bulk moduli determined from the experiments at anticipated, representative, virgin in situ conditions in a Buzzard Bench ECBM scenario ($P_p = 1200$ psi, $\sigma = 1800$ psi) for loading (solid bars) and unloading cycles (dashed bars). The calculated bulk modulus under vacuum represents the resistance to compression of the rock matrix, with no other fluid occupying the pore spaces, hence showing larger magnitudes – truly drained behavior.

For the cases where the sample was flooded with different fluids, the moduli are consistently lower when the sample is filled with CO_2 – in comparison to N_2 and the simulated flue gas. This reduction of the bulk modulus is reported by (Delle Piane and Sarout, 2016). The moduli in the experiments characterize the contribution of both rock and fluids. Hence, the compressibility and sorption of the supercritical carbon dioxide (and the nitrogen) play a fundamental role in reducing the resistance to compression at downhole conditions.

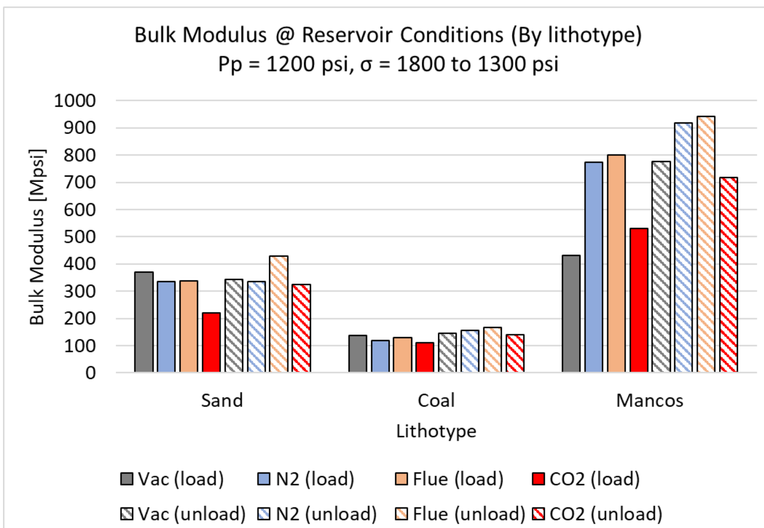

Figure 64. Moduli for the reservoir (coal), the interfingered sand, and the bounding material (Mancos shale) in the Buzzard Bench field, grouped by lithology.

An analysis of the feasibility of an ECBM project considers the reservoir system, including the storage rock (coal), the secondary storage and fluid transport network (interfingered sand), and the caprock (Mancos shale). Figure 65 is an alternative presentation of Figure 64 and indicates the moduli sub-grouped by fluids, assuming the injection of a single fluid type. The Mancos shale (MBG-Sh) is consistently higher, up to twice (or three times for the case of flooded with CO_2) than the Ferron sandstone (F-SS) or the Ferron coal. The mechanical integrity of the seal rock is one of the most important features for long-term sequestration or effective storage.

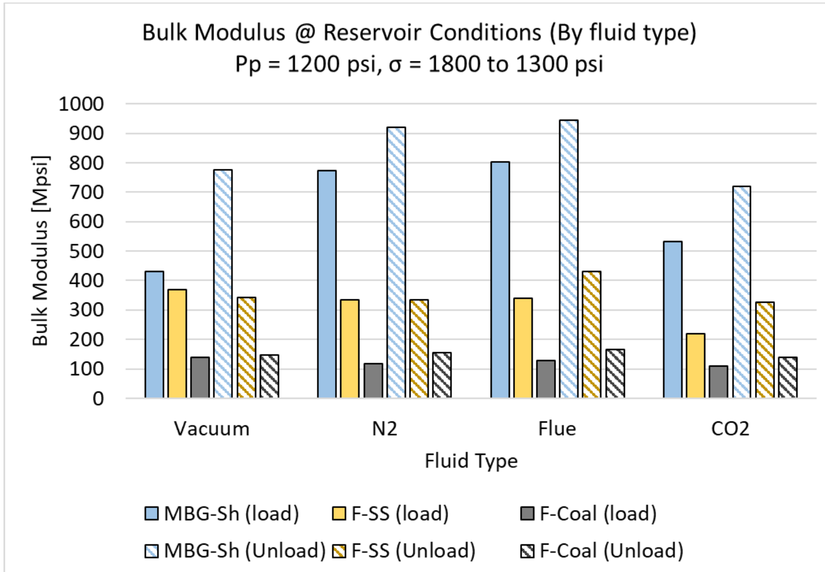

Figure 65. Moduli for the reservoir and bounding material in the Buzzard Bench field, grouped by saturating fluid.

XII.5.7 Bulk Modulus Prediction

Having characterized the entire set of rocks and fluids, repeatability was seen in the variations of modulus with effective stress. The stress-strain curves follow the same nominal pattern for every loading or unloading process if effective stress is considered. The shrinking or swelling due to the sorption of CO_2 shifts the strain. The prediction of the stress-strain behavior for in-situ conditions (σ = 1800 psi, P_p = 1200 psi, carbon dioxide at supercritical conditions) requires the "normalization" of the resulting curves from each experiment by eliminating the offset in the strain, initiating every response from $\varepsilon_V = 0$ mm^3/mm^3. The curves are fitted to an exponential function.

$$\sigma' = A\, e^{B\varepsilon_V} \tag{14}$$

where σ' is the Terzaghi effective stress, ε_V is the volumetric strain (mm^3/mm^3), and A (psi) and B are the resulting fitting parameters.

Figure 66 summarizes the measured stress-strain curves for each of the lithologies that are present. The solid lines with steeper slopes correspond to the Mancos Blue Gate shale (MBG-Sh) caprock. The dashed-dotted curves are the results from the Ferron Sandstone(F-SS), and the dashed lines with lower slopes are the measured response in the coal. The color identifies the fluid type: red for CO_2, blue for N_2, gray for vacuum, and orange for the flue gas surrogate mixture.

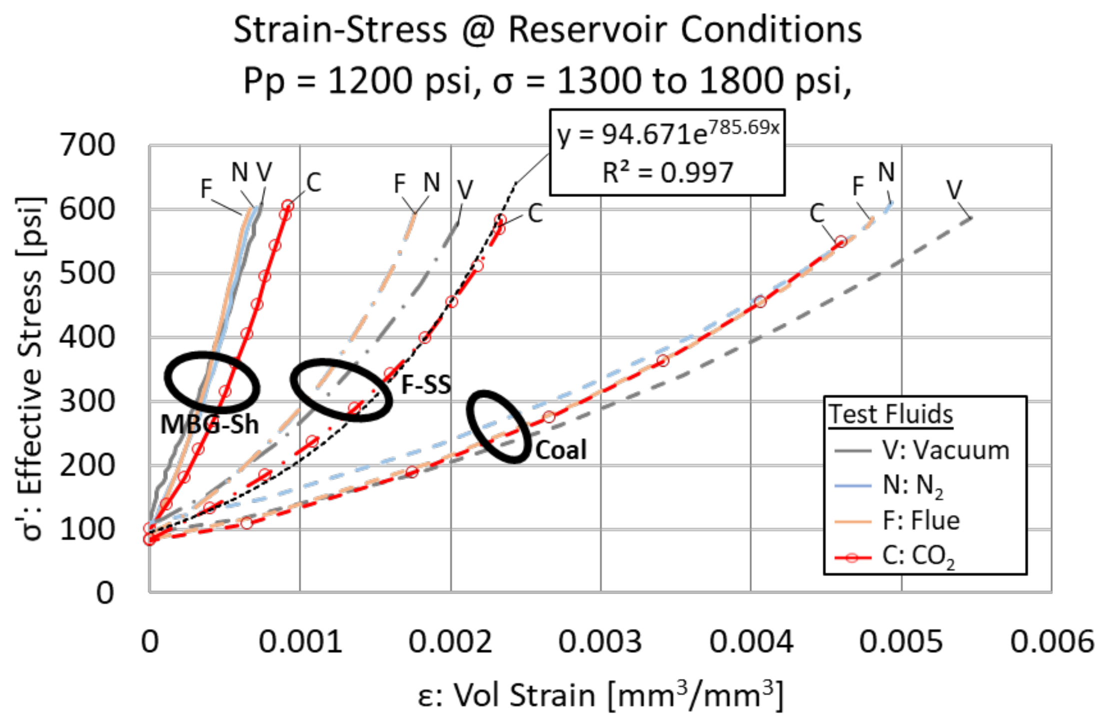

Figure 66. Summary of the experimental stress-strain curves at in situ conditions for the different lithotypes (shale, sandstone, and coal). The displayed equation is the resulting trendline calculation for the sandstone-flue gas combination. The slope gives a tangent bulk modulus.

Table 14 summarizes the coefficients A and B and the coefficient of determination, R^2, for each of the rock-fluid combinations using the exponential fit suggested in equation (14). These approximations are useful for numerical modeling of gaseous injection where coupled chemo-poroelastic mechanisms, in both the reservoir and the seal, play a role in the design of the field. Another application for these data is the monitoring of CO_2 flooding by using seismic techniques. The transit times for the formation change according to the chemo-poroelastic properties; a proper characterization of the fluid contained in the reservoir determines the appropriate velocity for the interpretation of seismic attributes.

XII.6 Key Observations:

- Regardless of the lithotype the undrained bulk modulus of any sample flooded with CO_2 is consistently lower compared to the other fluids.
- Flooding unsaturated coal with CO_2 produces the lowest bulk modulus, but once the sample is saturated (adsorption plus pore/cleat network) and the CO_2 has transitioned to the supercritical phase, it behaves similarly to the other fluids (N_2 and simulated flue gas).

- The flue gas behaves similarly to N_2 alone. The CO_2 in the mixture does not have a significant impact on the poroelastic properties. This is because this is an undrained test, and the volume of carbon dioxide is reduced when flue gas is injected.
- The curves can be modeled by using an exponential trendline $y=Ae^{Bx}$. This could be useful for numerical modeling and estimation of transit times for seismic interpretation. The bulk moduli change depending on the fluid present in the rock.

Table 14. The exponential fit of the strain-stress curves.

Lithotype	Fluid	Bulk Modulus Coefficients		
		A	B	R^2
Mancos Shale	Vacuum	133.6	2264	0.9674
	N_2	117.4	2508	0.9837
	Flue	110.4	2755	0.9786
	CO_2	115.1	1868	0.9893
Ferron Sand	Vacuum	113.6	817	0.9968
	N_2	98.4	1034	0.9981
	Flue	97.9	1035	0.9983
	CO_2	94.7	786	0.9970
Ferron Coal	Vacuum	98.3	339	0.9921
	N_2	114.3	343	0.9979
	Flue	90.9	393	0.9948
	CO_2	84.9	418	0.9945

XIV. Permanent Sequestration:

How can CO_2 be more effectively sequestered permanently in coal seams? As described CO_2 adsorbs to coal. N_2 is less adsorptive – less adsorptive than methane – some estimates suggest less so by one-half. Figure 67 (Reeves et al., 2003) supports this for a San Juan basin coal. What does the figure show? Carbon dioxide can displace methane and be stored. If there are adequate seals, an equilibrium adsorbed gas content will exist at any pressure. The gas can still be remobilized by desorption, but the reservoir pressure must be intentionally reduced substantially.

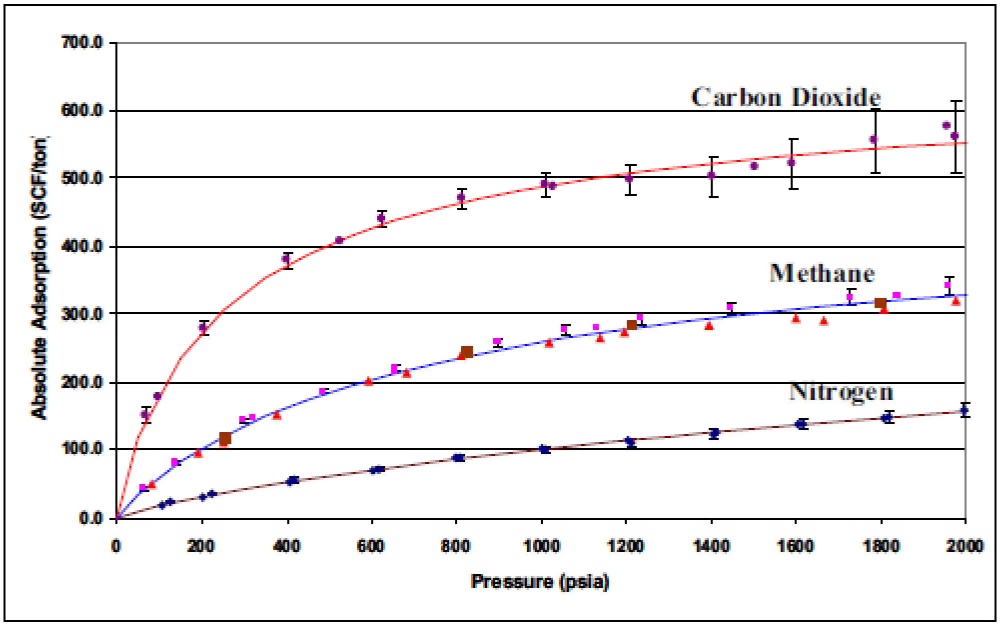

Figure 67. Laboratory sorption isotherms for CO_2, CH_4, and N_2 on San Juan basin coal (after Reeves et al., 2003). CO_2 has a higher affinity to coal than methane and much higher than nitrogen as was demonstrated in the experiments in Section XII.

The figure summarizes the essence of sorptive sequestration and touches on the implications of injecting something like processed flue gas with a mixture of carbon dioxide and nitrogen.

- Start with methane, naturally present in coal. The curve (labeled methane in Figure 67) shows that at a reservoir pressure of about 1500 psi, approximately 300 scf/ton of methane could be stored (this figure is for a San Juan Basin coal, slightly more adsorptive than the Ferron coal). Depending on the geologic history, this is the anticipated maximum amount of methane that is present in situ.
- Consider what happens if CO_2 is injected. The amount of carbon dioxide that can be stored is much higher than methane. As the coal is exposed to carbon dioxide, the adsorbed native methane (residual amounts of methane are still present even if production has been occurring before this time) is desorbed and the carbon dioxide adsorbs into the coal in its place. Isotherms performed on the Ferron coal at reservoir temperature showed a significantly greater CO_2 adsorptive capacity.
- What happens with nitrogen? As can be seen in the example in Figure 67, there is much less affinity for nitrogen in coal. At an inferred reservoir pressure of 1500 psi, maybe 130 scf/ton are adsorbed for the San Juan coal that is shown. This is much less than carbon dioxide. What happens when nitrogen flows through the reservoir? Adsorbed methane (or CO_2 if present) is (could be) produced. The

reason is that the pressure that matters is partial pressure. If nitrogen flows, the partial pressure of methane or carbon dioxide in that flow stream is low(er) and desorption can occur. This is how nitrogen flooding for methane recovery works, and why nitrogen breakthrough at the producer can be relatively fast.

- Imagine pumping a sanitized flue gas – i.e., hydrogen sulfide is removed and ideally oxygen and water giving, for example, a hypothetical blend of carbon dioxide and nitrogen. CO_2 will adsorb and maybe a little nitrogen but reduced partial pressure of carbon dioxide may temper the adsorption and swelling will be reduced, keeping more carbon dioxide in the flow stream, and moving it deeper into the reservoir.
- What happens if discrete slugs of carbon dioxide and nitrogen are pumped? The swelling might be mediated. When permeability to CO_2 is reduced, a nitrogen slug could recapture some of it and move it deeper into the formation.

The same phenomena are demonstrated for Ferron coal. Figure 68 is a methane isotherm performed on Ferron coal at 38°C. This figure shows as-expected methane adsorption. At an in-situ pressure of about 1500 psi (as used in the simulations) the adsorptive capacity is approximately 260± scf/ton (of methane). Alternatively, Figure 69 is an isotherm performed with carbon dioxide at 38°C. While there are some peculiar characteristics, the indications are that much more carbon dioxide will be adsorbed of carbon dioxide suggesting that the simulations could be quite conservative.

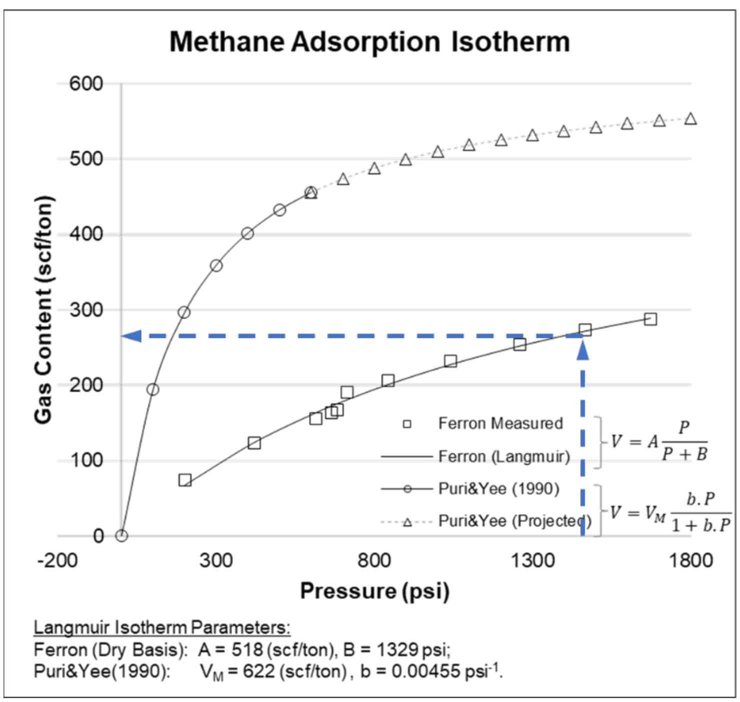

Figure 68. Methane adsorption on Ferron coal at 38°C. Measured methane adsorption at 1500 psi in situ pressure is shown.

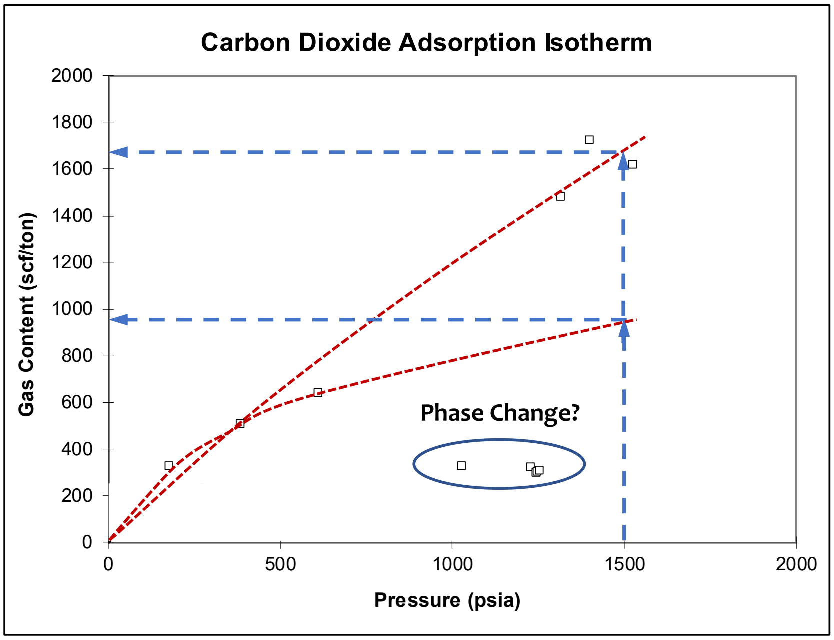

Figure 69. Carbon dioxide adsorption on Ferron coal at 38°C. The irregular nature of the data is attributed to phase changes.

The behavior shown in Figure 69 is intriguing. The reason for the sudden increase of the gas content (up to ~1700+ scf/ton) for pressures higher than P_{CR} can be attributed to the high compressibility of the supercritical CO_2. Figure 70 shows the compressibility of Ar, N_2, and CO_2 as determined from the NIST database. Once the CO_2 is allocated in the porous network of the coal, it will not only adsorb into the coal matrix but also will compress in the void space, allowing many CO_2 molecules to be stored.

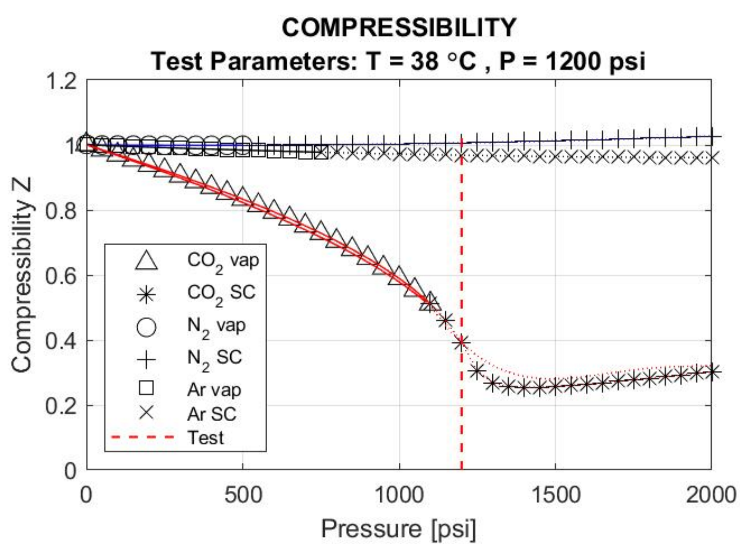

Figure 70. Carbon dioxide compressibility at 38°C.

While significant carbon dioxide can be sequestered, a key question is whether the adsorbed carbon dioxide will remain sequestered if there is a drilling penetration at some time in the future. Consider a case at a depth of 3500 ft. The hydrostatic pressure would be about 1500 psi (0.433 psi/ft and a nominal depth of 3500 ft TVD). A well penetrating this formation, pressurized with water as the wellbore fluid would be in equilibrium with the carbon dioxide in situ and there would not be desorption from the coal or gas produced by expansion drive from the sand. Gas production would occur if the pressure in the penetrating well were decreased and would continue until that well was killed (pressure brought back to hydrostatic). If in time, the carbon dioxide is entombed by some type of mineralization, drawdown or depletion would not immediately produce adsorbed gas.

XIII. Risk Assessment:

To recap.

- Conservative numerical solutions have suggested that an operation with numerous injection wells could successfully sequester carbon dioxide in the Ferron coal, near the existing power plants. The number of wells required would candidly need to be determined by a pilot injection program.
- The Ferron sandstone is interfingered with the coals. These sands will provide higher permeability flow paths to carry the injectate deep into the reservoir. This ideal hypothesized geologic feature of this location can be confirmed with additional numerical modeling but probably requires a pilot program in the field to add credibility.
- Laboratory measurements suggested that there can be some advantages of injecting flue gas without specific separation of the carbon dioxide. There are some exciting possibilities for this type of injection, but again, pilot testing and validation would be necessary.

Pilot testing would seem to be a potential next step. The first course of action for selecting a pilot program is assessing the risks – these include containment and induced seismicity. Certain parameters need to be considered for storage or an enhanced coalbed methane (ECBM) program design. The most appropriate tactic would likely be to use ECBM rather than formal sequestration for any pilot. Regardless, some of the tasks for qualifying a pilot site are as follows.

1. **Regional Evaluation and Initial Site Selection:** With the information collected already, this would be a six-month effort.
2. **Site Characterization:** Activities could include the following.
    a. Pre-characterize selected sites, using the information from DOGM, for wells drilled for oil and gas purposes. For a pilot, consider one injector and four monitoring wells in a five-spot pattern. Supplement the regional evaluation carried out here and carry out an initial site selection.
    b. Carry out site selection, characterize that site in full. Initial site selection has been carried out here, but detailed site selection will require

supplementary measurements beyond those that were made to establish commercial viability. This could include additional logging, coring, fluid sampling, various seismic exploration methods – 3D and VSP for example).

c. Carry out additional reservoir modeling, based on the newly acquired site characterization data.
d. Assess whether legacy wellbores need to be plugged and abandoned.
e. Undertake leasing for pore space and surface access. Research the current leasing arrangements. Land acquisition via leasing and acquisition of pore space rights from property owners over the entire project areal extent (per models). The operator may or may not be interested in participating in a pilot program. Concurrently, this information is used to develop a Monitoring, Reporting, and Verification Plan (MRV).
f. Carry out additional reservoir modeling, based on newly acquired site characterization data.
g. Collect 3D seismic across the plume uncertainty area (where the carbon dioxide will migrate to) and drill another stratigraphic well. Drill this stratigraphic well with continuous coring.
h. Design the injection system and plans for a Class II Injection Well operation. Prepare a Plugging and Abandonment Plan for the ECBM pilot, and an Emergency and Remedial Response Plan. Class II should be viable for ECBM and an experimental program. Consider a five spot with a new injector and up to four surrounding monitoring wells, using existing wells where possible for monitoring. Depending on configuration and well condition, an existing well might be adequate as the injector also, at least for a pilot test.
i. Design pipelines and surface facilities for the pilot.
j. Prepare and apply for permits (AoR and Corrective Action Plan, Testing and Monitoring Plan, Post-Injection Site Care and Site Closure Plan, Emergency and Remedial Response Plan (ERR).
k. For a Class VI permit at some time in the future, demonstration of financial responsibility will be required.

3. **Permitting:** Permitting: An operational, storage-only facility could involve Class VI wells. An experimental pilot could likely get Class II designation. Significant permitting effort should be anticipated. Permit this as an ECBM pilot. The premise would be to produce from the monitoring wells. If there is breakthrough, the carbon dioxide would be reinjected. In a commercial setting, after significant breakthrough, the monitoring wells might be shut in and new wells opened or drilled for injection.
4. **Operations:** Suppose that the pilot proves successful. A commercial-scale operation could be considered. The following outlines some of the activities that could be required for a commercial program. Detailed site characterization and permitting would be undertaken. An MRV plan (Monitoring, Reporting, and

Verification plan) would be required shortly after operation commences and periodic testing will be required to confirm well and reservoir performance, assess the extent of the injected fluid plume and ensure that groundwater quality is not diminished. For a commercial facility, a twenty-year program should be anticipated. This could involve drilling additional wells as time goes on.

a. The site operator takes control of the CO_2 after it is pipelined to the site from the plant.
b. Additional monitoring wells, pumping equipment, and other infrastructure must be in place at the start of injection.
c. There will be operational and maintenance expenses, including testing (mechanical integrity testing, continuous wellhead monitoring, annual noise logs, temperature logs, quarterly corrosion testing …).
d. Corrective action would need to be specified if any anomalies are detected (such as approaching abandoned wells).
e. Monitoring wells will detect issues within and above the injection zone. Dual completions may be feasible to concurrently evaluate above and within the target zone. These could ideally be Class II wells since it is an ECBM pilot. Possible monitoring requirements could be:
    a) One well every 4 mi^2 with a minimum of two wells initially and a minimum of five wells at the end of the planned life.
    b) Within the so-called pressure front area, one well every 50 mi^2 – minimum one well to start and two wells at the end of injection.
    c) Each well would monitor from four depth intervals in the storage zone and four depth intervals above the seal. An annual fluid sampling program is required. The gas in the monitoring wells would be comingled. These wells would also be used as methane production wells.
    d) Groundwater wells are installed to sample USDWs.
f. Atmospheric and near-surface CO_2 concentrations are measured with vadose zone wells, soil gas flux chambers, and eddy covariance towers.
    a. One vadose zone sampling well is installed with each injector and gas is sampled quarterly.
    a. Twenty soil gas flux chambers are used for each injection well for quarterly analysis.
    b. Five eddy covariance towers are located at each injection site for continuous monitoring.

Abandonment and Site Closure: FOR A PILOT, abandonment would follow standard DOGM procedures for a gas producing well.

Long Term Stewardship: FOR A PILOT, this would not be a consideration.

XIV. Economic Considerations

XIV.1 What are the Savings if Separation Requirements were Reduced?

One of the exciting elements of the laboratory work carried out for this project was that there could be some benefits for not separating carbon dioxide from the flue gas before injection. Coal swelling could be mitigated. On the other hand, pumping costs could be increased because the density of the pumped fluid would be decreased. The pertinent question is whether significant savings would result without capture.

One can get a perspective for post-combustion capture economics from published calculations. Ideally, some of these could be avoided if flue gas were injected – not requiring carbon dioxide separation. Regardless, Rubin et al., 2015, published the data in Table 15. Note the rows comparing LCOE (definitions are provided in Appendix C) with and without capture. Avoiding capture is particularly desirable. This is shown by the shaded lines in Table 15.

Indications that sequestration may be possible without a specific capture step are preliminary and based exclusively on laboratory assessments and engineering judgment. Pilot testing would be required. Regardless, this could be a real breakthrough, even if only partial processing is required – removal of H_2S, for example.

XIV.2 What are the Savings in Transportation Costs?

Another favorable aspect of this location (beyond the potential for direct flue gas injection) is that transportation distance would be minimized. Some very approximate estimates can be made by using published transportation data (again extracted from Rubin et al., 2015) shown in Table 16.

Table 16. Transport Costs, after Morgan and Grant (2014) Onshore

Mass Transport Rate (10^6 ton CO_2/year/100 mi)[43]	Cost (US$/ton CO_2/100 mi)
3.2	3.1
30	1.1

For demonstration purposes for a single injector pilot, presume 10 miles of pipeline (there will be multiple production/monitoring wells and there will likely need to be a return line from the producers to the injectors) and assuming 10 injection wells at 10^6 tons/year. For three scenarios, Table 16 would suggest a modest transportation cost since the plants are nearly collocated with coalbed play and the volumes are modest for a pilot program.

43 https://www.netl.doe.gov/projects/files/FENETLCO2TransportCostModel2018DescriptionandUsersManual_050718.pdf

Table 15. Summary of current (circa 2015) and past performances and cost estimates for post-combustion capture at SCPC (* pulverized coal) power plants using bituminous coal values in constant US 2013 dollars (after Rubin et al, 2015).**

Performance and Cost Measures for New SCPC Plants w/Bituminous Coal	Current values			Adjusted SRCCS values			Change in Rep. value (Current−Adjusted SRCCS)	
	Range		Rep. value	Range		Rep. value		
	Low	High		Low	High		Δ value	Δ%
Plant performance measures								
SCPC reference plant net power output (MW)	550	1030	742	462	758	587	155	26
Emission rate w/o capture (t CO_2/MWh)	0.746	0.840	0.788	0.736	0.811	0.762	0.03	3
Emission rate with capture (t CO_2/MWh)	0.092	0.120	0.104	0.092	0.145	0.112	−0.01	−7
Percent CO_2 reduction per MWh (%)	86	88	87	81	88	85	2	
Total CO_2 captured or stored (Mt/yr)	3.8	5.6	4.6	1.8	4.2	2.9	1.7	57
Plant efficiency w/o capture, HHV basis (%)	39.0	44.4	41.4	39.3	43.0	41.6	−0.2	−1
Plant efficiency w/capture, HHV basis (%)	27.2	36.5	31.6	28.9	34.0	31.8	−0.2	−1
Capture energy reqm't. (% more input/MWh)	21	44	32	24	40	31	1.1	3
Plant cost measures								
Total capital reqm't. w/o capture (USD/kW)	2313	2990	2618	1862	2441	2040	578	28
Total capital reqm't. with capture (USD/kW)	4091	5252	4580	2788	4236	3333	1247	37
Percent increase in capital cost w/capture (%)	58	91	75	44	73	63	13	
LCOE w/o capture (USD/MWh)	61	79	70	64	87	76	−6	−8
LCOE with capture only (USD/MWh)	94	130	113	93	144	119	−6	−5
Increase in LCOE, capture only (USD/MWh)	30	51	43	28	57	43	0	−1
Percent increase in LCOE w/capture only (%)	46	69	62	42	65	56	5	
Cost of CO_2 captured (USD/t CO_2)	36	53	46	33	58	48	−3	−6
Cost of CO_2 avoided, excl. T&S (USD/t CO_2)	45	70	63	44	86	67	−4	−6

A good example of potentially required processing, and in particular compression requirements is the Illinois ICCS project.

> “Next, a separator removes any free water produced during cooling, and the CO_2 stream is transported through a 0.61 m diameter, 457 m long pipeline to a compression and dehydration facility. At this facility, the gas is divided into four parallel streams that each feeding a 4-stage, 2424 kW reciprocating compressor resulting in a total compression capacity of 2000 tons per day. Each compressor has six cylinders; two cylinders for the 1st stage, two cylinders for the 2nd stage, one cylinder for the 3rd stage, and one cylinder for the 4th stage of compression. After each stage of compression, the interstage gas is cooled to 35°C using condensing water which is then removed by an interstage separator. … After the 3rd stage of compression, the four CO_2 streams are recombined and sent to the triethylene glycol (glycol) dehydration unit. The combined CO_2 stream enters the bottom of the glycol contactor where it is contacted with the lean glycol (water free) introduced at the top of the unit. The glycol removes water from the CO_2 by physical absorption and the rich glycol (water saturated) exits the bottom of the column. … After the CO_2 leaves the dehydration section, it splits into four streams each stream returning to the 4th stage of the reciprocating compressor where it is compressed to 9.8 MPa and 133°C. Finally, the dehydrated CO_2, which has less than 0.005% moisture by weight (>99.9% CO_2 purity), will be further compressed up to 15.8 MPa using a 298-kW centrifugal booster pump and transported 1610 m through a 0.2 m diameter pipeline to the injection wellhead. …”[44]

XIV.4 What are the Considerations related to Aquifers?

At the conceptual Emery County locations, any injection should be (but would need to be confirmed) well below the Underground Source of Drinking Water (USDW) level thus ensuring the safety of these water sources. USDWs are defined by Underground Injection Control (UIC) regulations as aquifers or portions thereof which contain less than 10,000 milligrams per liter (mg/L) of total dissolved solids (TDS) and are being used or could be used, as a source of drinking water. A hydrologic evaluation of the candidate location would be required.

XIV.5 What Monitoring is Required?

Significant monitoring is required for several reasons:

- avoiding or detecting leakage,
- protecting groundwater,

[44] https://www.carboncapturejournal.com/ViewNews.aspx?NewsID=3346

- detecting and enabling mitigation of microseismicity that exceeds background levels.

Surface and subsurface monitoring equipment are required. In a commercial setting, near-surface instrumentation would include:

- soil carbon dioxide flux monitoring,
- periodic shallow groundwater sampling for geochemical analysis.

Deeper monitoring would require passive seismic surveys, geochemical sampling, and pressure and temperature monitoring.

XIV.6 Well Construction?

In a commercial storage and sequestration setting, Class VI injection wells would require materials and cement that can withstand exposure to flue gas and flue gas/water mixtures without excessive corrosion.

However, for a pilot program or an ECBM operation, Class II well construction may be feasible. It might even be possible, depending on age, condition, and metallurgy to use existing wells for a demonstration program.

XV. Costing Considerations

To highlight costs and development/operational issues, FE/NETL's CO2 Saline Storage Cost Model is used to highlight some of the technical considerations and financial obligations.

XV.1 Volumetrics

One of the first things that needs to be done is to estimate a plume area. Analytically, the model assumes the following equation:

$$A_{pl} = \frac{q_{m-CO2} t_{inj}}{\rho_{CO2} h \phi e_{st}} \tag{16}$$

where:

A_{pl} .... plume area (m^2) – assuming CO_2 injection only,
q_{m-CO2} .... annual average mass rate of CO_2 injection (kg/year),
ρ_{CO2} .... density of CO_2 at reservoir conditions (kg/m^3),
h .... formation thickness (m),
ϕ .... porosity (decimal), and,
e_{st} .... storage coefficient.

To account for coal, this needs to be modified recognizing that storage is by adsorption rather than compressibility in porosity. The alternative that is adopted here is to use simulation data. We will base the plume area calculated at breakthrough using Eclipse.

XV.2 Wells Required?

After estimating the volumetrics, the required number of injection wells would typically be selected using a relationship that is strictly based on radial flow. In this instance, however, we have simulations for two injectors that we have previously used to determine spatial distribution. Regardless, the simplest way to estimate the number of wells required is to first estimate a theoretical capacity for a single well. If neat CO_2 is injected, the relationship below would be used. If flue gas was considered, the viscosity would need to be adjusted slightly.

$$q_{mwmaxf} = a_{LB} kh\,(p_{max} - p_{amb})/\mu_{CO2} \tag{17}$$

where:

q_{mwmaxf} .... maximum mass flow rate of CO_2 for a single well,
a_{LB} .... Law and Bachu coefficient, 0.0208 (tonne/day·m·MPa)/(mD/cP),
k .... effective permeability (mD),
h .... formation thickness (m),
p_{max} .... maximum bottomhole hole injection pressure (MPa),
p_{amb} ....ambient pressure in the storage formation (MPa), and,
μ_{CO2}............................. CO2 viscosity at reservoir temperature and pressure (cP).

The selection we would make is a little more conservative (the maximum BHP would be set at slightly less than the so-called fracturing pressure. Notice that some wells may be dual completions – accessing the injection zone and monitoring above the zone.

XV.3 Other Costs?

After a viable lifetime, the operator would need to set up a trust fund to cover the cost of long-term stewardship. The operator is always conscious of the cash flow for the operations. The cash flow is determined as the price of storing CO_2 in dollars per tonne (or ton) multiplied by the mass of CO_2 stored per year. Credits could make operations favorable. Future value is considered. Depreciation schedules are generated for all capital costs according to IRS guidelines. In a permanent storage scenario, there is a cost of complying with requirements for Class VI injection. This includes planning (and if necessary, implementing) corrective action, plugging, abandonment, site closure, and eventual remediation and restoration.

What are some order of magnitude costs for a commercial sequestration site? Consider some examples, as follows.

Capital Expenditures

Cryogenic Air Separation Plant or Similar Processing. This includes compression equipment. The Emery County situation might require less processing if flue gas can be directly used. This would be for a permanent installation. A pilot could use industrial gas and rental pumping equipment.	$7,500,000	The basis for these estimates was $250,000/MMcfD capacity. We will assume 10 wells, each injecting 2 MMcfD and a 50% contingency.
Pipeline. The prices shown are for a small commercial operation. The 10 miles is a low-end estimate that would need to be refined. For a pilot, pipeline costs would be negated.	$3,600,000	Assume a commercial scheme would be costed at $30,000 per inch-mile and presume a 12-inch line and 10 miles of piping
Connections to Trunklines. In a commercial setting, each well would be connected to a 12-inch line with a 6-inch line.	$600,000	Assume a commercial scheme would be costed at $20,000 per inch-mile and presume a 6-inch line and 10 wells with an average of 0.5 miles/well.
Drilling and completing new wells.	$7,000,000	Assume a commercial scheme would be costed at $200/ft for 3500 ft deep wells and 10 wells. A pilot might use existing wells. This is a very low-end estimate.
Total	$18,800,000	**This is a low-end estimate for a commercial operation. It does not include, planning, leasing, site characterization, monitoring ….**

Operating Expenditures

Injection well operations	\$10,000/month	An outdated estimate was \$500/month. Today, one might estimate, with compression costs, \$1000/well/month. Wells may be cycled on and off according to pressure considerations. Compression costs will likely be higher if flue gas is injected as opposed to carbon dioxide.
Cost of gas	\$	Gas would be provided from the plant. Cost depends on the separation that is required.
Handling breakthrough fluid	\$0.50 Mcf	Methane can go to sales. However, CO_2 or flue gas would need to possibly be separated and certainly recirculated back for reinjection.

There are numerous additional costs including conventional financial considerations such as production taxes, discount rates …. Figure 71, from the FE-NETL model shows some of the other standard financial considerations for a commercial sequestration project. The values entered are generic and would be situation-dependent.

Inputs Related to Financial Module			
Financial Item	Value	Defaults	Units/ Comments
Percent Equity (remainder is debt)	55.0%	55.0%	Capitalization
Cost of Equity	12.0%	12.0%	
Cost of Debt	5.5%	5.5%	Interest rate
Tax Rate	38.0%	38.0%	Matches PSFM
Escalation Rate	3.0%	3.0%	
General and Administrative (G&A) Factor	20%	20.0%	Assessed on all labor costs
Site Selection & Site Characterization Failure Contingency	0%	0.0%	Assessed to account for sites failing
Process Contingency Factor	20%	20.0%	Assessed on all monitoring costs
Project Contingency Factor	15%	15.0%	Assessed on all capital costs
Lease bonus	\$ 50.00		\$/acre
Injection Fee (for lease holders)	\$0.25		\$/tonne
Long-term Stewardship Trust Fund (State)	\$0.07		\$/tonne
Operational Oversight Fund (State)	\$0.01		\$/tonne

Figure 71. There are financial expenditures associated with financing a commercial project as wells as some long-term funding obligations for stewardship.

Other financial costs to consider include potential costs for Corrective Action. Injection well plugging is enfranchised in stewardship funding which also includes long-term monitoring, PSC, and Site Closure as well as potential expenditures for Emergency and Remedial Response (ERR).

The real differentiating element these days could be Q45 tax credits (https://sgp.fas.org/crs/misc/IF11455.pdf). Refer to the sidebar.

Table 1. Key Elements of the Section 45Q Credit

Equipment Placed in Service Before 2/9/2018	Equipment Placed in Service on 2/9/2018 or Later
Credit Amount (per Metric Ton of CO_2)*	
Geologically Sequestered CO_2	
\$23.82 in 2020. Inflation-adjusted annually.	\$31.77 in 2020. Increasing to \$50 by 2026, then inflation-adjusted.
Geologically Sequestered CO_2 with EOR	
\$11.91 in 2020. Inflation-adjusted annually.	\$20.22 in 2020. Increasing to \$35 by 2026, then inflation-adjusted.
Other Qualified Use of CO_2	
None.	\$20.22 in 2020. Increasing to \$35 by 2026, then inflation-adjusted.
Claim Period	
Available until 75 million tons of CO_2 have been captured and sequestered.	12-year period once facility is placed in service.
Qualifying Facilities	
Capture carbon after 10/3/2008.	Begin construction before 1/1/2026.
Annual Capture Requirements	
Capture at least 500,000 metric tons.	*Power plants:* capture at least 500,000 metric tons. *Facilities that emit no more than 500,000 metric tons per year:* capture at least 25,000 metric tons. *DAC and other capture facilities:* capture at least 100,000 metric tons.
Eligibility to Claim Credit	
Person who captures and physically or contractually ensures the disposal, utilization, or use as a tertiary injectant of the CO_2.	Person who owns the capture equipment and physically or contractually ensures the disposal, utilization, or use as a tertiary injectant of the CO_2.

Source: CRS analysis of IRC Section 45Q.

XV.4 Time Frames?

A pilot program could be carried out over a relatively short time frame (with site characterization, installation of monitoring, permitting, leasing negotiations, field injection testing) a time frame of one to two years would be anticipated. For a commercial sequestration operation, the anticipated times for a hypothetical site are shown in Figure 72.

		Duration (Yrs)	Begin Year	End Year	Calendar
Year Project Begins:	**Site Screening**	1	1	1	2024 - 2024
	Site Selection & Site Characterization	3	2	4	2025 - 2027
	Permitting & Construction	2	5	6	2028 - 2029
2024	**Operations**	30	7	36	2030 - 2059
	PISC and Site Closure	50	37	86	2060 - 2109

Figure 72. A hypothetical commercial project with durations of different stages.

XVII. Assessment of Benefits

This study:

1. Carried out fundamental laboratory experimentation and modeling that highlighted **technical, economic, and environmental** costs and benefits for a specific CO_2 source (Huntington or Hunter plant) to sequester CO_2 in the Emery coal seams. The key aspects of the study are:

a. If delivery and storage are in the coal alone, one simulation scenario suggested an individual well could sequester on the order of 1 million tons of carbon dioxide. This number is contingent on the proximity of the producing well in an ECBM operation and is a low-end estimate that considers breakthrough in a nearby producer.
b. Injection rate limitations suggested a daily injection rate limitation of 2 MMscfD. This would mandate twenty to thirty injection wells at a minimum to handle emissions.
c. The storage and delivery of the CO_2 are favored by the local geology where the interfingered sands are immune to adsorptive swelling and permeability reduction that is experienced by the coals. This swelling in the coal is known to reduce permeability locally. The sands would provide conductive pathways to bypass these restrictions – all within an effective upper and lower seal. This could be an outstanding attribute of this site.
d. The perceived effectiveness of the seals, the role of the sands, and the native sequestration potential of the sands would favor a field pilot.
e. The economics are impacted by the laboratory demonstration that flue gas could be injected and that the depressed coal permeability would be mitigated. This has advantages of potentially reducing pre-injection separation but could be associated with nitrogen breakthrough (and the processing thereafter) and increased compression costs because of the reduced hydrostatic head.
f. From an environmental potential, the formation is below aquifers, but the regional geologic study is still necessary to understand the consequences of outcropping in the San Rafael Swell. Upper and lower seals would appear to be effective.
g. It would initially seem to be appropriate to permit this as an ECBM operation and the methane can go to sales and be used for running compression equipment.

2. Considered whether **local coalbeds are conducive** to enhanced CO_2 methane recovery. The observations are:
    a. Simulations suggest ECBM would be effective.
    b. The adsorptive capacity is high –certainly very viable for sequestration.
    c. Produced methane could be used to drive compression equipment and go to sales.
3. Identified new technologies for **improving injection efficiency** and attempt to identify supplementary funding opportunities for field-scale evaluation.
    a. The two most important concepts developed by this research relate to:
        i. The interfingered sand will help to bypass swelling-induced permeability reduction.
        ii. It is feasible to use flue gas for the ECBM – or at least blends of nitrogen and carbon dioxide.

    iii. This is an ideal time for soliciting pilot funding opportunities, considering Q45 credits.

4. Considered the risk of **induced seismicity will be reduced** in comparison to carbon dioxide injection into deep saline aquifers (without "voidage/injectate" volume compensation).
    a. It is anticipated that the risk of induced seismicity requires further study, but that the adsorption sink of the coal may keep formation pressure from aggressively increasing with injection.
    b. Further geologic analysis is required to de-risk the operation.

XVIII. Pilot Study to Address Technical Challenges

XVIII.1 Can Flue Gas be Injected?

What is the effectiveness of methane capture and purification required of the gas stream before injection? If flue gas can be tolerated, there could be some advantages. The advantage is not necessarily that NOx can be sequestered but that the presence of nitrogen may enable moving CO_2 deeper into the coal (speculation at this point). The study has indicated that blends of nitrogen and carbon dioxide can be injected with less swelling potential. In fairness, there is less carbon dioxide injected per cubic meter of fluid injected and it is unknown if the swelling will evolve as more carbon dioxide is injected or whether there will be a plateau reached because of the partial pressures of the injectate. Considering this would be a goal of a pilot study.

XVIII.2 Can Flue Gas be Injected?

The true **capacity** for carbon dioxide storage in coals in-situ can be established with pilot testing. Continuous injection below fracturing pressure may not be a realistic scenario. The potential for refined injection procedures including fracturing, water stages, and in particular horizontal wells, might alleviate the mismatch between a large and constant CO_2 supply and the sequestration volume in the coals.

XVIII.3 Seal Integrity?

Seal integrity and permanence of sequestration are always a concern for subsurface storage. Effective monitoring is required. Injection of water, particularly calcified water after periodic injection of carbon dioxide could afford mineralization and more permanent sequestration. Predicting, monitoring, and mitigating leakage is a common theme of all subsurface storage operations.

The seals are superficially quite good (Mancos shale). Without mineralization, sequestration is controlled by avoiding underbalanced penetrations. Some local plugging and abandonments would need to be considered in developing an engineering plan for a pilot test.

XVIII.4 Coal Swelling?

Coal swelling impacts coalbed methane production. The experience in the past has been that chemisorption and associated swelling have reduced cleat permeability. Tactical changes in the injection strategy – multiple horizontal wells, with water diversion stages and pressures above fracturing are envisioned to effectively provide conformal injection and storage of CO_2 through the bulk of the reservoir. The potential geologic advantage, in this case, is the presence of interfingering sands which may be able to move injectate past locally plugged zones. Direct flue gas injection seems to be a real possibility for mitigating swelling.

XVIII.5 Logistics?

Logistics and feasibility of piping CO_2 or flue gas to injection equipment from a plant environment to the injection facility are favored by the proximity of the coalbeds to the plants.

XVIII.6 Pilot Plant Funding

A possibly favorable geologic scenario has been identified. Additionally, non-traditional injection technologies (injection above fracturing pressure, sequential injection of water, mineralization encouragement, and others) are likely to dramatically increase storage capacity. However, this remains a challenging sequestration scenario – there are significant emissions and multiple wells would be required. The economics could be favorable if it is permitted as an ECBM play. The expenditures to qualify as a dedicated sequestration-only site are significant. Q45 credits could strongly influence the viability.

XVIII.7 Required Field Operations for Pilot Planning

Consider the basic field operations for preparing for an ECBM pilot.

Production and Monitoring Well Selection:

Presume that something like a five-spot will be implemented and that this will be an ECBM program rather than sequestration alone. Existing wells would be used for the production. These wells would also serve as monitoring wells for the pilot. The produced methane would be used to compress the fluid to be injected. The first detailed engineering effort would be to evaluate the cementing records for all the casing strings in these wells. It will be necessary to confirm that there are no wet shoes (contaminated or no cement in the casing section between float collar and shoe after a primary cement job). Each one of these producers will need to have a baseline suite of logs for corrosion assessment (casing integrity logging). It will be necessary to change out the C sections of the wellheads to ensure corrosion resistance. The C section is the production section of the wellhead. This is used to land production tubing. The standard C section is a set of slips with rubber plates for pack off. The CO_2 C section will be a hanger rubber that slips over the tubing with a screw-on flanged wellhead. This will prevent any CO_2 corrosion to the wellhead. If corrosion damage occurs, the pressure rating is lowered, and it will be necessary to change out the wellhead.

Injection Well:
Presume that an existing well can be repurposed, rather than having to drill a new well. As with the producers, it will be necessary to select a well that is optimally located and with an appropriate cementing record, particularly no wet shoe. There should be no history of corrosion. The casing will need to be pressure tested. Before this testing, preparation will include pickling, running a casing scraper, and running a casing integrity log to assess defects and casing thickness. It is necessary to install a high corrosion-resistant wellhead and valves. The injection string would include a nickel-coated packer and corrosion-resistant tubing (stainless steel).

Infrastructure and Testing
An injection building (control panel, wiring to CO_2 code) will house an electric injection pump(s). A suction and discharge manifold system is required along with the main injection line to the well and pressure sensors for the piping. Injection testing with CO2/flue gas and water will be needed to prescribe a ceiling pressure for injection. This is conventional thinking. In fact, controlled small volume microhydraulic fracturing may be appropriate for bypassing swollen coal sections.

Production
A membrane-based system will high-grade carbon dioxide that breaks through. In a commercial situation, this would be required to ensure pipeline quality methane. Regardless, produced carbon dioxide would be gathered from the four wells for reinjection.

Nomenclature

Symbol	Description	Unit
C_d	Deep conductivity	$(ohm \cdot m)^{-1}$
c_f	Pore volume compressibility	psi^{-1}
C_m	Mud conductivity	$(ohm \cdot m)^{-1}$
C_s	Shallow conductivity	$(ohm \cdot m)^{-1}$
ε_L	Strain	dimensionless
Gc	Gas content	scf/ton
K	Bulk modulus	psi
K_f	Cleat permeability	mD
K_{rg}	Relative permeability to gas	dimensionless
K_{rw}	Relative permeability to water	dimensionless
M	Axial modulus	psi
m_f	Mud filtrate resistivity	ohm·m
P	Pressure	psi
Pi	Initial pressure	psi

P_L	Langmuir pressure	psi
R_{lls}	Shallow lateral resistivity	ohm·m
R_{mf}	Mud filtrate resistivity	ohm·m
V_{ash}	Ash volume	m^3
V_w	Moisture content	m^3
w	Cleat width	μm
ρ_b	Bulk density	g/cm^3
ρ_f	Ash density	g/cm^3
ρ_{ma}	Matrix density	g/cm^3
ϕ_f	Cleat porosity	dimensionless
ϕ_i	Initial cleat porosity	dimensionless
ϕ	Porosity	dimensionless

Acknowledgments
The authors gratefully acknowledge the financial support of PacifiCorp to carry out this research contract number 3300001843. The authors also acknowledge Schlumberger Services for the academic licenses of the Petrel and Eclipse software suites used for the research.

References
1. Advanced Resources International, Southwestern Regional Partnership For Carbon Sequestration (Phase 2) Pump Canyon CO2- ECBM/Sequestration Demonstration, San Juan Basin, New Mexico U.S. DOE Award No: DE-FC26-05NT42591. Houston, TX January 31, 2010.
    - Adams, M. A., and Kirr, J. N. 2021. Geologic Overview, Coal Deposits, and Potential Methane Recovery from Coalbeds of the Uinta Basin—Utah and Colorado. In C. T. Rightmire, G. E. Eddy, and J. N. Kirr (eds.), *Coalbed Methane Resources of the United States*. American Association of Petroleum Geologists. https://doi.org/10.1306/st17437c10.
2. Ali, M., A. Aftab, F.U.R. Awan, H. Akhondzadeh, A. Keshavarz, A. Saeedi, S. Iglauer, and M. Sarmadivaleh, CO2-wettability reversal of cap-rock by alumina nanofluid: Implications for CO2 geo-storage. Fuel Processing Technology, 2021. 214: p. 106722.
3. Ali, M., F.U.R. Awan, M. Ali, A. Al-Yaseri, M. Arif, M. Sánchez-Román, A. Keshavarz, and S. Iglauer, Effect of humic acid on CO2-wettability in sandstone formation. Journal of Colloid and Interface Science, 2021. 588: p. 315-325.
4. Anderson, P. B., T. C. Chidsey Jr., T. A. Ryer, R. D. Adams, and K. McClure, 2004, Geologic framework, facies, paleogeography, and reservoir analogs of the Ferron Sandstone in the Ivie Creek area, east-central Utah, in T. C. Chidsey Jr., R. D. Adams, and T. H. Morris, eds., Regional to wellbore analog for fluvial-deltaic reservoir modeling: Deveugle et al. 761 The Ferron Sandstone of Utah: AAPG Studies in Geology 50, p. 331–356.

5. Arri, L.E., D. Yee, W.D. Morgan, and M.W. Jeansonne, Modeling Coalbed Methane Production with Binary Gas Sorption. 1992, SPE 24363, Rocky Mountain Reg. Mtg, Casper, WY.
6. Bachu, S. and Stewart, S. (2002): Geological sequestration of anthropogenic carbon dioxide in the Western Canada Sedimentary basin: Suitability analysis; Journal of Canadian Petroleum Technology, v. 41, no. 2, p. 32-40.
7. Berkowitz, N., The Chemistry of Coal. Vol. p. 86. 1985, New York City: Elsevier Science.
8. Bird, R. B. (Robert B., Stewart, W. E., & Lightfoot, E. N. (2006). Transport phenomena (2nd ed., p. 928). J. Wiley
9. Boyeldieu, C. and A. Winchester, Use of Dual Laterolog for the Evaluation of the Fracture Porosity in Hard Carbonate Formations. 1982.
10. Burns, T.D. and R.A. Lamarre. Drunkard's Wash Project: Coalbed Methane Production from Ferron Coals in East-Central Utah. in International Coalbed Methane Symposium, University of Alabama. 1997. Tuscaloosa, Alabama.
11. Caroll, R.E., J.C. Pashin, M.R. McIntyre, R.H. Groshong Jr, and R.M. Bustin, Carbon Sequestration and Enhanced Recovery Potential of Mature Coalbed Methane Reservoirs in Black Warrior Basin, in AAPG Studies in Geology. 2009, AAPG. p. 125-147.
12. Condon, S.M., Fracture network of the Ferron Sandstone Member of the Mancos Shale, east-central Utah, USA. International Journal of Coal Geology, 2003. 56(1-2): p. 111-139.
13. Conway, M.W. Characterization and Performance of Coalbed Methane Wells in Drunkard's WashCarbon County, Utah. in Coalbed Methane Symposium. 1997. Tuscaloosa, Alabama.
14. Dallegge, T.A. and C.E. Barker, Coal-Bed Methane Gas-In-Place Resource Estimates Using Sorption Isotherms and Burial History Reconstruction: An Example from the Ferron Sandstone Member of the Mancos Shale, Utah. 2013. Paper 1625-B*.
15. Deveugle, P.E.K., Jackson, M.D., Hampson, G.J., Stewart, J., Clough, M.D., Ehighebolo, T., Farrell, M.E., Calvert, C.S., and Miller, J.K. 2014. A comparative study of reservoir modeling techniques and their impact on predicted performance of fluvial-dominated deltaic reservoirs, AAPG Bulletin, v. 98, no. 4 (April 2014), pp. 729–763.
16. Environmental Protection Agency. Overview of Greenhouse Gases. 2019, Environmental Protection Agency.
17. Ertürk, M.C., Production Performance of Coal Bed Methane, Shale Gas and Tight Gas Reservoirs with Different Well Trajectories and Completion Techniques, in Petroleum and Natural Gas Engineering. 2013, Middle East Technical University.
18. Evaluation of Impacts to Underground Sources of Drinking Water by Hydraulic Fracturing of Coalbed Methane Reservoirs. United States Environmental Protection Agency, 2004.

19. Finkbeiner, T., B.B. Stump, M.D. Zoback, and P.B. Flemings, Pressure(P), Overburden (Sv), and Minimum Horizontal Stress (Shmin) in Eugene Island Block 330, Offshore Gulf of Mexico. 1996, Gas Research Institute (GRI-96/0285): Pennsylvania.
20. Glover, P.W.J., A generalized Archie's law for n phases. 2010. 75(6): p. E247-E265.
21. Godec, M., G. Koperna, and J. Gale, A Review of its Status and Global Potential. 2014. 63: p. 5858-5869.
22. Gunter, W., S. Wong, D. Law, F. Sanli, Y. Jianping, and F. Zhiqiang, Enhanced Coalbed Methane (ECBM) Field Test at South QinShui Basin Shanxi Province, China, GCEP Workshop, August 22-23, 2005, Beijing, PRC.
23. Gunter, W.D., Mavor, M.J., and Robinson, J.R. CO2 storage and enhanced methane production: Field testing at Fenn-Big Valley, Alberta, Canada, with application, Greenhouse Gas Control Technologies 7, Proc. 7th International Conference on Greenhouse Gas Control Technologies 5– September 2004, Vancouver, Canada, Volume I, 2005, Pages 413-421. XIV.
24. Hale, L.A. and F.R. Van De Graaff. Cretaceous stratigraphy and facies patterns-northeastern Utah and adjacent areas. in 13th Annual Field Conference. 1964.
25. Harpalani, S., B.K. Prusty, and P. Dutta, Methane/CO2 sorption modeling for coalbed methane production and CO2 sequestration. 2006. 20(p. 1591-1599).
26. Hendry, D., Miller, A., Wilkinson, N., Wicramathilaka, M., Espanani, R., and Jacoby, W. 2013. Exploration of High Pressure Equilibrium Separations of Nitrogen and Carbon Dioxide, J. of CO_2 Utilization, 3-4, 37-43.
27. Hefti, M., and Mazzotti, M. (2018). Postcombustion CO2 Capture from Wet Flue Gas by Temperature Swing Adsorption. Industrial and Engineering Chemistry Research, 57(45), 15542–15555. https://doi.org/10.1021/acs.iecr.8b03580
28. Huang, D., & Li, W. (2018). A brief review on the buoyancy criteria for supercritical fluids. In Applied Thermal Engineering (Vol. 131, pp. 977–987). https://doi.org/10.1016/j.applthermaleng.2017.12.042
29. Krupnick, A.J., R.J. Kopp, k. Hayes, and S. Roeshot, The Natural Gas Resources Revolution: Critical Questions for Sustainable Energy Future. 2014, Resource for the Future, REE Report: Washington DC. https://media.rff.org/documents/RFF-Rpt-NaturalGasRevolution.pdf.
30. He, Q., S.D. Mohaghegh, and V. Gholami, A Field Study on Simulation of CO2 Injection and ECBM Production and Prediction of CO_2 Storage Capacity in Unmineable Coal Seam. 2013.
31. Jie, S., Z. Changchun, H. Zhaohui, X. Liang, Y. Yuqing, Z. Guohua, and W. Wenwen, Log evaluation of a coalbed methane (CBM) reservoir: a case study in the southern Qinshui basin, China. 2014. 11(1).
32. Koperna, G.J., A.Y. Ouidinot, G.R. McColpin, N. Liu, J.E. Heath, A. Wells, and G.B. Young. CO2-ECBM/Storage Activities at the San Juan Basin's Pump Canyon Test Site. in SPE Annual Technical Conference and Exhibition, 4-7 October. 2009. New Orleans, Louisiana: SPE.
33. Lamarre, R.A., Chapter 22: Coalbed Methane Production from Ferron Coals at Buzzard Bench Field, Utah, in AAPG Studies in Geology No. 50: Regional to Wellbore

Analog for Fluvial-Deltaic Reservoir Modeling: The Ferron Sandstone of Utah, J. Thomas C. Chidsey, R.D. Adams, and T.H. Morris, Editors. 2004, The American Association of Petroleum Geologists and the Society of Exploration Geophysicists.

34. Laxminarayana, C.X. Cui, and R. Bustin. Implications of Volumetric Swelling/Shrinkage of Coal in Sequestration of Acid Gases. 2004. Tuscaloosa, Alabama USA: Proc. Int. Coalbed Methane Symposium.
35. Levine, J. R. (1996). Model study of the influence of matrix shrinkage on absolute permeability of coal bed reservoirs. In R. Gayer & I. Harris (Eds.), Coalbed Methane and Coal Geology (Vol. 109, Issue 1, pp. 197–212). https://doi.org/10.1144/GSL.SP.1996.109.01.14
36. Li, J., D. Liu, Y. Yao, and Y. Qiu, Evaluation of the Reservoir Permeability of Anthracite Coals. 2011. 87(2): p. 121-127.
37. Liang, J.T., K.T. Raterman, and E.P. Robertson. A mechanistic model for CO2 sequestration in Tiffany coal bed methane field. in International Coalbed Methane Symposium, University of Alabama. 2003. Tuscaloosa, Alabama.
38. Mathews, J.P., O. Karacan, P. Halleck, G.D. Mitchel, and A. Grader. Storage of pressurized carbon in coal observed using X-ray tomography. First National Conference on Carbon Sequestration. 2001. Washington, D.C. http://www.netl.doe.gov/publications/proceedings/01/carbon_seq/7a4.pdf.
39. Mavor, M.J., W.D. Gunter, and J.R. Robinson. Alberta multiwell micro-pilot testing for CBM properties, enhanced methane recovery and CO2 storage potential. in SPE Annual Technical Conference and Exhibition. 2004. Houston, Texas: SPE 90256.
40. McPherson, B., M. Cather, R. Middleton, T. Chidsey, J. Heath, M. Saunders, and S.-Y. Lee, CarbonSAFE Rocky Mountains Phase I: Ensuring Safe Subsurface Storage of CO2 in the Intermountain West, DE-FE0029280. 2018.
41. Morad, K., R. Mireault, and L. Dean, Reservoir Engineering for Geologists: Coalbed Methane Fundamentals. 2007. Article 12: p. 47-48.
42. NIST. (2021). Thermophysical Properties of Fluid Systems. National Institute of Standards and TechnoNationallogy. https://webbook.nist.gov/chemistry/fluid
43. Olajossy, C.A., Why Coal Bed Methane (CBM) Production in Some Basins is Difficult. 2019. 12(15).
44. Ottiger, S., Pini, R., Storti, G., and Mazzotti, M. (2008). Measuring and modeling the competitive adsorption of CO2, CH4, and N2 on a dry coal. Langmuir, 24(17), 9531–9540. https://doi.org/10.1021/la801350h.
45. Pagnier, H. Field Experiment Of ECBM-CO2 In The Upper Silesian Basin Of Poland (Recopol). in SPE Europec/EAGE Annual Conference, 13-16 June. 2005. Madrid, Spain: SPE.
46. Palmer, I., B. Moore, and D. Loftin. Cleat Porosity of Coals: New Understanding. in CoalSeq Forum VII. 2011. Houston: Higgs-Palmer and BP America.
47. Palmer, I.D. and J. Mansoori. How Permeability Depends Upon Stress and Pore Pressure in Coalbeds: A New Model. in SPE Annual Technical Conference and Exhibition. 1996. Denver, Colorado: SPE.

48. Patel, N. C. & Teja, A. S. A new cubic equation of state for fluids and fluid mixtures. Chem. Eng. Sci. 37, 463–473 (1982).
49. Pan, Z., J. Ye, F. Zhou, Y. Tan, L.D. Connell, and J. Fan, CO2 storage in coal to enhance coalbed methane recovery: a review of field experiments in China. 2017. 60(5-6): p. 754-776.
50. Peaceman, D.W. Interpretation of well-block pressures in numerical reservoir simulation. in 52nd Annual Fall Technical Conference and Exhibition. 1978. Denver: SPE.
51. Pekot, L.J. and S.R. Reeves. Modeling the effects of matrix shrinkage and differential swelling on coalbed methane recovery and carbon sequestration. in Presented at the 5-2003 International Coalbed Methane Symposium, 5-9 May. 2003. Tuscaloosa, Alabama.
52. Peng, D.-Y., & Robinson, D. B. (1976). A New Two-Constant Equation of State. Industrial & Engineering Chemistry Fundamentals, 15(1), 59–64. https://doi.org/10.1021/i160057a011
53. Puri, R. and D. Yee. Enhanced Coalbed Methane Recovery. SPE Paper 20732, SPE 65th Annual Technical Conference and Exhibition. 1990. New Orleans, LA.
54. Quere, L., R.M. Andrew, P. Friedlingstein, S. Stitch, J. Huack, and J. Pongratz, Share of Global CO2 Emissions (Global Carbon Project and CDIAC). 2018.
55. Rai, V., D.G. Victor, and M.C. Thurber, Carbon capture and storage at scale: Lessons from the growth of analogous energy technologies. Energy Policy, 2010. 38(8): p. 4089-4098.
56. Redlich, O., & Kwong, J. N. S. (1949). On the thermodynamics of solutions. V. An equation of state. Fugacities of gaseous solutions. Chemical Reviews, 44(1), 233–244. https://doi.org/10.1021/cr60137a013
57. Reeves, S. and A. Oudinot, The Allison CO2 – ECBM Pilot, A Reservoir and Economic Analysis Coal. 2005.
58. Reeves, S. and A. Taillefert, Reservoir modeling for the design of the RECOPOL CO2 sequestration project, Poland. 2002, US DOE.
59. Reeves, S. Geological Sequestration of CO2 in Deep, Unmineable Coalbeds: An Integrated Research and Commerical-Scale Field Demonstration Project. in SPE Annual Technical Conference and Exhibition, 30 September. 2001. New Orleans, Louisiana: SPE.
60. Reeves, S., A. Taillefert, L. Pekot, and C. Clarkson, The Allison Unit CO2-ECBM Pilot: A Reservoir Modeling Study. 2003, US DOE DE-FC26-0NT40924.
61. Robertson, E.P., Enhanced Coal Bed Methane Recovery and CO2 Sequestration in the Powder River Basin. 2010, Idaho National Laboratory.
62. Rodriues, C.F., C. Laiginhas, M. Fernandes, M.J. Lemosd e Sousa, and M.P. Dinis, The coal cleat system: A new approach to its study. 2014. 6(3): p. 208-218.
63. Rubin, E.S. Davison, J.E., and Herzog, H.I. 2015. The cost of CO_2 capture and storage, International Journal of Greenhouse Gas Control, 40, 378–40.
64. Ryer, T.A., Stratigraphic, Facies and Depositional History of the Ferron Sandstone in the Canyon of Muddy Creek, East Central Utah. 1991. 19: p. 45-54.

65. Saghafi, A., Discussion on determination of gas content of coal and uncertainties of measurement. 2017. 27(5): p. 741-748.
66. Schmidt, G., & Wenzel, H. (1980). A modified van der Waals type equation of state. Chemical Engineering Science, 35(7), 1503–1512. https://doi.org/https://doi.org/10.1016/0009-2509(80)80044-3
67. Schroeder, K., E. Ozdemir, and B.I. Morsi, Sequestration of carbon dioxide in coal seams. 2002, Energy & Environment Research. p. 54-63.
68. Sharp et al.
69. Shi, J. and S. Durucan A Model for Changes in Coalbed Permeability during Primary and Enhanced Methane Recovery. 2005. 8(4).
70. Shi, J.Q., S. Durucan, and M. Fujioka, A reservoir simulation study of CO_2 injection and N_2 flooding at the Ishikari coalfield CO_2 storage pilot project, Japan. 2008, International Journal of Greenhouse Gas Control. p. 47-57.
71. Sibbit, A.M. and O. Faivre, The Dual Laterolog Response In Fractured Rocks. 1985: p. 17-20.
72. Soave, G. (1972). Equilibrium constants from a modified Redlich-Kwong equation of state. Chemical Engineering Science, 27(6), 1197–1203. https://doi.org/https://doi.org/10.1016/0009-2509(72)80096-4
73. Song. C., Pan, W., Srimat, S.T., Zheng, J., Li, Y., Wang, Y-H., Xu, B-Q., and Zhu, Q-M. 2004. Tri-reforming of Methane over Ni Catalysts for CO_2 Conversion to Syngas with Desired H_2/CO Ratios using Flue Gas of Power Plants without CO_2 Separation, Studies in Surface Science and Catalysis, 153, S.-E. Park, J.-S. Cang and K.-W. Lee (ed.), Elsevier B.V.
74. State of Utah Division of Oil, Gas, and Mining, in Online Oil and Gas Information System. 2019.
75. Steinberg, M. Decarbonization and sequestration for mitigating global warming. in First National Conference on Carbon Sequestration. 2001. Washington, D.C.
76. Stevens, S.H., CO2-ECBM: Insights from USA and International CBM Pilots. 2002: Houston, Texas.
77. Stevens, S.H., D. Spector, and P. Riemer. Enhanced coalbed methane recovery using CO2 injection: worldwide resource and CO2 sequestration potential. in Presented at SPE International Oil and Gas Conference and Exhibition in China. 1998. Beijing, China: SPE Paper 48881.
78. Sutton, T., Wireline Logs for Coalbed Evaluation. 2014.
79. Tao, S., Y. Wang, D. Tang, H. Xu, Y. Lv, W. He, and Y. Li, Dynamic variation Effects of Coal Permeability during the Coalbed Methane Development Process in the Qinshui Basin, China. 2012. 93: p. 16-22.
80. Utah Division of Oil, Gas, and Mining. 2021 [cited 2021; Available from: https://oilgas.ogm.utah.gov/oilgasweb/live-data-search/lds-main.xhtml.
81. Utah Geological Survey: Ferron Sandstone Project Moves to Reservoir Simulation Stage. 1996, Utah Geological Survey (UGS), Petroleum News (May). p. 2-4.
82. Utah Township, Range, and Meridian. 2006.

83. Van Bergen, F., H. Pagnier, and P. Kryzystolik, Field experiment of enhanced coalbed methane-CO2 in the upper Silesian basin of Poland. 2006. 13: p. 201-224.
84. Vangkilde, P.T., K.L. Anthonsen, N. Smith, K. Kirk, F. Neele, B. Van der Meer, Y.L. Gallo, D. Bossie-Codreanu, A. Wojcicki, Y.M. Nindre, C. Hendriks, F. Dakhoff, and N.P. Christense, Assessing European capacity for geological storage of carbon dioxide—the EU geocapacity project. 2009, Energy Procedia. p. 2663-2670.
85. White, C.M., D.H. Smith, K.L. Jones, A.L. Goodman, S.A. Jikich, R.B. La-Count, and T.K. Schroeder, Sequestration of carbon dioxide in coal with enhanced coalbed methane recovery. 2005. 19(3): p. 659-724.
86. Wong, S., D. Law, X. Deng, J. Robinson, B. Kadatz, W.D. Gunter, Y. Jianping, F. Sanli, and F. Zhuqiang. Enhanced coalbed methane and CO2 storage in anthracitic coals—Micro-pilot test at South Qinshui, Shanxi, China. 2007. International Journal of Greenhouse Gas Control.
87. Xue, Z. and T. Ohsumi. Coal matrix swelling caused by adsorption of carbon dioxide and its impact on permeability. in Proceedings of the 7th International Conference on Greenhouse Gas Control Technologies 5. 2004. Vancouver, Canada: Research Institute of Innovative Technology for the Earth (RITE).
88. Yang, S., Y. Cai, R. Wei, and Y. Zhou, A new fracture permeability model of CBM reservoir with high-dip angle in the Southern Junggar Basin. 2019. 37(1): p. 125-143.
89. Yang, Y., T. Song, S. Chen, and T. Li, Experimental Study on Strength Discreteness and Triaxial Compression of Coal Rock Soil Mechanics. 2006. 31(11): p. 3469-3474.
90. Ye, J., S. Feng, and Z. Fan, Micro-pilot test for enhanced coalbed methane recovery by injecting carbon dioxide in south part of Qinshui Basin. 2007. 28: p. 77-80.

Appendix A Mathematical formulations for Equations of State

Equation of State

EOS General form:

$$P = \frac{RT}{V-b} - \frac{a}{V^2+uV-w^2}$$

EOS as a cubic function

$$Z^3 + (U - B - 1)Z^2 + \left(A - U(1+B) - W^2\right)Z + \left(W^2(1+B) - AB\right) = 0$$

$$A = a\,\frac{P}{(RT)^2} \qquad U = u\,\frac{P}{RT} \qquad b = \Omega_b\,\frac{RT_c}{P_c}$$

$$B = b\,\frac{P}{RT} \qquad W = w\,\frac{P}{RT} \qquad a = \Omega_a\,\frac{R^2{T_c}^2}{P_c}\,\alpha(T_r,\omega)$$

Gas	Pc (bar)	Tc (K)	ω
N_2	3.39	126.20	0.039
Ar	4.87	150.80	0.001
CO_2	7.38	304.12	0.2239

EOS Parameter	Redlich-Kwong (RK)	Soave-Redlich-Kwong (SRK)	Peng Robinson (PR)	Schmidt-Wenzel (SW)	Patel-Teja (PT)
	$\Omega_a = 0.42747$	$\Omega_a = 0.42747$	$\Omega_a = 0.457235$	$\Omega_a = [1-\eta(1-q)]^3$ q → Smallest positive root from: $(6\omega+1)q^3 + 3q^2 + 3q - 1 = 0$ $\eta = \frac{1}{3(1+q\omega)}$	$\Omega_a = 3\eta^2 + (1-3\eta) + 3(1-2\eta)\Omega_b + \Omega_b^2$ $\eta = 0.0211947\,\omega^2 - 0.076799\omega + 0.329032$
a	$\alpha = \frac{1}{\sqrt{T_r}}$	$\alpha = \left[1 + m\left(1-\sqrt{T_r}\right)\right]^2$	$\alpha = \left[1 + m\left(1-\sqrt{T_r}\right)\right]^2$	$\alpha = \left[1 + m\left(1-\sqrt{T_r}\right)\right]^2$	$\alpha = \left[1 + m\left(1-\sqrt{T_r}\right)\right]^2$
		$m = \frac{-0.176\,\omega^2 + 1.574\omega + 0.48}{1.18}$	$m = 0.1667\,\omega^3 - 0.1644\,\omega^2 + 1.485\omega + 0.3796$	$\omega < 0.371$ $m_0 = m_1 = -0.528\,\omega^2 + 1.347\omega + 0.465$ $\omega > 0.371$ $m_0 = m_2 = 0.9593\omega + 0.5361$ $\omega < 0.4$ $m = m_1 = m_0 + 0.01429\,(5T_r - 3m_0 - 1)^2$ $\omega > 0.55$ $m = m_2 = m_0 + 0.71\,(T_r - 0.779)^2$ $0.4 > \omega > 0.55$ $m = \left(\frac{0.55-\omega}{0.15}\right)m_1 + (\omega - 0.4)m_2$	$m = -0.295937\,\omega^2 + 1.30982\omega + 0.452413$
b	$\Omega_b = 0.08664$	$\Omega_b = 0.08664$	$\Omega_b = 0.077796$	$\Omega_b = \eta q$	Ω_b -> Smallest positive root from: $\Omega_b^3 + (2-3\eta)\Omega_b^2 + 3\eta^2\Omega_b - \eta^3 = 0$
u	$u = b$	$u = b$	$u = 2b$	$u = (1+3\omega)b$	$u = b + c$ $c = (1-3\eta)\frac{RT_c}{P_c}$
w	$w = 0$	$w = 0$	$w = 0$	$w^2 = 3\omega b^2$	$w^2 = bc$

Appendix B: Bulk Modulus Analysis for Sandstone and Shale

B.1 Sandstone with a Vacuum

The chronology of hydrostatically loading a Ferron sandstone sample with no fluid (vacuum) in the pore network is displayed in Figure B.1. In the plot in the left-hand panel, the horizontal axis is the elapsed time, the primary vertical axis is fluid pressure in the sample, and the secondary vertical axis is the measured volumetric strain in one direction. The confining pressure indicates the loading and unloading cycles from 100 to 1800 psi by pumping/withdrawing confining fluid (Paratherm oil) at a constant flow rate of 6 ml/min. The low flow rate for applying confining pressure ensures that the stresses in the sample are equilibrated within the rock matrix during the loading and unloading cycles (i.e., drained conditions). The pore pressure record indicates that a vacuum is maintained during the entire test, P_p = -10 psig, verifying that there are no leaks in the flowline.

The positive strain (Figure B.1) indicates that the sample experienced only compression (compared to the initial conditions at a relaxed state). The time record of the stress and strain response tracking each other indicates that the sample compresses during loading cycles and decompresses, or shrinks, during the unloading cycles. There is some hysteresis (it cannot be said if this is recoverable over time – anelastic). The maximum strain of ε = 0.0025 mm/mm indicates that this Ferron sandstone sample compressed by 0.25% of its original radius. The final strain of ε = 0.00075 mm/mm indicates that the sample does not immediately return to its initial condition of ε = 0 mm/mm, as the sample has been permanently deformed after the applied stresses are accommodated by the internal rock texture and features: grains, pores, bedding, and fractures. However, some of that permanent strain could be due to the seating of the cantilevers on the sample.

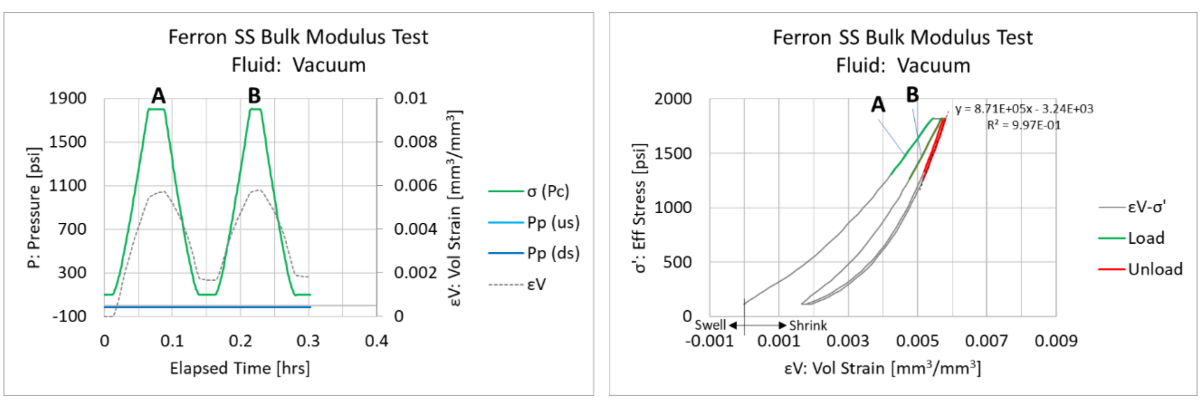

Figure B.1. Bulk modulus determination: Ferron sandstone under vacuum.

The bulk modulus of the Ferron sandstone sample, F-SS, was calculated from the stress-strain plot, with the measured strain in the horizontal axis and the effective stress in the vertical axis (parallel to bedding). Refer to Table 13.

Four different bulk moduli values were calculated corresponding to the loading and unloading steps for the initial and the repeated cycles (Table B.1). The initial loading starts from displacement zero and reaches a 0.0023 mm^3/mm^3 strain, decreasing to 0.0006 mm^3/mm^3 after the initial unloading. The second loading cycle produces a steeper slope,[45] thus a higher bulk modulus. Once the matrix has been compressed and it becomes stiffer - compared to the more relaxed initial conditions-. The unloading cycle is consistent with the initial conditions by decreasing to a similar strain of 0.0024 mm^3/mm^3, with a similar slope at a high value of effective stress.

Table B.1. Summary of the measured bulk modulus for hydrostatic loading of an evacuated Ferron sandstone sample.

Test	**Pore Pressure, P_P** (psig)	**Confining Pressure, σ** (psi)	**Bulk Modulus, K**	
			(10^6 psi)	**(10^9 Pa)**
A Load	-10	1800	0.43	2.9
A Unload	-10	100	0.89	6.2
B Load	-10	1800	0.59	4.1
B Unload	-10	100	0.87	6.00

B.2 Sandstone with N_2 as Pore Fluid

This set of experiments evaluated the sandstone's response when a relatively inert fluid (N_2) was injected into the Ferron Sandstone, with limited adsorption expected given the mineral analysis (regardless of the saturating fluid). The sequence of events is labeled in the pressure-time record in Figure B.2, labeled A through F.

- In *A*, the pore pressure is increased to 500 psi, followed by a loading and unloading cycle raising the confining pressure from 600 to 1800 psi and subsequently reducing the confining pressure to 600 psi, with the Terzaghi effective stress increasing from 100 to 1200 psi and decreasing to 100 psi.
- Cycles B and C simulate a more representative potential scenario for the downhole conditions in the Buzzard Bench field by setting the pore pressure at 1200 psi. Bringing the confining pressure from 1300 to 1800 psi (and back to 1300 psi) leads to a smaller range of effective stress - between 100 and 600 psi. Recall that the effective stress is the total stress minus a fraction of the pore pressure. The fractional modifier of the pore pressure is Biot's poroelastic parameter ($0 \leq \alpha \leq 1$). For materials with a high hydraulic diffusivity (such as soils and weakly consolidated rock), the assumption is made that Biot's parameter approaches 1, as was commonly adopted by Terzaghi in derivations for soil (and rock near failure).

[45] This characteristic behavior for a reload below the elastic limit of a porous material. Note also that the unloading modulus is higher, as is commonly the case.

The final stage of the test entailed setting the pore pressure to atmospheric pressure and repeating the loading and unloading cycles.

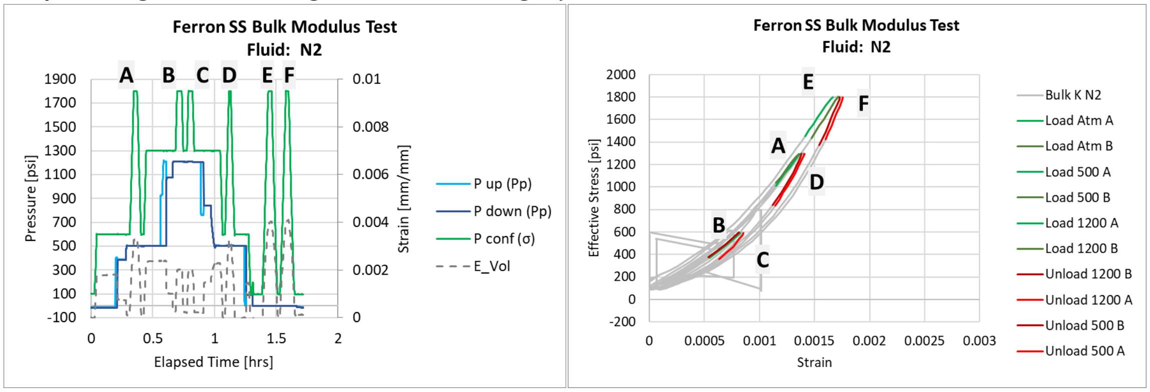

Figure B.2. Bulk modulus experiments: Sandstone flooded with N_2

The stress-strain plot for this test indicates that all the cycles, A through F, overlie each other, following a similar path regardless of the pore pressure. This is a manifestation of fundamental effective stress concepts. In the lower ranges of effective stress, the slope of the curve is smaller, indicating that the rock sample is in a more or less 'relaxed' state with flaws at least partially opened; small increases in the effective stress produce large deformation -strain- in the sample. As the effective pressure increases, the rock becomes stiffer, as observed in cycles E and F, where the rock deforms at a lower rate for similar increases in the effective stress. Other than the described poroelastic stresses, there appears to be little to no effect of N_2 on the F-SS structure.

B.3 Sandstone with Surrogate Flue Gas (80:20 N_2:CO_2)

The sample response in this experiment, with a simulated flue gas mixture (80:20 N_2:CO_2) flooding the sample is like that for the pure N_2. The three sets of effective stress conditions (with pore pressure at atmospheric, 500, and 1200 psi) produce stress-strain curves that overlie each other. The measured response shows a limited effect from CO_2 "compression" (compared to 100% CO_2), given the lower carbon dioxide concentration in the mixture. The response is shown in Figure B.3.

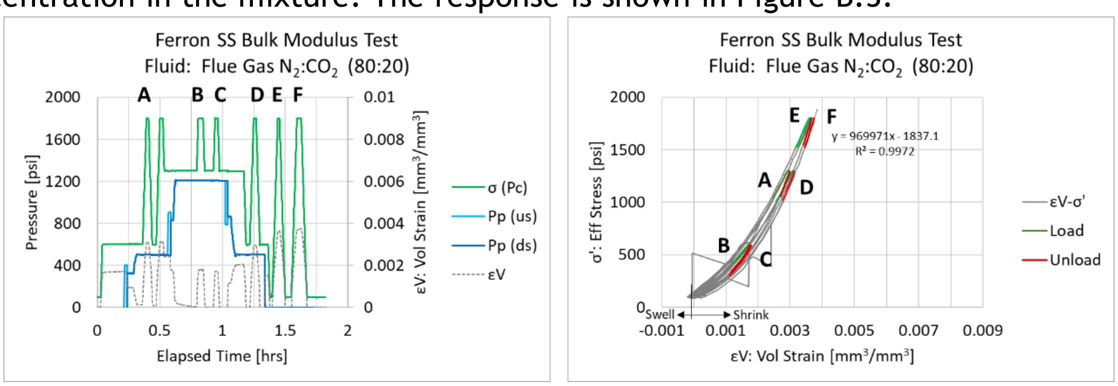

Figure B.3. Bulk modulus experiments: Ferron sandstone flooded with a flue gas proxy (N_2:CO_2, 80:20).

In conclusion, the effect of CO_2 even plays a role in the sandstone. Pore volume is sensitive to the dynamic thermodynamic properties of fluid compression, especially when transitioning from a gas to a supercritical phase where the compressibility of the CO_2 reduces considerably. The strain readings remained in the positive range, ruling out any adsorptive processes. This needs to be confirmed by more experimentation and there is even some question as to how the permeability will be affected.

B.4 Shale with a Vacuum

The Mancos shale overlies the Ferron sandstone/coal package and is envisioned as a seal. For this reason, a Mancos sample was exposed to the different gases as well. The prepared shale sample was only 2” in length. Therefore the axial strain assembly could not be installed. Instead, the strain ε_{t2} (parallel to the bedding) was considered as a substitute for the measurements in the axial direction. The testing chronology is shown in Figure B.4.

The bulk modulus measured with pore pressure on a vacuum indicated an anomaly in the volumetric strain by displaying a slight swelling of the sample at the beginning of the test. The slight difference in temperature (slightly higher in the oven) may have come into play. The rest of the loading cycles indicated only compression - positive values of the volumetric strain.

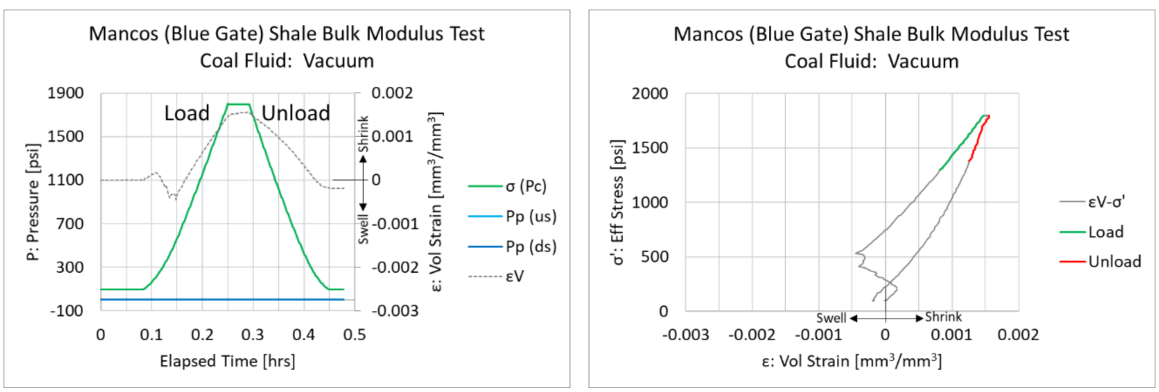

Figure B.4 Bulk modulus experiment for an evacuated Mancos (Blue Gate) shale sample.

B.5 Shale with N_2

The test with an inert fluid - nitrogen - was completed for pore pressures between atmospheric and 1200 psi (Figure B.5). The loading and unloading cycles, A to D, in the ε_V-σ’ plot overlie each other. This is similar behavior to that seen in the coal and sandstone described earlier.

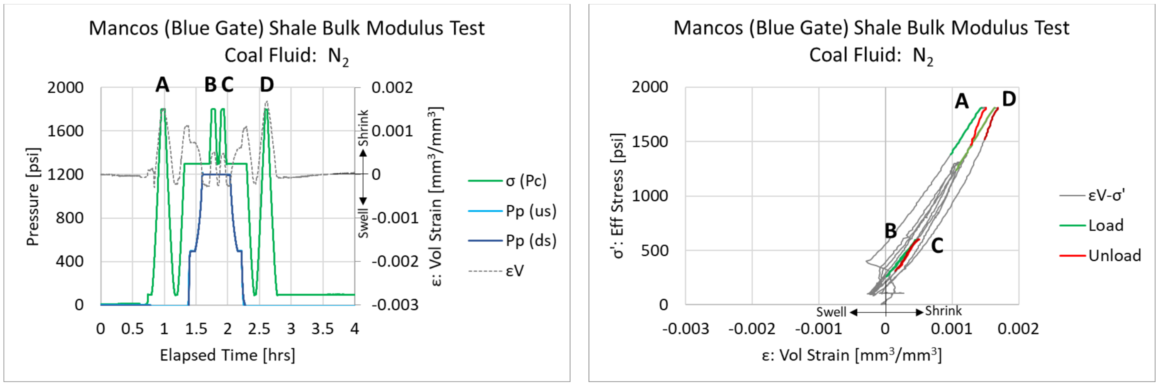

Figure B.5 Bulk modulus experiment for Mancos shale flooded with N_2.

B.6 Shale with Surrogate Flue gas (N_2:CO_2 80:20)

The flue gas in the shale did not demonstrate a mixed behavior of swelling and compression, as was observed with the coal. The behavior was more characteristic of that seen with the nitrogen (Figure B.6).

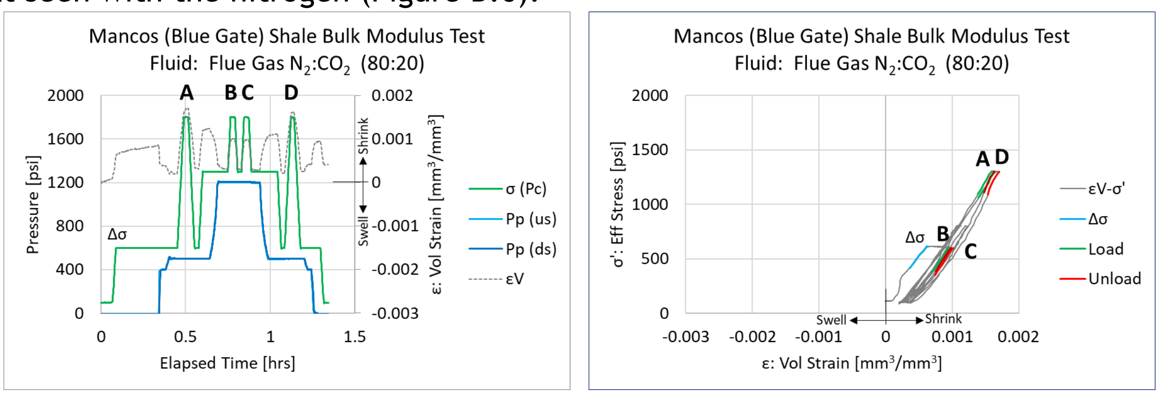

Figure B.6 Bulk modulus experiment on Mancos shale flooded with the simulated flue gas (N_2:CO_2, 80:20).

Appendix C: Economic Evaluations

There are several methods for comparison of costs of an ECBM program on a levelized basis – viewing comprehensive lifetime expenditures and revenue streams. The natural gas produced will be used to compress the carbon dioxide and for sales. One often hears of the levelized cost of energy, LCCE. One definition of LCCE is "the cost per unit of energy that, if held constant through the analysis period, would provide the same net present revenue value as the net present value cost of the system." (Short et al., 1995, p. 93). These calculations enable the comparison of various plant scenarios. It can be viewed as the breakeven cost where discounted revenues equal discounted net expenses.

$$LCOE = \sum_{t=0}^{n} \frac{Expenses}{(i+1)^t} \Bigg/ \sum_{t=0}^{n} \frac{E_t}{(i+1)^t} \qquad \text{(C-1)}$$

where:

LCOE .... levelized cost of energy
E_t .... energy delivered in year t
i............ discount rate
n............ lifetime of the project

In the case of the power plants in central Utah, energy conversion technologies may be more relevant, if an ECBM complement is planned – i.e., using the CO_2 to produce methane and using the methane to provide the energy to inject the carbon dioxide. Alternatively, a formal sequestration site can be considered. For this calculation, one needs to consider lifetime expenses that include investment costs, I; operation and maintenance (including waste management, O&M; fuel costs (such as compression for injection), F; carbon costs/credits, C; and decommissioning costs (well abandonment and restoration), D.

$$LCOE = \sum_{t=0}^{n} \frac{I_t + O\&M + F_t + C_t + D_t}{(i+1)^t} \Bigg/ \sum_{t=0}^{n} \frac{E_t}{(i+1)^t} \qquad \text{(C-2)}$$

To simplify this by assuming annual energy supplied is constant, economists may write:

$$\begin{aligned} LCOE &= \frac{i}{1-(i+1)} \frac{NPV(lifetime\ expenses)}{E} \\ &= CRF \frac{NPV(lifetime\ expenses)}{E} \\ &= \frac{Annuity(lifetime\ expenses)}{E} \end{aligned} \qquad \text{(C-3)}$$

where:
CRF... capital recovery factor
NPV ....net present value of all lifetime expenditures

For constant annual costs (O&M and fuel only):

$$LCOE = \frac{CRF \cdot I + O\&M + F}{E} \tag{C-4}$$

where:
I.........................upfront investment (all capital expenditures discounted to t = 0)
O&M........ annual operation and maintenance cost (could include byproduct revenue)
F...annual fuel cost
E... annual energy provision

It may be more important to consider greenhouse gas mitigation – consider mitigation costs normalized by the avoided emissions (Levelized cost of conserved carbon (LCCC). Suppose the annual reduction in GHG emissions is ΔC and ΔL indicates the lifetime of expenses.

$$LCOE = CRF \frac{NPV(\Delta L)}{\Delta C} = \frac{Annuity(\Delta L)}{\Delta C} \tag{C-5}$$

If we assume annual consistency (no change in emission, annual O&M, annual benefits ΔB above the baseline …)

$$LCCC = \frac{CRF \cdot \Delta I + \Delta O\&M - \Delta B}{\Delta C} \tag{C-6}$$

ΔI indicates the incremental investment for mitigation above the baseline investment.